UNIVERSIDAD DE CHILE
FACULTAD DE CIENCIAS FÍSICAS Y MATEMÁTICAS
DEPARTAMENTO DE INGENIERÍA MATEMÁTICA

INVERSE PROBLEMS IN ELASTOGRAPHY AND DISPLACEMENT-FLOW MRI

TESIS PARA OPTAR AL GRADO DE
DOCTOR EN CIENCIAS DE LA INGENIERÍA,
MENCIÓN MODELACIÓN MATEMÁTICA
EN COTUTELA CON LA UNIVERSIDAD DE GRONINGEN

HUGO PATRICIO ANNER CARRILLO LINCOPI

PROFESORES GUÍAS:
AXEL OSSES ALVARADO
ROEL VERSTAPPEN

MIEMBROS DE LA COMISIÓN:
BANGTI JIN
JAIME ORTEGA PALMA
ARJAN VAN DER SCHAFT
CHRISTIAAN STOLK

Este trabajo ha sido parcialmente financiado por Beca Doctorado Nacional Conicyt 2015 21151645, CMM Conicyt PIA AFB170001 y Fondecyt 1151512-1191903

SANTIAGO DE CHILE
2020

SUMMARY OF THE THESIS TO OBTAIN THE DEGREE
OF: DOCTOR EN CIENCIAS DE LA INGENIERÍA,
MENCIÓN MODELACIÓN MATEMÁTICA
BY: HUGO CARRILLO LINCOPI
DATE: JANUARY 30, 2020
ADVISOR 1: AXEL OSSES
ADVISOR 2: ROELAND VERSTAPPEN

Inverse problems in elastography and displacement-flow MRI

In the context of medical imaging, we present a new method for the reconstruction of the following parameters of interest: the velocity of blood in vessels via magnetic resonance imaging (MRI) and the displacements of tissues under a harmonic regime via MRI. The method has been called Optimal Dual-Venc due its least squares approach using two VENCs (a key parameter in the standard velocity reconstructions via MRI) and its advantage is that we can measure, with respect to other methods, a wider range of velocities-displacements while keeping a low noise in the images.

In addition, in the context of elasticity imaging, we study the inverse problem of the recovery of the shear modulus (an elastic feature that characterizes a tissue) under the following models: linear elasticity (small displacements) with internal measurements of elastic energy density, assuming an incompressible displacement field, in dimension two, and the (nonlinear) Saint-Venant model of elasticity with internal measurements of the displacement field (as in the case of magnetic resonance elastography), in dimension two and three. We obtain as a result of our study the feasibility of a recovery of the shear modulus in a unique and stable way. Techniques in this part are mainly in the context of hybrid inverse problems, elliptic systems of PDEs, pseudodifferential operators, Douglis-Nirenberg numbers and Lopatinskii condition.

RESUMEN DE LA TESIS PARA OPTAR AL GRADO DE:
DOCTOR EN CIENCIAS DE LA INGENIERÍA,
MENCIÓN MODELACIÓN MATEMÁTICA
POR: HUGO CARRILLO LINCOPI
FECHA: 30 DE ENERO DE 2020
PROF. GUÍA 1: AXEL OSSES
PROF. GUÍA 2: ROELAND VERSTAPPEN

Inverse problems in elastography and displacement-flow MRI

En el contexto de imágenes médicas, presentamos un nuevo método para la reconstrucción de los siguientes parámetros de interés: la velocidad sanguínea en los vasos vía imágenes de resonancia magnética (MRI) y el desplazamiento de tejidos bajo un régimen armónico vía MRI. El método ha sido llamado Optimal Dual-Venc debido a su enfoque de mínimos cuadrados usando dos VENCs (un parámetro clave en las reconstrucciones estándar de velocidad vía MRI) y su ventaja es que podemos medir, con respecto a otros métodos, un rango más amplio de velocidades-desplazamientos mientras las imágenes mantienen un ruido bajo.

Además, en el contexto de imágenes de elasticidad, estudiamos el problema inverso de la reconstrucción del módulo de corte (un parámetro elástico que caracteriza un tejido) bajo los siguientes modelos: elasticidad lineal (pequeños desplazamientos) con mediciones internas de densidad de energía elástica, asumiendo un campo de desplazamientos incompresible, en dimensión dos, y el modelo de elasticidad (no-lineal) de Saint-Venant con mediciones internas del campo de desplazamientos (como en el caso de resonancia magnética de elastografía), en dimensión dos y tres. Obtenemos como resultado de nuestro estudio la factibilidad de la recuperación del módulo de corte de manera única y estable. Las técnicas en esta parte se sitúan principalmente en el contexto de problemas inversos híbridos, sistemas elípticos de EDPs, operadores pseudodiferenciales, números de Douglis-Nirenberg y la condición de Lopatinskii.

SAMENVATTING VAN DE PROEFSCHRIFT
OM HET GRAAD TE KRIJGEN VAN:
DOCTOR EN CIENCIAS DE LA INGENIERÍA,
MENCIÓN MODELACIÓN MATEMÁTICA
DOOR: HUGO CARRILLO LINCOPI
DATUM: 30 JANUARI 2020
PROMOTOR 1: AXEL OSSES
PROMOTOR 2: ROELAND VERSTAPPEN

Inverse problems in elastography and displacement-flow MRI

In de context van medische beeldvorming presenteren we een nieuwe methode voor de reconstructie van de volgende interessante parameters: de snelheid van bloed in bloedvaten via magnetische resonantiebeeldvorming (MRI) en de verplaatsingen van weefsels onder een harmonisch regime via MRI. De methode is Optimal Dual-Venc genoemd vanwege de kleinste-kwadraten benadering met twee VENC's (een belangrijke parameter in de standaard snelheidsreconstructies via MRI) en het voordeel is dat we, ten opzichte van andere methoden, een breder bereik van snelheden en verplaatsingen kunnen meten met behoud van weinig ruis in de afbeeldingen.

Bovendien bestuderen we in de context van elasticiteitsbeeldvorming het inverse probleem van het bepalen van de schuifmodulus (een elastische eigenschap die een weefsel kenmerkt) in de volgende modellen: lineaire elasticiteit (kleine verplaatsingen) met interne metingen van elastische energiedichtheid, uitgaande van een niet-samendrukbaar verplaatsingsveld, in twee dimensies, en het (niet-lineaire) Saint-Venant-elasticiteitsmodel met interne metingen van het verplaatsingsveld (zoals in het geval van magnetische resonantie-elastografie), in twee en drie ruimtelijke dimensies. Als resultaat van onze studie verkrijgen we dat het bepalen van de afschuifmodulus op een unieke en stabiele manier haalbaar is. Technieken in dit deel zijn voornamelijk in de context van hybride inverse-problemen, elliptische systemen van PDE's, pseudo-differentiële operatoren, Douglis-Nirenberg-getallen en Lopatinski-conditie.

Aknowledgements

I would like to thank CONICYT for the financial support through the PhD fellowship I received.

My gratitude to Axel Osses and Roel Verstappen for accepting being my supervisors at the University of Chile and the University of Groningen, respectively, thank you for your time reading and discussing the results of my thesis. I would like to thank the members of my assessment committee, Arjan van der Schaft, Bangti Jin, Christiaan Stolk and Jaime Ortega for reading and correcting this thesis.

I would like to thank Cristóbal Bertoglio, my daily supervisor for the first part of this thesis, for all the support and dedication during this whole period. We met in 2016 at the University of Chile and started to work together. He is one of the main responsible of this double degree adventure.

I would like to thank Alden Waters, my daily supervisor for the second part of this thesis. She received me in Groningen and made me work hard. Certainly I feel that I learned a lot under her supervision, so thank you for your patience and dedication.

Also, I would like to thank the people that collaborated in my thesis and learning in this time: Sergio Uribe for his support at the Center of Biomedical Imaging, discussions about MRI and image adquisitions, and Maya De Buhan for receiving me at the Laboratoire MAP5 in Paris V and for her disposition to discuss about elasticity equations. Thanks to the people who helped me with administrative affairs: Richard Weber, Paula Castillo, Silvia Mariano at the University of Chile and Annette Korringa, Elina Sietsema at the University of Groningen. I extend my gratitude to all the people that made this double degree possible.

Thanks to Jeremías Garay and the colleagues in Groningen for the reception. Special mention to David Nolte for his help answering all my questions about the double degree, and Ronald Remmerswaal for helping me with the Sammenvatting. Of course, I would like to thank my colleagues in Chile: Hugo Maturana, Evelyn Cueva, Rodrigo Quezada, Roberto Morales and all the colleagues I spent time with. Thanks for the good moments, mathematical discussions and many jokes. Special mention to Los Compares.

I would like to thank my family for all the support during this years: my brother Carlos, my sisters Andrea and Rosa, and especially my parents Hugo Carrillo and Rosa Lincopi. Los quiero un montón, gracias por estar siempre conmigo. Papá y mamá, este logro también es de ustedes.

Finally, thanks to my beloved Valentina Díaz for being besides me all this time, even when we were spatially far from each other. Thanks Valentina for always reading and listening to me in good and bad times. Sincerely, I hope we continue ahead giving us much joy, support and love. Has sido un apoyo fundamental, ¡gracias!

Contents

Chapter 1

Introduction

1.1 Motivation

In this thesis we study some inverse problems in MRI and in elasticity imaging. A problem is called *inverse* if its formulation involves the solution of other problem, called *direct*. In science, the *direct* problem comes from fundamental laws, such as energy conservation; the *inverse* problem consists in the determination of the parameters of the equations governing the direct problem, from the knowledge of the solution entirely or a part of it. In other words, by solving an inverse problem, parameter values that cannot be obtained directly can be found.

Magnetic resonance imaging (MRI) is a noninvasive biomedical imaging technique. Its development comes from the study of the nuclear magnetic resonance by Felix Bloch and Edward Purcell [Blo46] and later the development of the tomographic technique by Paul Lauterbur and Peter Mansfield [Lau+73; Man82]. MRI has potential advantages over other techniques: lack of ionizing radiation, free choice of imaging planes, high resolution, capability for tissue characterization, etc. The characterization of tissues can be anatomical and qualitative or even quantitative giving a map of a specific parameter which can be obtained from the MRI technique, such as: proton density, magnetic relaxation times, water diffusivity, velocity and displacement. Each of the parameters mentioned above has the capability of characterizing a biological tissue, in order to detect any disease, see for example [JBP+05; CJ05; MBV06; GME12].

In this thesis we are interested in the recovery of the following parameters from magnetization measurements in MRI: the velocity of blood flowing in vessels and the displacements of tissues under a harmonic regime. Both velocity and displacement imaging is achieved by the so-called *Phase-Contrast MRI* (PC-MRI), that is, the derivation of the quantity of interest is performed by the substraction (modulo 2π) of two measured phases of the complex transverse magnetization in MRI.

Imaging the velocity of blood flow finds its main application in the research into cardiovascular diseases, since heart failure is a major cause of death in Western societies and will become even more prevalent with increasing life expectancy [MBV06]. Blood velocity measurements can also lead to the recovery of further mechanical information like relative pressures [Yan+96; Ber+18; NB19; Nol+19] and wall shear stress [Sot+12; Sot+16].

Imaging the harmonic displacements in tissues finds its motivation in *elastography*, that is, two-step techniques consisting in measuring the displacements of a tissue and then recov-

ering some elastic parameter of it. Examples of elastography techniques are ultrasound and magnetic resonance elastography (MRE). Several diseases involve changes in the mechanical properties of tissue and normal function of tissue, like skeletal muscle, heart, lungs, gut, etc. The changes in mechanical properties are not best seen precisely in the displacement map, but the best contrast is seen in the spatial distribution of any elastic parameter [HSB17]. These elastic parameters can be then reconstructed from the knowledge of the displacement map, using the elasticity equations.

Mathematically, elasticity imaging techniques have given rise to many problems which are challenging in many branches of mathematics. Our focus will be on partial differential equations, studying nonlinear models for elasticity and the measurements. In the literature, inverse problems in elasticity are most studied for linear models, however those models do not describe accurately some phenomena, but nonlinear elasticity models do it.

1.2 Research objectives

The topics presented in this thesis are:

1. The proposal of a new method for the recovery of the velocity of blood from MRI measurements. The proposed method is more robust, meaning less affected by noise and able to measure a wider range of velocities than the usual methods. This method is motivated, proposed and tested in Chapter 2. In addition, in Chapter 3 the natural extension to MRE is discussed.

2. Analysis of nonlinear inverse problems in elasticity, in two cases: assuming the measurements or the elasticity model being nonlinear. This analysis motivates techniques for the reconstruction of an elasticity parameter. Examples will be presented. This topic is developed in Chapter 4.

In the following two sections we will provide the reader the fundamentals of MRI for the comprehension of velocity and displacement recovery, and also fundamentals of hybrid inverse problems and elasticity equations.

1.3 Magnetic Resonance Imaging

1.3.1 Generalities of MRI

The nuclear magnetic resonance phenomenon is modeled by the Bloch equation of the magnetization $\boldsymbol{M} = [M_1, M_2, M_3]^\intercal$ of protons in position $\boldsymbol{X}(t)$ at time t under the influence of a magnetic field $\boldsymbol{B}$ [Abr61; Sli13]:

$$\frac{d\boldsymbol{M}}{dt} = \gamma \boldsymbol{M} \times \boldsymbol{B} + \frac{1}{T_1}(M_0 - M_3)\boldsymbol{e}_3 - \frac{1}{T_2}\boldsymbol{M}_\perp \tag{1.1}$$

where T_1 and T_2 are *relaxation times*, M_0 is the magnetization at equilibrium, $\boldsymbol{M}_\perp = M_1\boldsymbol{e}_1 + M_2\boldsymbol{e}_2$ and $(\boldsymbol{e}_1, \boldsymbol{e}_2, \boldsymbol{e}_3)$ are the basis vectors of the frame of reference.
The Bloch equation represents the conservation of angular momentum of the spin of the

protons, including quantum effects.
By components, this is:

$$\frac{dM_1}{dt} = \gamma(B_3M_2 - B_2M_3) - \frac{M_1}{T_2}, \tag{1.2}$$

$$\frac{dM_2}{dt} = \gamma(-B_3M_1 - B_1M_3) - \frac{M_2}{T_2}, \tag{1.3}$$

$$\frac{dM_3}{dt} = \gamma(B_2M_1 - B_1M_2) - \frac{M_3 - M_0}{T_1}. \tag{1.4}$$

The main steps in MRI are defined by different stages of the "controlled" magnetic field $\boldsymbol{B}$:

- Initially, $\boldsymbol{B} = B_0\boldsymbol{e}_3$, where B_0 has a much larger magnitude compared with all the other fields described below. The field $B_0\boldsymbol{e}_3$ is constant in time and space and it is present in all the experiment. Under this equilibrium condition, $M_1 = M_2 = 0$.

- The application of a *radiofrequency pulse* (rf pulse) causes the *resonance* in spins, that pulse is generated by adding a time-harmonic field $B_1(t)\boldsymbol{e}_1$ for a very short period of time. This creates the transversal magnetization to tip towards the transversal plane, i.e. $M_1 \neq 0, M_2 \neq 0$.

- When the rf pulse is released, the problem is studied only using equations (1.2)-(1.3), and a non-zero initial condition, because the measurements that the scanner gives us are $M_{xy} = M_1 + iM_2$.

- In order to recover the desired physical quantity, we modify the component B_3. The description for velocity and displacement recovery is given in the remaining of this section.

For our purposes, we will also consider the relaxation time T_2 large enough for neglecting the term $\frac{\boldsymbol{M}_\perp}{T_2}$. Therefore, from equations (1.2)-(1.3), we see that M_{xy} satisfies the following equation:

$$\frac{dM_{xy}}{dt} = -i\gamma B_3 M_{xy}. \tag{1.5}$$

Hence

$$M_{xy}(\boldsymbol{X}(t), t) = M_{xy}(t_0)\exp\Big(-i\gamma\int_{t_0}^{t} B_3(\boldsymbol{X}(t'), t')dt'\Big).$$

We can fix $M_{xy}(t_0) \in \mathbb{R}$, and then we can write

$$M_{xy}(t) = M_{xy}(t_0)e^{i\varphi(\boldsymbol{X}(t),t)}$$

where the *phase*

$$\varphi(\boldsymbol{X}(t), t) = -\gamma\int_{t_0}^{t} B_3(\boldsymbol{X}(t'), t')dt' \tag{1.6}$$

is the key quantity in this work.

1.3.2 Velocity Encoding

We now assume that the spins are moving "locally" following the equation

$$\boldsymbol{X}(t) = \boldsymbol{x} + t\boldsymbol{u} \tag{1.7}$$

where $\boldsymbol{x}, \boldsymbol{u}$ are time-constant vectors. In particular, $\boldsymbol{x}$ corresponds to the original position of the spins at $t = 0$, and $\boldsymbol{X}(t)$ to the position of the spins at time t. In addition, let us consider the component B_3 with the form

$$B_3(\boldsymbol{X}(t), t) = B_0 + \boldsymbol{X}(t) \cdot \boldsymbol{G}(t)$$

where $\boldsymbol{G}(t)$ is a constant-in-space vector. Then, equation (1.6) becomes, at the time of measurement T_E, and passing the dependence from $\boldsymbol{X}(T_E)$ to $\boldsymbol{x}$ and $\boldsymbol{u}$ due (1.7):

$$\varphi(\boldsymbol{X}(T_E), T_E) = \varphi(\boldsymbol{x}, \boldsymbol{u}, T_E) = -\Big(\gamma B_0 T_E + \gamma \boldsymbol{x} \cdot m_0(\boldsymbol{G}) + \gamma \boldsymbol{u} \cdot m_1(\boldsymbol{G})\Big)$$

where

$$m_0 = \int_0^{T_E} \boldsymbol{G}(t')dt', \quad m_1 = \int_0^{T_E} t'\boldsymbol{G}(t')dt'$$

are known as the zeroth and first moments, respectively [KJH18]. It is usual in MRI practice to consider a *waveform* $\boldsymbol{G}(t)$ such that $m_0(\boldsymbol{G}) = 0$ in order to remove it from the velocity reconstruction problem. Then the model of the phase $\varphi = \varphi(\boldsymbol{x}, \boldsymbol{u}, T_E)$ reads:

$$\varphi = \varphi_0 + \gamma u m_1(G) \ , \ \varphi_0 := \gamma B_0 T_E, \tag{1.8}$$

with v the component of the velocity in direction of $\boldsymbol{G}$, and G the magnitude of the vector $\boldsymbol{G}$.

Since φ_0 is not fully known due to inhomogeneities in the magnetic field B_0, we cannot obtain v directly from equation (1.8). So, for each $\boldsymbol{x}$ we consider two measurements φ^{G_0} and φ^{G_1} satisfying (1.8) with waveforms G_0 and G_1 respectively, so that we can obtain u via the formula

$$u = \frac{\varphi^{G_0} - \varphi^{G_1}}{\gamma(m_1(G_0) - m_1(G_1))}. \tag{1.9}$$

In practice, the user controls indirectly the strength of the magnetic fields by setting the *velocity encoding* parameter, VENC, defined by:

$$\mathrm{VENC}(G_0, G_1) = \frac{\pi}{\gamma(m_1(G_0) - m_1(G_1))},$$

which has the dimension of velocity. According to equation (1.9), the velocity can be determined by:

$$u = \frac{\varphi^{G_0} - \varphi^{G_1}}{\pi}\mathrm{VENC}(G_0, G_1). \tag{1.10}$$

This is the standard *phase contrast* MRI technique for velocity recovery (PC-MRI). Note that $u = u(\boldsymbol{x})$.

1.3.3 Magnetic Resonance Elastography (MRE)

Instead of assuming that the motion is modelled by (1.7), we adopt the following model [Man+01; HSB17]:

$$\boldsymbol{X}(\boldsymbol{x},t) = \boldsymbol{x} + \boldsymbol{U}(\boldsymbol{x},t) \tag{1.11}$$

where the displacement $\boldsymbol{U}(\boldsymbol{x},t)$ is given by

$$\boldsymbol{U}(\boldsymbol{x},t) = \mathrm{Re}\Big(\boldsymbol{u}_c(\boldsymbol{x})e^{i\omega t}\Big). \tag{1.12}$$

This motion is caused by some periodic external force, where $\boldsymbol{u}_c(\boldsymbol{x}) \in \mathbb{C}^d$ describes a complex steady-state behavior.

The waveform $\boldsymbol{G}(t)$, called *motion encoding gradient (MEG)* in this context, is zeroth moment nulling. Typically, the MEG $G(t)$ is set either as:

- *symmetric*, that is $\boldsymbol{G}(t) = \boldsymbol{G}(-t)$, or
- *antisymmetric*, that is $\boldsymbol{G}(t) = -\boldsymbol{G}(-t)$,

where we set $t = 0$ at the middle of the time of the application of the MEG,that is the MEG is assumed to be applied for $t \in \Big[-\frac{T}{2}, \frac{T}{2}\Big]$, where $T = \frac{2\pi}{\omega}$.

Then the equation (1.6) for the phase of the spins moving under this model and under this gradient field is given by

$$\varphi(\boldsymbol{x}) = \varphi_0 + \gamma \int_{-T/2}^{T/2} G(t) \cdot X(\boldsymbol{x},t)dt$$

where G is the magnitude of the vector $\boldsymbol{G}$ and X is the component of $\boldsymbol{X}$ in direction of $\boldsymbol{G}$. We will denote by u_c the component of $\boldsymbol{u}_c$ in the direction of $\boldsymbol{G}$. The phase φ_0 is static and it can be measured by a null MEG, so we are interested only in the dynamic phase:

$$\vartheta(\boldsymbol{x}) = \gamma \int_{-T/2}^{T/2} G(t) \cdot X(\boldsymbol{x},t)dt$$

We have:

$$\begin{aligned}
\vartheta(\boldsymbol{x}) &= \gamma \int_{-T/2}^{T/2} G(t)\Big(x + \mathrm{Re}(u_c(\boldsymbol{x})e^{i\omega t})\Big)dt \\
&= \gamma x \int_{-T/2}^{T/2} G(t)dt + \gamma \mathrm{Re}\Big(u_c(\boldsymbol{x}) \int_{-T/2}^{T/2} G(t)e^{i\omega t}dt\Big) \\
&= \gamma \mathrm{Re}\Big(u_c(\boldsymbol{x}) \int_{-T/2}^{T/2} G(t)e^{i\omega t}dt\Big) \\
&= \gamma\Big(\mathrm{Re}(u_c) \int_{-\frac{T}{2}}^{\frac{T}{2}} G(t)\cos(\omega t)dt - \mathrm{Im}(u_c) \int_{-\frac{T}{2}}^{\frac{T}{2}} G(t)\sin(\omega t)dt\Big)
\end{aligned}$$

where we use the fact that $G(t)$ is zeroth moment nulling, so the term $\gamma x \int_{-T/2}^{T/2} G(t)dt$ in the second line is null. Therefore we obtain:

$$\frac{\vartheta(\boldsymbol{x})}{\xi(\omega,T)} = \begin{cases} \mathrm{Re}(u_c(\boldsymbol{x})) & \text{for } G \text{ symmetric, } \xi(\omega,T) = \gamma \int_{-\frac{T}{2}}^{\frac{T}{2}} G(t)\cos(\omega t)dt \\ \mathrm{Im}(u_c(\boldsymbol{x})) & \text{for } G \text{ antisymmetric, } \xi(\omega,T) = -\gamma \int_{-\frac{T}{2}}^{\frac{T}{2}} G(t)\sin(\omega t)dt \end{cases}$$

where $\xi(\omega,T)$ is known as the *encoding efficiency*. This is a key controlled parameter in MRE.

Several measurements and the discrete Fourier transform in time

To identify displacements at different states of the wave given by (1.12), we consider

$$\boldsymbol{U}_c(\boldsymbol{x},\tau) = \boldsymbol{u}_c(\boldsymbol{x})e^{i\omega\tau}$$

where τ is the time corresponding to the displacement observed by the MRI experiment, which corresponds to the complex displacement at the time of the rf pulse, here $\boldsymbol{u}_c$ corresponds to the complex displacement of maximum amplitude. Then

$$\boldsymbol{U}(\boldsymbol{x},\tau,t) = \mathrm{Re}\Big(\boldsymbol{U}_c(\boldsymbol{x},\tau)e^{i\omega t}\Big)$$

is the displacement occurring at time t after the rf pulse. Following the analysis done before, we can obtain by PC-MRI either $\mathrm{Re}(u_c(\boldsymbol{x})e^{i\omega\tau})$ or $\mathrm{Im}(u_c(\boldsymbol{x})e^{i\omega\tau})$ in the direction of the MEG $\boldsymbol{G}(t)$.

For reconstructing any elastic parameter, it would be better to have a displacement field suitable in a time independent equation (see next section). For achieving that, let $n = 0,\ldots,N-1$, and consider the set of N displacements as follows:

- Considering the harmonic regime as above, let $u_n(\boldsymbol{x})$ be the PC-MRI measurement of the displacement of the spins having its position in $\boldsymbol{x}$ at a certain time τ_n. That is, we assume the model:

$$u_n(\boldsymbol{x}) = \begin{cases} \mathrm{Re}\Big(u_c(\boldsymbol{x})e^{i\omega\tau_n}\Big) & \text{if } G \text{ is symmetric,} \\ \\ \mathrm{Im}\Big(u_c(\boldsymbol{x})e^{i\omega\tau_n}\Big) & \text{if } G \text{ is antisymmetric,} \end{cases} \tag{1.13}$$

  where each u_n is obtained from the measurement ϑ_n:

$$u_n = \frac{\vartheta_n}{\xi(\omega,T)}. \tag{1.14}$$

- We apply the following discrete Fourier transform for $\{u_n\}_{n=0}^{N-1}$:

$$u_{FT} \;=\; \sum_{n=0}^{N-1} u_n e^{-i\frac{2\pi n}{N}}$$

  and we choose $\tau_n = \dfrac{Tn}{N}$.

- If $G(t)$ is symmetric, then we have:

$$u_n(\boldsymbol{x}) = \mathrm{Re}\Big(u_c(\boldsymbol{x})e^{i\frac{2\pi n}{N}}\Big)$$

and then

$$\begin{aligned} u^s_{FT} &= \sum_{n=0}^{N-1} \mathrm{Re}\Big(u_c(\boldsymbol{x})e^{i\frac{2\pi n}{N}}\Big)e^{-i\frac{2\pi n}{N}} \\ &= \sum_{n=0}^{N-1}\Big[\mathrm{Re}(u_c)\cos\Big(\frac{2\pi n}{N}\Big) - \mathrm{Im}(u_c)\sin\Big(\frac{2\pi n}{N}\Big)\Big]\Big[\cos\Big(\frac{2\pi n}{N}\Big) - i\sin\Big(\frac{2\pi n}{N}\Big)\Big] \\ &= \sum_{n=0}^{N-1}\Big[\mathrm{Re}(u_c)\cos^2\Big(\frac{2\pi n}{N}\Big) - \mathrm{Im}(u_c)\sin\Big(\frac{2\pi n}{N}\Big)\cos\Big(\frac{2\pi n}{N}\Big)\Big] \\ &\qquad +i\Big[-\mathrm{Re}(u_c)\cos\Big(\frac{2\pi n}{N}\Big)\sin\Big(\frac{2\pi n}{N}\Big) + \mathrm{Im}(u_c)\sin^2\Big(\frac{2\pi n}{N}\Big)\Big] \\ &= \frac{N}{2}u_c \end{aligned}$$

since

$$\sum_{n=0}^{N-1}\cos^2\Big(\frac{2\pi n}{N}\Big) = \sum_{n=0}^{N-1}\sin^2\Big(\frac{2\pi n}{N}\Big) = \frac{N}{2}$$

and

$$\sum_{n=0}^{N-1}\cos\Big(\frac{2\pi n}{N}\Big)\sin\Big(\frac{2\pi n}{N}\Big) = 0.$$

- Similarly, we obtain for the case G antisymmetric:

$$u^a_{FT} = i\frac{N}{2}\overline{u}_c$$

Therefore,

$$u_c = \begin{cases} \dfrac{2}{N}u^s_{FT} & \text{if } G \text{ is symmetric,} \\ \dfrac{2i}{N}\overline{u}^a_{FT} & \text{if } G \text{ is antisymmetric.} \end{cases} \tag{1.15}$$

Now that we have obtain u_c is we can recover completely the model (1.12) in order to characterize the viscoelastic properties of a tissue [HSB17], and also we can use algorithms for recovering the shear modulus from a time independent elasticity equation, see for example [AWZ15].

1.4 Hybrid Inverse Problems in Elasticity

1.4.1 Hybrid Inverse Problems

Hybrid inverse problems are inverse problems that describe coupled-physics phenomena in order to reconstruct a parameter of interest. The main idea of hybrid inverse problems is given in two steps:

- First, a high-resolution inverse problem is solved to provide internal information involving solutions and parameters of a differential equation.
- Next, the obtained internal information, also called internal functional, is used to reconstruct with high-contrast the parameter of interest of the inverse problem.

In some settings, a single modality gives a reconstruction with either high contrast or high resolution, but not both at the same time. Under convenient conditions, the physical coupling defining a hybrid inverse problem result in a reconstruction with a high contrast and resolution.

Hybrid inverse problems are useful in, for example, medical and geophysical imaging. Several examples of physical couplings defining hybrid inverse problems are described in [Bal13], for example: the photo-acoustic effect, the ultrasound modulation effect, transient elastography, current density imaging.

The mathematical analysis of many hybrid inverse problems falls within the context of linear and nonlinear equations or systems of equations. In particular, in this thesis, the study of the second step is given by the theory of redundant systems of elliptic partial differential equations, coupling system

$$\begin{cases} \mathcal{L}v &= f \quad \text{in } \Omega, \\ \mathcal{B}v &= g \quad \text{on } \partial\Omega, \end{cases}$$

with the functionals related with the measurements

$$\mathcal{M}v = H \text{ in } \Omega,$$

where $v = (\gamma, u)$, γ is the set of parameters to reconstruct, u is the solution of the direct problem, $\mathcal{L}, \mathcal{B}, \mathcal{M}$ are operators acting on v, Ω is an open bounded subset of $\mathbb{R}^d$ with smooth boundary.

A main tool in our study of hybrid inverse problems is the symbol of a differential operator, since it will provide important properties of equations. We use the definition of symbol given in [Esk11] and we present it here.

Definition 1.1. *If $A(x, D)$ (with $D = -i\frac{\partial}{\partial x}$) is a differential operator having the form*

$$A(x, D)u = \sum_{|k|=0}^{m} a_k(x)\Big(- i\frac{\partial}{\partial x}\Big)^k u,$$

then the symbol of $A(x, D)$ is the polynomial $A(x, \xi)$ defined by

$$A(x, \xi) = \sum_{|k|=0}^{m} a_k(x)\xi^k$$

and its principal symbol is the polynomial $A_0(x, \xi)$ defined by

$$A_0(x, \xi) = \sum_{|k|=m} a_k(x)\xi^k.$$

Note that the definition is related with the following well-known Fourier transform property for partial derivatives

$$\mathcal{F}[D^k u](\xi) = \xi^k \mathcal{F}[u](\xi)$$

where we can see that he symbol of the differential operator D^k is ξ^k.

1.4.2 Linear Elasticity Equations

We consider elastic deformations that are given by [Amm+15]:

$$\rho \boldsymbol{U}_{tt} - \nabla \cdot S[\boldsymbol{U}] = \boldsymbol{F} \tag{1.16}$$

where $\boldsymbol{U}(\boldsymbol{x}, t)$ is the displacement field, $\boldsymbol{F}(\boldsymbol{x}, t)$ is the excitation force density, and S is the Cauchy stress tensor which in case of *linear elasticity* is given by

$$S[\boldsymbol{U}] = 2\mu \boldsymbol{\epsilon}[\boldsymbol{U}] + \lambda(\mathrm{tr}(\boldsymbol{\epsilon}[\boldsymbol{U}])I_d$$

where

$$\boldsymbol{\epsilon}[\boldsymbol{U}] = \frac{1}{2}(\nabla \boldsymbol{U} + \nabla \boldsymbol{U}^\intercal) = \nabla^S \boldsymbol{U}$$

is the *infinitesimal strain tensor*.

As in section 1.3.3, if the force is periodic in time with frequency ω, the resulting displacements will be perodic in time as well. After applying a Fourier transform in time in equation (1.16), we obtain:

$$\omega^2 u + 2\nabla \cdot \mu \nabla^S u + \nabla(\lambda \nabla \cdot u) = 0 \tag{1.17}$$

where $u = u(x, \omega)$ is the Fourier transform of $\boldsymbol{U}(x, t)$ in the variable t, evaluated in the frequency ω.

1.5 Thesis Overview

The main contributions of this thesis are new methods for the reconstruction of the following parameters of interest: the velocity of blood in vessels via magnetic resonance imaging (MRI), the displacements of tissues under a harmonic regime via MRI, and the shear modulus from different models of hybrid imaging.

Inverse problems in MRI.

Imaging velocity fields by phase-contast MRI has limitations, some of them are:

- Since the phase is a number in the interval $]-\pi, \pi]$, a wrong choice of the VENC parameter causes aliasing, that is, there are pixels corresponding to jumps with respect to the true velocity. This is because the PC-MRI velocity satisfies $|u_{pc}| \leq |\mathrm{VENC}|$, so the true velocity has to be less than |VENC| to avoid aliasing.
- The usual way to reduce the above limitation is to increase the VENC, but this adds noise to the image, since VENC$\propto$VNR (veloticty-to-noise ratio).

In Chapter 2 a method (Optimal Dual-VENC, ODV) for tackling these limitations is proposed, in order to augment the range of velocities measured while keeping a low noise level. The approach uses dual-VENC measurements combined with appropriate cost function optimization having the form:

$$J(u) = \frac{1}{2}\sum_{j=1}^{2} |e^{i\hat{\vartheta}^{G_j}} - e^{i\vartheta^{G_j}(u)}|^2$$

where for $j = 1, 2$, $\hat{\vartheta}^{G_j} = \hat{\varphi}^{G_j} - \hat{\varphi}^{G_0}$ is the "measured" velocity dependent phase and $\vartheta^{G_j}(u)$ its model depending on the velocity u. The VENCs involved are defined from the pairs (G_0, G_1) and (G_0, G_2), respectively. Experiments are performed with a phantom and with volunteers in order to verify the theoretical results.

Main Result: *The global minimum of J in a "reasonable domain" (explained in Section 2.2.6) gives a new recovered velocity u_{ODV} which is not aliased even if the* VENC*'s involved are less than the true velocity, keeping a low noise.*

On the other hand, the limitations described above are also present in imaging harmonic displacements. The adaptation of the method presented in Chapter 2 is developed to deal with harmonic displacements by MRI, and issues related with MRE are discussed. Experiments with a phantom are performed in order to confirm the theoretical results. This is presented in Chapter 3.

Inverse problems in elasticity.

Most of the inverse problems in elasticity have been mathematically studied in the frame of linear elasticity with linear measurements. In Chapter 4 the inverse problem of the recovery of the shear modulus μ is studied from the following models where $\Omega \subset \mathbb{R}^d$ is a bounded domain with smooth boundary, and u_j is the displacement field corresponding to the j-th measurement, where $j = 1, \ldots, J$ and J is the number of measurements:

- Linear elasticity in harmonic regime with frequency ω, with elastic energy density measurements: that is, the model reads

$$\begin{cases} \omega^2 u_j + 2\nabla \cdot \mu \nabla^S u_j &= -\nabla p_j \quad \text{in } \Omega, \\ \nabla \cdot u_j &= 0 \quad \text{in } \Omega, \\ u_j &= g_j \quad \text{on } \partial\Omega, \end{cases}$$

  and is coupled to measurements given by:

$$\frac{\mu}{2}|\nabla^S u_j|^2 = H_j \quad \text{in } \Omega.$$

  This problem is studied in dimension $d = 2$ assuming that the pressures p_j are known. In addition, a forcing term is added in the model equation, which is described by a differential operator of order at most 1.

- Saint-Venant model with internal measurements of the displacements, that is, the model becomes:

$$\begin{cases} (L_{\mu,\lambda} + N_{\mu,\lambda})u_j + \omega^2 u_j &= 0 \quad \text{in } \Omega, \\ u_j &= g \quad \text{on } \partial\Omega, \end{cases}$$

  where

$$\begin{aligned} L_{\mu,\lambda} u_j &= 2\nabla \cdot \mu \nabla^S u_j + \nabla(\lambda \nabla \cdot u_j), \\ N_{\mu,\lambda} u_j &= 2c_\tau \nabla \cdot (\mu \nabla u_j^{\mathrm{T}} \nabla u_j) + \nabla(\lambda |\nabla u_j|^2) \end{aligned}$$

  and c_τ is a constant in x. The measurements are given by:

$$u_j = H_j \quad \text{in } \Omega.$$

This problem is studied in dimension $d = 2, 3$. In addition, we study the case of linear elasticity with the same model of measurements, which is useful for the analysis of Saint-Venant model.

In each case, the ellipticity of the respective linearized system is studied, applying the curl operator in the models coupled to internal displacements measurements. Then, the resulting systems augmented with the respective measurements can be written by:

$$\begin{cases} \mathcal{L}v &= f \quad \text{in } \Omega, \\ \mathcal{B}v &= g \quad \text{on } \partial\Omega, \end{cases}$$

where $\mathcal{L}, \mathcal{B}$ are differential operators and $v = (\delta\mu, \{\delta u_j\}_{j=1}^J)$. Necessary definitions for the development of the chapter are given in Sections 4.2 and 4.3.

Main Results: *The following results are presented for each model:*

- *Ellipticity for the operator $\mathcal{L}(x, D)$, with $J = 2$ sets of measurements, that is, the principal symbol $\mathcal{P}(x, \xi)$ is a full rank matrix $\forall x \in \Omega$ and $\forall \xi \in \mathbb{R}^d \backslash \{0\}$. The ellipticity holds for certain conditions over the infinitesimal strain tensors $\nabla^S u_j$, where $j = 1, 2$. This is presented for the different models in Theorem 4.3, Corollary 4.1, Section 4.6.1 and Section 4.7.1.*

- *Lopatinskii condition for the operator $\mathcal{A} = (\mathcal{L}, \mathcal{B})$, and then the existence of a parametrix, wich gives a useful estimate in appropriate Sobolev spaces, showing injectivity of $\mathcal{A}$ except for a finite dimensional kernel. This is presented for the different models in Lemma 4.5, Theorem 4.4, Corollary 4.1, Section 4.6.2, and Section 4.7.2.*

- *A stability estimate which allows to show that the kernel mentioned above is trivial. As a consecuence, it is possible to define the inverse of $\mathcal{A}$. In the case of elastic energy density, it is necessary a lower bound for the frequency ω. This is presented for the different models in Theorem 4.5, Lemma 4.2, Section 4.6.3 and Section 4.7.2.*

- *The existence of $\mathcal{A}^{-1}$ allows to define an iterative algorithm for the recovery of μ, which is presented and its convergence is shown. See Sections 4.4.5, 4.5.3 and 4.7.3*

Chapter 2

Optimal Dual-VENC (ODV) Unwrapping in Phase-Contrast MRI

The content of this chapter was published in H. Carrillo, A. Osses, S. Uribe, C. Bertoglio. "Optimal Dual-VENC (ODV) Unwrapping in Phase-Contrast MRI". In: *IEEE transactions on medical imaging* (2019) 38(5), 1263-1270. [Car+18]

2.1 Introduction

Velocity-encoded Phase-Contrast MRI (PC-MRI) is a well-established method for measuring flow velocities, with several applications to quantitative analysis of cardiovascular pathologies [Sri+09]. The velocity-encoding magnetic gradients are set by the choice of the velocity encoding parameter, or VENC [Dyv+15]. It is well known that the velocity-to-noise-ratio (VNR) worsens when increasing the VENC. However, if VENC is set lower than the true velocity (which is unknown prior to the scan), velocity aliasing occurs. Moreover, even for VENC values slightly larger than the true velocity, velocity aliasing may occur due to measurement noise. These restrictions motivate in clinical practice to acquire images at different VENCs, obligating the MRI operator to manually select the image for one specific VENC, while the aliased images are ignored and the time spent is squandered.

Velocity aliasing is one of the main limitations for measuring complex features of blood flows, particularly, when high and low velocities are present in the same image, such as in heart, valvular and vascular malformations.

Then, VENC has to be set high, but as a consequence, low VNR is present in low velocity regions, for instance in recirculation regions in aneurisma or false lumen in dissections, to name a few. This leads to significant inaccuracies when further analysis of the flow is performed [Cal+16]. Aliasing is also problematic in many PC-MRI techniques, like Tissue Phase Mapping [Pet+06] and Elastography [HSB17], where the motion magnitudes vary across the regions of interest.

In order to reduce aliasing artefacts, unwrapping algorithms have been developed by assuming that the velocity field is smooth in space and/or time, see e.g. [Loe+16] and references therein. Nevertheless, they often fail when the aliased regions are large. Therefore, voxelwise dual-VENC strategies have been proposed, i.e. without any assumption on smoothness of the flow [LPP95; Net+12; Ha+16; Cal+16; Sch+17]. They have been based on unwrapping low-VENC data by using the high-VENC reconstruction, which is assumed aliasing-free. While

actual approaches allow to improve the VNR with respect to a single high-VENC acquisition, they fail when the high-VENC data is aliased. Also, there is a lack of mathematical support for choosing the low- and high-VENCs. All of these issues limits the applicability of dual-VENC techniques, particularly when the peak velocities are uncertain.

Therefore, the aim of this work is to provide a mathematical framework to obtain aliasing-free velocity estimations from dual-VENC data, even when the both VENC acquisitions are aliased. The key is the least-squares formulation of the PC-MRI problem, whose mathematical properties allow to propose optimal combinations of VENCs to achieve this goal. We also present a numerical algorithm for dual-VENC reconstructions, which is successfully applied to numerical, experimental and volunteer data sets.

2.2 Theory

2.2.1 Classical PC-MRI

Assuming a constant velocity field, the usual starting point of classical PC-MRI is the model for the phase of the transverse magnetization at the echo-time [LPP95]:

$$\varphi^G = \varphi^0 + \vartheta^G \tag{2.1}$$

with $\varphi^0 \in [0, 2\pi)$ the reference phase, and

$$\vartheta^G = \vartheta^G(u) = \gamma u m_1(G) \tag{2.2}$$

the velocity dependent phase. Here, $u \in \mathbb{R}$ the flow velocity component parallel to the velocity-encoding gradient $G = G(t) \in \mathbb{R}$, with t the encoding time, and $m_1(G) \in \mathbb{R}$ the first-order moment of $G(t)$. The constant $\gamma > 0$ is the giromagnetic ratio.

From now on, we deal with different gradients G_i with different amplitudes. Assuming that we have measured two phases φ^{G_0} and φ^{G_1} with $G_0 \neq G_1$, the *phase-contrast* velocity is estimated by

$$u_{pc} := \frac{\varphi^{G_0} - \varphi^{G_1}}{\pi} \mathrm{VENC}(G_0, G_1), \tag{2.3}$$

with

$$\mathrm{VENC}(G_0, G_1) = \frac{\pi}{\gamma(m_1(G_0) - m_1(G_1))}.$$

In the case that the true velocity $|u_{true}| \leq |\mathrm{VENC}|$, then $u_{pc} = u_{true}$. But if $|u_{true}| > |\mathrm{VENC}|$, the phase difference exceeds $\pm\pi$ and aliasing occurs, i.e. $u_{true} \neq u_{pc}$. However, increasing the VENC decreases the VNR. Therefore, choosing the VENC parameter is an iterative manual process trying to set it as small as possible to maximize VNR and at the same time large enough to avoid aliasing.

2.2.2 Dual-VENC approaches

It is well known that for any VENC value, u_{true} belongs to the set of infinite but numerable solutions of type

$$u_{pc} + 2k\mathrm{VENC}(G_0, G_1),\ k \in \mathbb{Z}. \tag{2.4}$$

Therefore, it is natural to extend the velocity estimation problem such that k can be also estimated using additional encoding gradient measurements.

Assuming that now three measurements with gradients $G_0 = 0 < G_1 < G_2$ are available, two velocities at different VENC values can be reconstructed: the phase-contrast velocity u_1 at $\text{VENC}_1 = \text{VENC}(G_1, 0)$ and a set of velocities $u_2 + 2k\text{VENC}_2$ at $\text{VENC}_2 = \text{VENC}(G_2, 0)$, with $\text{VENC}_1 > \text{VENC}_2$, $k \in \mathbb{Z}$, where u_2 is obtained by phase-contrast at VENC_2. Standard dual-VENC unwrapping strategies, see e.g. [Sch+17; LPP95], aim to find the correct low-VENC velocity from an un-aliased high-VENC velocity u_1. Hence, an improved VNR should be achieved. Here, we will compare our new dual-VENC approach against the one from [Sch+17], which is defined as:

$$u_{\text{SDV}} = \begin{cases} u_2 + 2 \cdot \text{VENC}_2 & \text{if } \epsilon_1 < D < \epsilon_2 \\ u_2 - 2 \cdot \text{VENC}_2 & \text{if } -\epsilon_2 < D < -\epsilon_1 \\ u_2 + 4 \cdot \text{VENC}_2 & \text{if } \epsilon_3 < D < \epsilon_4 \\ u_2 - 4 \cdot \text{VENC}_2 & \text{if } -\epsilon_4 < D < -\epsilon_3 \end{cases}$$

with $D = u_1 - u_2; \epsilon_1 = 1.6 \cdot \text{VENC}_2; \epsilon_2 = 2.4 \cdot \text{VENC}_2;$
$\epsilon_3 = 3.2 \cdot \text{VENC}_2; \epsilon_4 = 4.8 \cdot \text{VENC}_2$. In the reminder of this article, we will denote it as *standard* dual-VENC (SDV).

Note that the SDV reconstruction will be aliased if $|\text{VENC}_1| < |u_{true}|$. The new dual-VENC method based on our analysis will overcome this issue by optimally choosing both VENC_1 and VENC_2 based on a reformulation of the phase-contrast problem presented next.

2.2.3 Least-squares formulation of the single-VENC problem

For a given velocity encoding gradient G let us denote the measured phase of transverse magnetization by $\hat{\varphi}^G$.

Assume now that we have available two measurements: a reference one for $G = 0$, and another for $G \neq 0$. We formulate the velocity reconstruction as a standard maximum-likelihood estimation problem from the phase measurements, by means of the least-squares function

$$\begin{aligned} J_G(u) &= \frac{1}{2}|e^{i\hat{\vartheta}^G} - e^{i\vartheta^G(u)}|^2 \\ &= \frac{1}{2}\Big(\cos(\hat{\vartheta}^G) - \cos(\vartheta^G(u))\Big)^2 \\ &\quad + \frac{1}{2}\Big(\sin(\hat{\vartheta}^G) - \sin(\vartheta^G(u))\Big)^2 \qquad (2.5) \\ &= \Big(1 - \cos\Big(\hat{\vartheta}^G - \vartheta^G(u)\Big)\Big) \qquad (2.6) \end{aligned}$$

with $\hat{\vartheta}^G = \hat{\varphi}^G - \hat{\varphi}^0$ the "measured" velocity dependent phase.

Least-squares formulations have also been recently applied in the context of unwrapping methods using the information of contiguous voxels for various types of single- and dual-VENC acquisitions [LE17]. However, no analysis of their properties or potential for optimizing the VENC combinations was reported.

Figure 2.1 shows examples of the functions $J_G(u)$, for different gradients represented by $\text{VENC}(G, 0)$. The synthetic measurements were generated with a unitary magnitude and the phases from Equation (2.1) using $\varphi^0 = \gamma B t_E$ with $B = 1.5\ T$, $\gamma = 267.513e3\ rad/T/ms$,

$t_E = 5\ ms$, a velocity $u_{true} = 1\, m/s$. It can be appreciated that the functions are periodic, with the period depending on the VENC, and also that the true velocity is a local minimum independent on the VENC. The following propositions proof these observations.

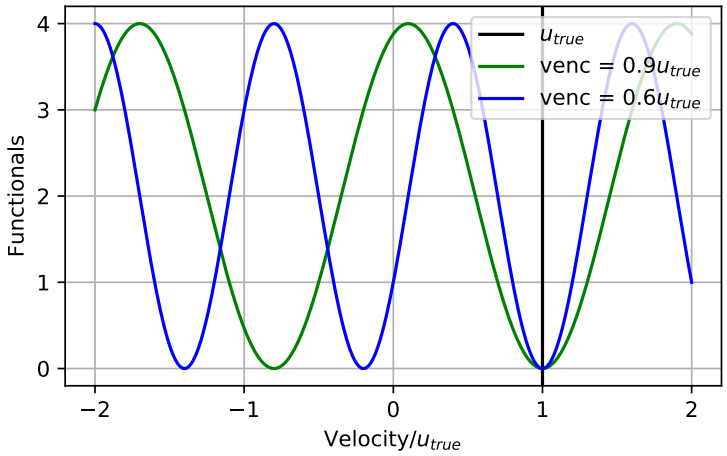

Figure 2.1: cost functions $J_G(u)$ for u_{true} and two VENC values.

Proposition 2.1. *$J_G(u)$ is a periodic function with period* $2\text{VENC}(G, 0)$.

Proof. It suffices to see that the cosine and sine are 2π-periodic functions, and

$$\begin{aligned} \vartheta^G(u + 2\text{VENC}(G,0)) &= \gamma(u + 2\text{VENC}(G,0))m_1(G) \\ &= \gamma u m_1(G) + 2\pi \\ &= \vartheta^G(u) + 2\pi \end{aligned}$$

□

Proposition 2.2. *The critical points u_k of $J_G(u)$ are*

$$u_k = \frac{\hat{\varphi}^G - \hat{\varphi}^0}{\gamma m_1(G)} + k\text{VENC}(G,0)\ ,\ k \in \mathbb{Z} \tag{2.7}$$

Proof. From (2.6) we see that

$$\frac{\partial J_G}{\partial u} = -\gamma m_1(G)\sin(\hat{\vartheta}^G - \vartheta^G). \tag{2.8}$$

At the critical points we must then have:

$$\sin(\hat{\vartheta}^G - \vartheta^G) = 0 \iff \vartheta^G(u_k) = \hat{\vartheta}^G + k\pi, \quad k \in \mathbb{Z}. \tag{2.9}$$

Finally, using Equation (2.2) we obtain

$$u_k = \frac{\hat{\varphi}^G - \hat{\varphi}^0}{\gamma m_1(G)} + k\frac{\pi}{\gamma m_1(G)}. \tag{2.10}$$

□

Proposition 2.3. *At the critical points of $J_G(u)$, the second derivatives are given by*

$$\frac{\partial^2 J_G}{\partial u^2}(u_k) = C \cdot (-1)^k,\ k \in \mathbb{Z}, C > 0.$$

Proof. Taking the derivative in (2.8) we obtain:

$$\frac{\partial^2 J_G}{\partial u^2}(u_k) = \gamma^2 m_1(G)^2 \cos(\hat{\vartheta}^G(u_k) - \vartheta_u^G) = C \cdot (-1)^k \tag{2.11}$$

where the last equality holds due to Equation (2.9). □

In conclusion, we have just proved that Equation (2.4) corresponds to the local minima of the cost function J_G by taking k as an even number in Equation (2.11).

It is also straightforward to show that the true velocity u_{true} belongs to the set of local minima of J_G when the measurements are noise-free. Indeed, in that case $\hat{\varphi}^G = \hat{\varphi}^0 + \gamma m_1(G) u_{true} + 2k\pi$, and if we choose $\varphi^G(u_{true}) = \hat{\varphi}^0 + \gamma m_1(G) u_{true}$, then $J_G(u_{true}) = 0$ from Equation (2.6).

2.2.4 The dual-VENC least squares problem

We assume now that we have measured the magnetization vector with three encoding gradients $G_0 = 0 < G_1 < G_2$. We can then define the dual-VENC least squares sum function as:

$$\begin{aligned} J_\Sigma(u) &= \frac{1}{2}\sum_{j=1}^{2} |e^{i\hat{\vartheta}^{G_j}} - e^{i\vartheta^{G_j}(u)}|^2 \\ &= \sum_{j=1}^{2} \left(1 - \cos\left(\hat{\vartheta}^{G_j} - \vartheta^{G_j}(u)\right)\right) \end{aligned}$$

Figure 2.2 shows the single- and dual-VENC least-squares functions for different VENC combinations $\text{VENC}_1 > \text{VENC}_2 = \beta\text{VENC}_1$, $0 < \beta < 1$. Hence, the VENCs can be set in terms of VENC_1 and β. Note that VENC_1 is set lower than u_{true} and is kept fixed in all plots, while β is variable. We can first observe that in all cases local and global minima are present in the dual-VENC functions $J_\Sigma(u)$. However, the true velocity is always a global minimum since it is a local and global minimum for each VENC, as shown in the previous section.

Remarkably, the periodicity of J_Σ is now the least common multiplier (lcm) between the periodicity of the single-VENC functions, i.e. $L_\Sigma := \text{lcm}(2\text{VENC}_1,\ 2\text{VENC}_2)$. As a consequence, if β is carefully chosen, as in Figure 2.2(a) and 2.2(b), J_Σ has a larger period than the original single-VENC functions, namely $L_\Sigma > 2\text{VENC}_1$. Therefore, even though $\text{VENC}_1, \text{VENC}_2 < |u_{true}|$, we can still distinguish u_{true} from the other global minima since they have larger absolute values.

However, if we do not choose β well, e.g. as in Figures 2.2(c) and 2.2(d), then $L_\Sigma = 2\text{VENC}_1$ and the global minima with smallest absolute value will not be u_{true} if $\text{VENC}_1 < u_{true}$ and velocity aliasing occurs. A general method for computing the aliasing limit is: for $\beta = \alpha/\alpha_0$, with $\alpha, \alpha_0 \in \mathbb{N}$ the smallest possible values, then it is easy to verify that the periodicity of J_Σ is $L_\Sigma = \alpha 2\text{VENC}_1$, since

$$L_\Sigma = k_1 2\text{VENC}_1 = k_2 2\beta\text{VENC}_1,\ k_1, k_2 \in \mathbb{Z}$$

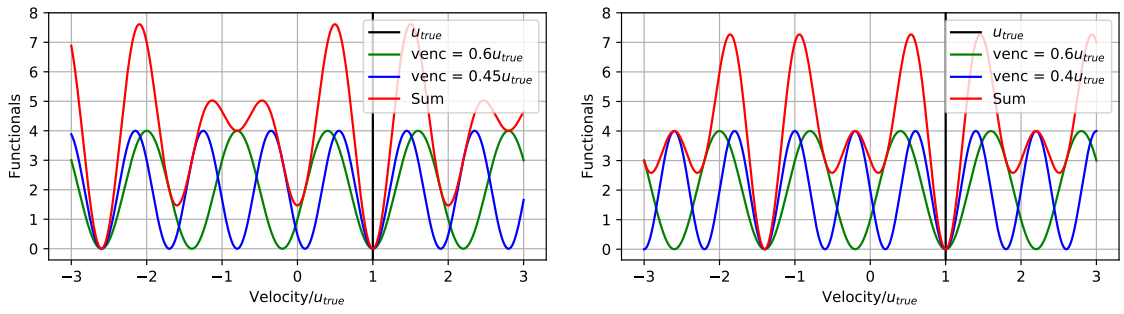

(a) $\beta = 0.75$

(b) $\beta = 0.66$

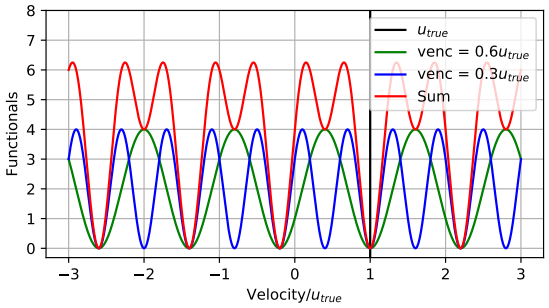

(c) $\beta = 0.5$

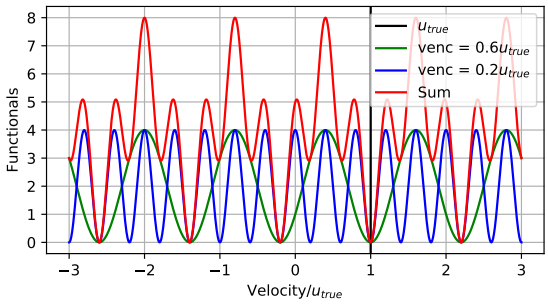

(d) $\beta = 0.33$

Figure 2.2: Cost functions $J_G(u)$ and $J_\Sigma(u)$ for different $\text{VENC}_1, \text{VENC}_2 = \beta\text{VENC}_1$.

leading to $k_1 = \alpha$, $k_2 = \alpha_0$. Then, aliasing will occur when $||u_{true}| - L_\Sigma/2| < |u_{true}|$, i.e. $\text{VENC}_1 < |u_{true}|/\alpha$.

Table 2.1 gives examples of VENC_1 such that the global minimum of J_Σ with lowest magnitude corresponds to u_{true} depending on β.

β	0.95	0.9	0.75	0.7	0.66	0.55	0.5
α	19	9	3	7	2	11	1

Table 2.1: Examples of aliasing limits for decreasing values of β. ODV method allows aliasing-free estimation if $\text{VENC}_1 > |u_{true}|/\alpha$.

2.2.5 Choice of β

As shown in Table 2.1, in the case without any measurement noise, to maximize the periodicity of J_Σ one should choose $\text{VENC}_2 \approx \text{VENC}_1$, making the aliasing velocity very small, or for instance $\beta = 0.7$ or $\beta = 0.55$ as indicated in Table 2.1.

However, the presence of noise deforms the dual-VENC functions, see Figure 2.3, since the noise is independent for each VENC. Therefore, local minima from both single-VENC cost functions that are not necessarily u_{true} can get close to each other. Hence, there is an increased risk for u_{true} not being global minima when α is large. In order to maximize the robustness to noise, the local minima of both single-VENC functions should be separated as much as possible. As shown in Figure 2.2(b), this is indeed the case for $\beta = 0.66$. For

$\beta = 0.75$ this separation is less pronounced, however $\beta = 0.75$ would allow to lower the aliasing velocity if noise is low. In general, the optimal choice of β should be optimized to the SNR of the specific MRI scanner, but $\beta = 0.66$ is always the most robust to noise due to the largest separation between minima. In the experiments, we will use these two values, $\beta = 0.66$ and $\beta = 0.75$. Additionally, in the experiments with numerical data, we will show the poor performance of $\beta = 0.7$ when noise is present.

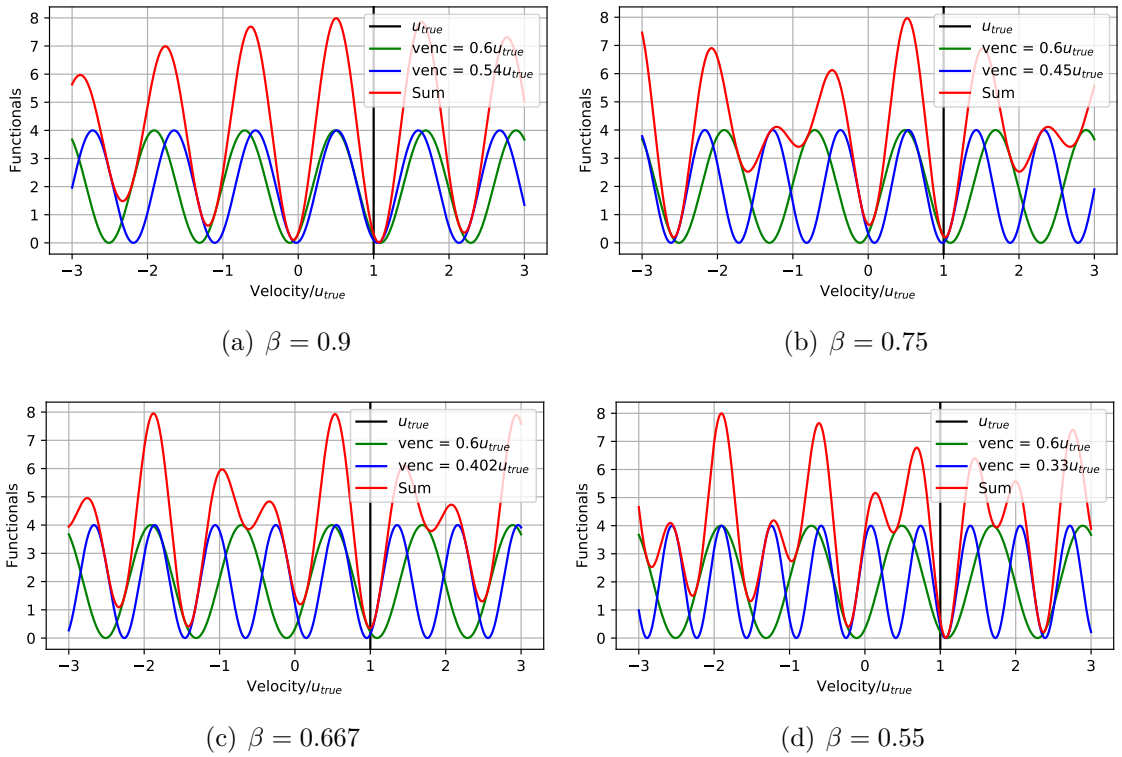

(a) $\beta = 0.9$ (b) $\beta = 0.75$

(c) $\beta = 0.667$ (d) $\beta = 0.55$

Figure 2.3: Cost functions $J_G(u)$ for different pair of values of VENC and the sum cost function J_Σ with noisy magnetization measurements (standard deviation 20% of magnitude).

2.2.6 The optimal dual-VENC (ODV) algorithm

Based on the considerations above, we now detail the ODV velocity estimation algorithm. For the given user-defined parameters VENC_1 and $\text{VENC}_2 = \beta\text{VENC}_1$, $0 < \beta < 1$:

1. Measure phases $\hat{\varphi}^{G_i}$ for three gradients: $G_0 = 0$ and G_1, G_2 such that $\text{VENC}(G_1, 0) = \text{VENC}_1$ and $\text{VENC}(G_2, 0) = \text{VENC}_2$.

2. Find the global minima u_k^*, $k \in \mathbb{Z}$:

$$u_k^* = \underset{u \in [-u_{max}, u_{max}]}{\operatorname{argmin}} J_\Sigma(u),$$

with $u_{max} = \text{lcm}(2\text{VENC}_1, 2\text{VENC}_2)/2$. The estimated dual-VENC velocity corresponds to u_k^* with smallest absolute value.

2.3 Methods

This section summarizes setups with three types of data: synthetic, phantom and volunteer. In all cases we applied the formula (2.3) for single-VENC and dual-VENC with both standard [Sch+17] (SDV) and new ODV methods. For the ODV algorithm, the global minima was found using a sampling of the cost function J_Σ with uniform spacing of the velocity of $\text{VENC}_2 \cdot 10^{-3}$, which was found to be small enough to avoid numerical artefacts in the global optimization.

2.3.1 Synthetic data

The reference phase is defined as $\varphi^0 = \gamma B_0 T_E$ with $B_0 = 1.5\ T$, $\gamma = 267.513e3\ rad/T/ms$, $T_E = 5\ ms$. For the phases of the non-zero flow encoding gradients, we consider $\varphi^{G_{1,2}} = \varphi^0 + u_{true}\pi/\text{VENC}_{1,2}$, with $u_{true} = 1m/s$. Using these phases, reference magnetization measurements were built assuming a unitary magnitude. The estimation is shown in terms of VENC_1 and $\text{VENC}_2 = \beta\text{VENC}_1$, with $\beta = \{0.66, 0.7, 0.75\}$.

We also compute estimations using magnetization measurements perturbed with an additive Gaussian noise with zero-mean and standard deviation of 20% of the magnitude. We express these results in terms of mean estimated velocity for 2000 realizations of the noise and twice the standard deviation.

2.3.2 Phantom data

In order to preliminarily assess the ODV we used a flow phantom that consisted of a rigid straight hose of 15mm internal diameter, 25mm external diameter. The hose was connected to a MRI-compatible flow pump (CardioFlow 5000 MR, Shelley Medical Imaging Technologies, London, ON, Canada) with a constant flow rate of 200 mL/s. The system was filled with a blood-mimicking fluid (40% distilled H2O, 60% Glycerol) and the set up was similar as in [Urb+16; Mon+17]. The MRI data sets were acquired on a clinical 1.5T Philips Achieva scanner (Philips, Best, The Netherlands). The protocol consisted of through-plane PC-MRI sequence with a single cardiac phase due to constant flow rate. The scan parameters were: in-plane resolution was 1x1 mm with a slice thickness of 8 mm, 1 prospective cardiac phase, FA = 12^o, TR=9.2 ms, TE=4.9 ms, matrix size = (256,256). The data was acquired using non-symmetric pairs of encoding gradients with VENC = $150, 100, 70$ cm/s with one surface coil. The acquisitions were performed using single-VENC protocols and the dual-VENC reconstructions were computed using only one of the zero-encoding gradients of the corresponding dual-VENC pair.

2.3.3 Volunteer data

Eight healthy volunteers underwent MRI in the same 1.5T Achieva scanner using a 5 elements cardiac coil. The protocol consisted of through-plane PC-MRI sequence perpendicular to the ascending aorta just above the valsalva sinus. We used several VENC values: 33.3, 37.5, 50, 66.7, 75, 100 and 150cm/s. These choices allow to generate dual-VENC reconstructions with both values of $\beta = 0.66$ and $\beta = 0.75$. The raw data was obtained and the reconstruction of each bipolar gradient was performed offline using matlab. Data from the multiple coils were combined using the method proposed in [Ber+94]. The data was acquired using the following

scan parameters: in-plane resolution was 1x1 mm with a slice thickness of 8 mm, 25 cardiac phases using prospective ECG triggering, FA = 15^o, TR=5.5 ms, TE=3.7 ms, matrix size = (320, 232). Temporal resolution depended on the heart rate of the patients, varying between 35ms to 48 ms.

As in the panthom, the acquisitions were performed using single-VENC protocols. One issue with this approach is that the TE may be different depending in the scan setting, particularly may increase for low VENCs [BSP92]. Since we use only the reference phase of VENC_1, the value of the reference phase used in the dual-VENC reconstructions for VENC_2 was scaled by $T_E^{(2)}/T_E^{(1)}$, with $T_E^{(1)}$ and $T_E^{(2)}$ the echo times given by acquisitions with VENC_1 and VENC_2, respectively. This is justify simply by the knowledge about the reference phase being proportional to T_E [Bro+14].

2.4 Results

2.4.1 Synthetic data

Figure 2.4 shows the estimated velocity against VENC_1 without noise, confirming the unwrapping properties of both dual-VENC approaches: for SDV aliasing occurs when $\text{VENC}_1 < u_{true}$, and for ODV when $\text{VENC}_1 < u_{true}/2$, $\text{VENC}_1 < u_{true}/7$ and $\text{VENC}_1 < u_{true}/3$ with $\beta = 0.66$, $\beta = 0.7$ and $\beta = 0.75$, respectively.

Similar results for noisy measurements are presented in Figure 2.5, now including the aforementioned confidence interval. As one expects, the spread of the estimations are lower for $\beta = 0.66$. Moreover, in the single-VENC cases we confirm that aliasing starts even before the theoretical value due to the noise. This is also evident for SDV, while ODV is clearly more robust. We can also see that for ODV and $\beta = 0.7$ the confidence interval does not decrease uniformly with VENC_1 due to the nondesirable effect of overlapping of the single-VENC least squares functions mentioned in Section 2.2.5. A similar, but less pronounced effect, occurs with $\beta = 0.75$. Therefore, in the real data acquisitions we continue using only $\beta = 0.66$ and $\beta = 0.75$.

2.4.2 Phantom data

The results for the phantom experiments are presented in Figure 2.6. The peak velocity in the tube is about 120 cm/s, what can be inferred from the single-VENC image with $\text{VENC}_1 = 150$. The wall of the tube can be distinguish as the noise ring separating the flow and the surrounding zero-velocity fluid. We first show the single-VENC PC-MRI, where aliasing for the two smaller VENCs can be clearly appreciated. We also confirm that SDV cannot handle the aliasing when both VENC values are lower than the true velocity, while ODV is able to sucessfully reconstruct un-aliased images from two aliased ones.

2.4.3 Volunteers data

Figure 2.7 presents the velocity profiles on the descending aorta for the different VENC combinations and different reconstruction methods for Volunteer 5. The figures for all the volunteers can be found in the Supplementary Material 2.A.

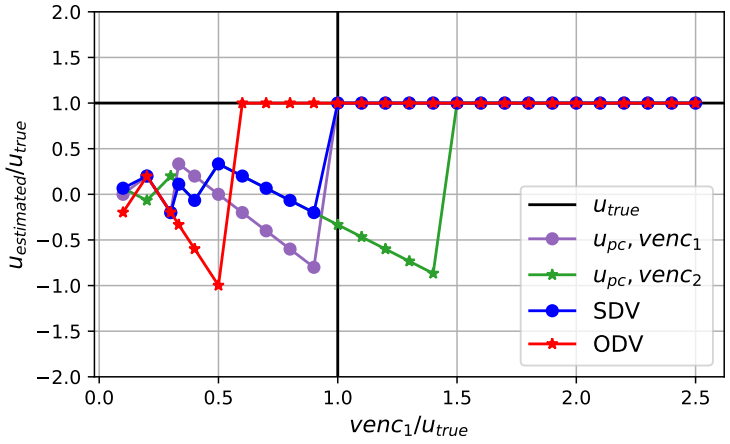

(a) $\beta = 0.667$

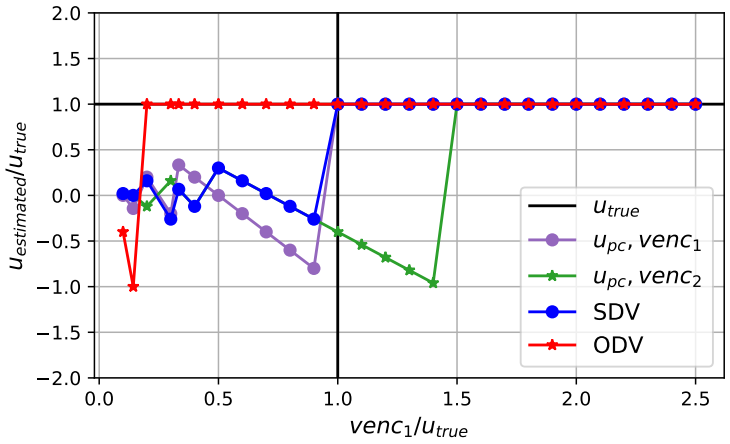

(b) $\beta = 0.7$

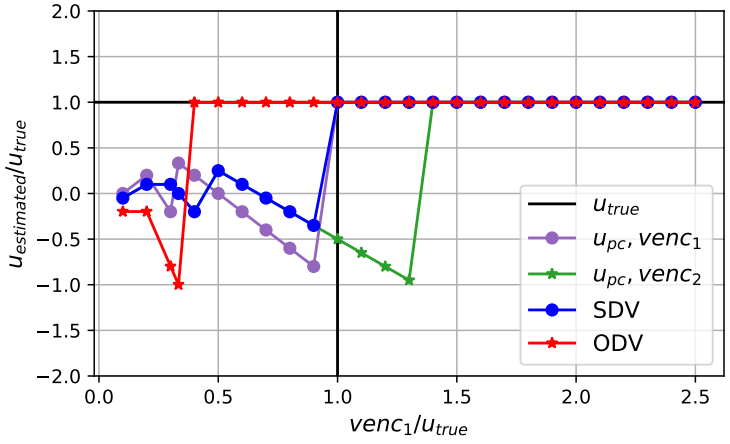

(c) $\beta = 0.75$

Figure 2.4: Synthetic data (noise-free): single- and dual-VENC.

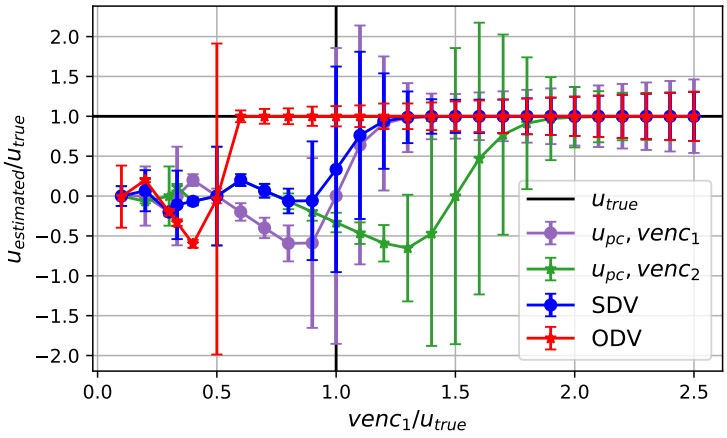

(a) $\beta = 0.667$

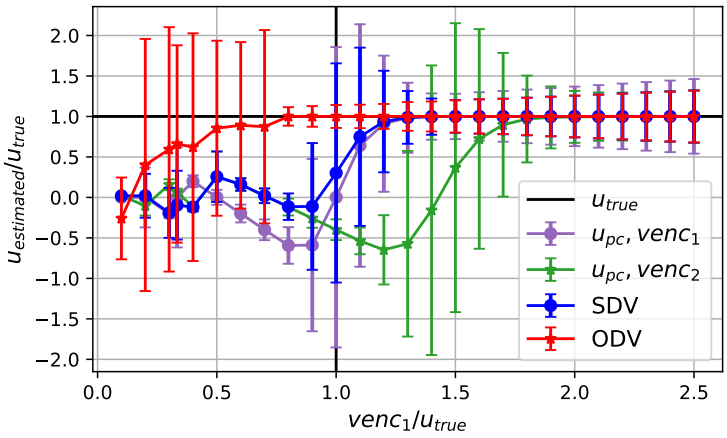

(b) $\beta = 0.7$

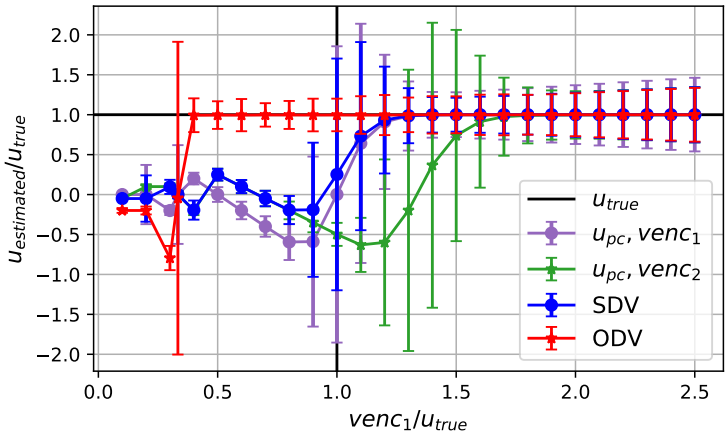

(c) $\beta = 0.75$

Figure 2.5: Synthetic data (20% noise): single- and dual-VENC.

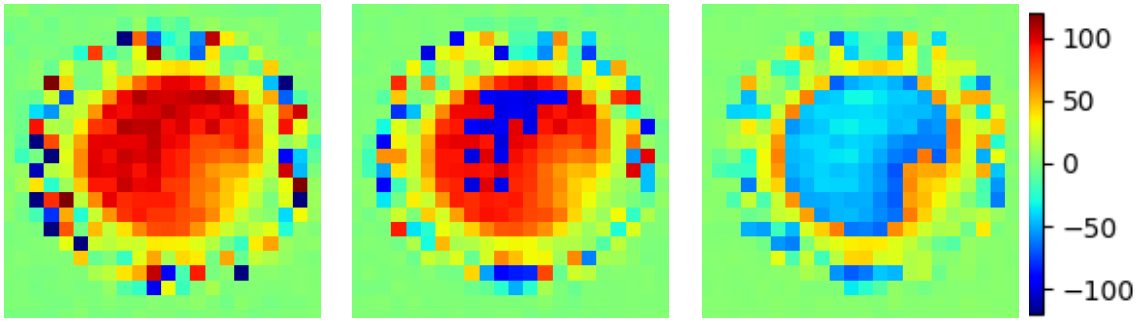

(a) PC 150 (b) PC 100 (c) PC 70

(d) SDV $150, 100$ (e) SDV $150, 70$ (f) SDV $100, 70$

(g) ODV $150, 100$ (h) ODV $150, 70$ (i) ODV $100, 70$

Figure 2.6: Phantom data: single- (PC) and dual-VENC.

In all our results in volunteers it is confirmed that ODV is the most robust method when decreasing the VENC, allowing to reconstruct velocities using lower VENCs than the true velocity, in contrast to SDV. Moreover, the theory is verified: aliasing is practically inexistent for $(\text{VENC}_1, \text{VENC}_2) = (50, 37.5)$ ($\beta = 0.75$), while aliasing always occurs at $(50, 33.3)$ ($\beta = 0.66$). Indeed, the peak velocity is approximately 130 cm/s, for $\beta = 0.75$, $\text{VENC}_1 = 50 > 130/3 \approx 40$, hence no aliasing appears. For $\beta = 0.66$, $\text{VENC}_1 = 50 < 130/2 \approx 65$, hence aliasing appears. The actual noise level of the acquisition seems to not affect the performance of the ODV with $\beta = 0.75$.

Figure 2.8 summarises the ODV results for all volunteers when varying the VENC. The error is computed in terms of the ℓ^2-norm for the voxels inside the lumen, relative to the ℓ^2-norm of the reference image (average of VENC 150 cm/s with 3 repetitions).

Finally, Figure 2.9 shows the standard deviation of the estimated velocities on a static tissue (thoracic muscle) in terms of the VENC for all single- and dual-VENC methods.

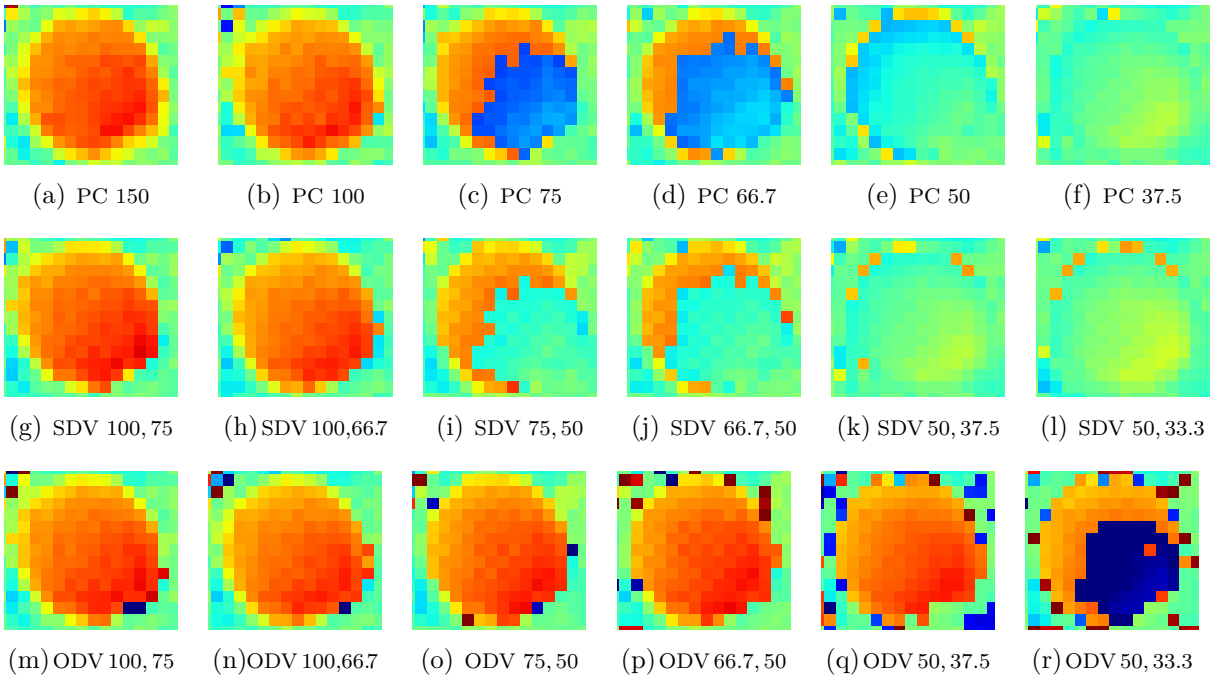

(a) PC 150 (b) PC 100 (c) PC 75 (d) PC 66.7 (e) PC 50 (f) PC 37.5

(g) SDV 100, 75 (h) SDV 100,66.7 (i) SDV 75, 50 (j) SDV 66.7, 50 (k) SDV 50, 37.5 (l) SDV 50, 33.3

(m) ODV 100, 75 (n) ODV 100,66.7 (o) ODV 75, 50 (p) ODV 66.7, 50 (q) ODV 50, 37.5 (r) ODV 50, 33.3

Figure 2.7: Volunteer 5. First row: single-VENC PC-MRI. Second row: SDV. Third row: ODV. Velocities are colored as in Figure 2.6. Numbers indicate the VENC(s).

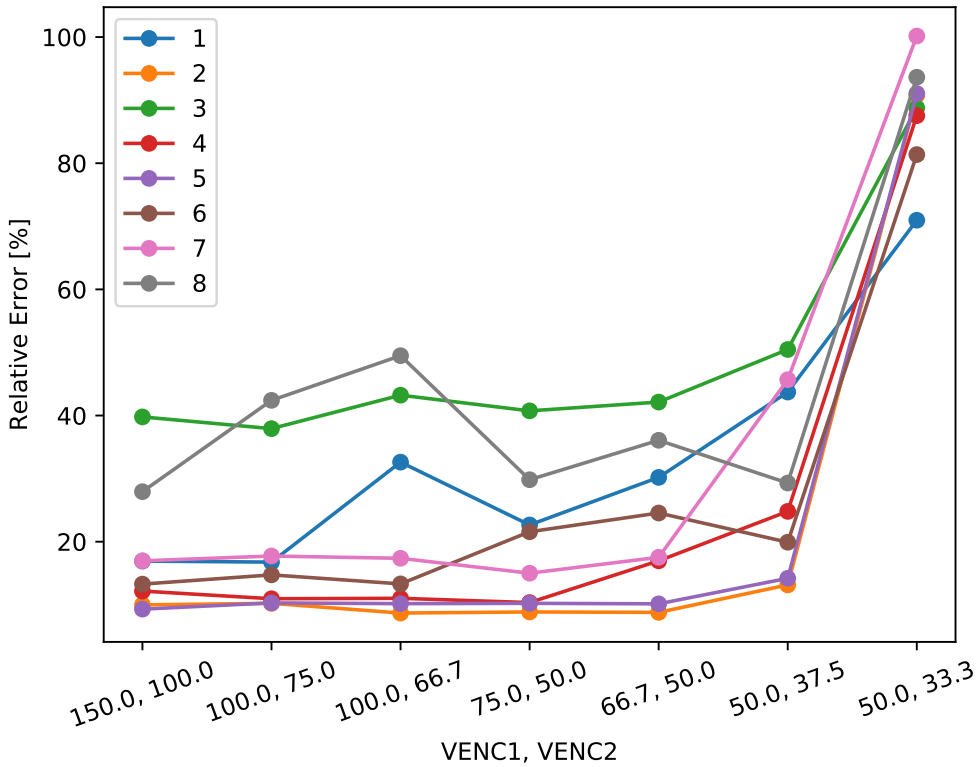

Figure 2.8: Volunteers 1 to 8: $(\text{VENC}_1, \text{VENC}_2)$ v/s relative error between ODV and reference.

Analogous results are obtained for all volunteers (see Supplementary Material). Here, results need to be carefully analyzed and interpreted. Therefore, we present two sets of dual-VENC reconstructions: one with three encoding gradients as described above scaling the reference phase with the echo times, and another using four encoding gradients, i.e., where the reference phase of each VENC was used and therefore no scaling is needed.

First, we can see that noise decreases with VENC in the single-VENC reconstructions, and that the standard deviation is larger for VENC_1 than for VENC_2, as expected. For the both dual-VENC approaches, this is also the case for $\text{VENC}_2 > 50$ cm/s. The ODV using three gradients (ODV(3)) gives also a standard deviation close to VENC_2. Also as expected, the SDV using four gradients (SDV(4)) gives exactly the same results as VENC_2.

For $\text{VENC}_2 \leq 50$, the standard deviation of both dual-VENC approaches shows jumps when using three gradients, while it monotonically decreases when using four gradients. A possible reason is the scaling of the reference phase for VENC_2. Indeed, for VENC > 50 T_E stays fixed, hence no scaling is applied. But for VENC ≤ 50 the T_E is automatically changed. The differences in the curves for SDV(3) (i.e. with scaling) and SDV(4) (i.e. no scaling) are more evidence pointing in this direction. Therefore, this problem is most likely to be related to the acquired data but not to the ODV or SDV reconstruction methods. We are currently working in dual-VENC acquisition protocols using only three gradients, which should avoid this issue.

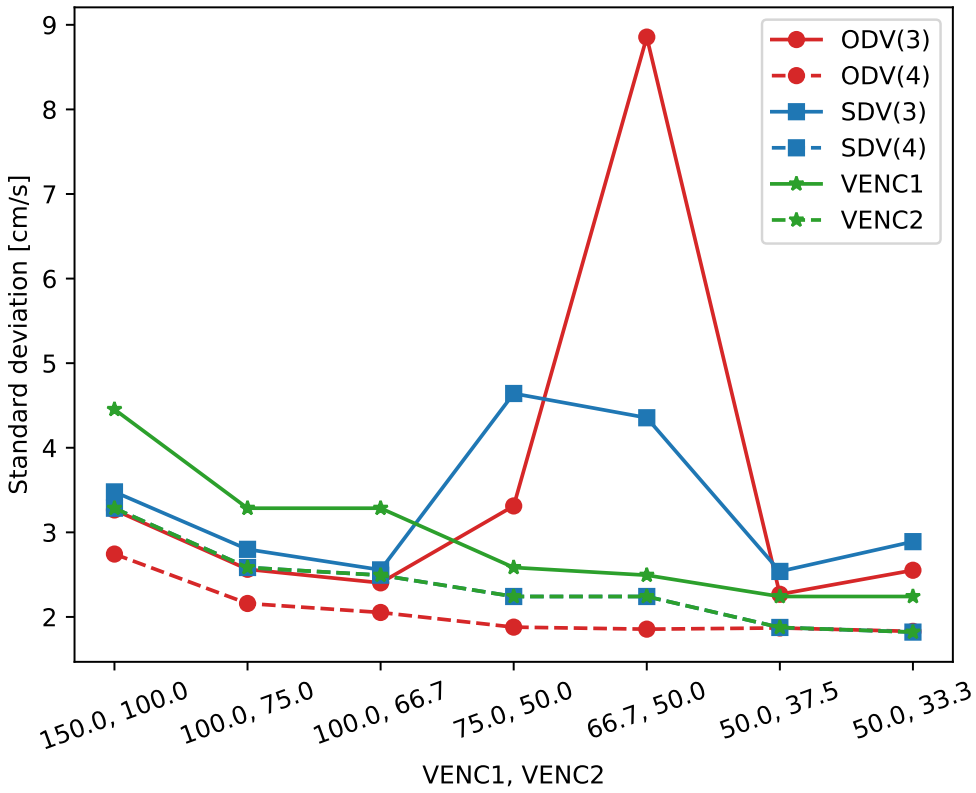

Figure 2.9: Volunteer 5: $(\text{VENC}_1, \text{VENC}_2)$ v/s standard deviation of estimated velocity in static tissue.

2.5 Discussion

In this work, we present a method for reconstructing velocities using dual-VENC images, for the first time in the literature when both single-VENC images are aliased. The main advantage of the method is that the true velocity does not need be known exactly in advance, since aliasing is allowed for both VENCs. All previous works have proposed to unwrap low-VENC images using high-VENC images without aliasing [LPP95; Net+12; Ha+16; Cal+16; Sch+17]. The theoretical findings are confirmed in real data sets from an experimental phantom and volunteers.

The choice of the VENC's ratio $\beta = 0.66$ is the most robust to noise, independent on the MRI scanner settings. However, for the volunteers scanned here, $\beta = 0.75$ works satisfactory and therefore it allows lower aliasing limits for the ODV estimations than $\beta = 0.66$, as given by the theory. Let us recall that β can be kept fixed (for instance, optimized once for typical scan settings), while the scanner user only needs to choose VENC_1 as in a single-VENC acquisition.

Note that unwrapping methods using contiguous voxels - like the ones from [LE17] - can be still applied after the estimation with ODV. The unwrapping would then probably perform better due to the larger periods of the candidate solutions, e.g. $L_\Sigma = 6\text{VENC}_1$ for $\beta = 0.75$ and $L_\Sigma = 4\text{VENC}_1$ for $\beta = 0.667$.

Concerning the limitations of our study, the method was not assessed in patients, only in volunteers. It is well known that dual-venc approaches (as any other cardiovascular MRI sequences) are challenging due to variabilities during the experiment (not only measurment noise) [LPP95], such as cardiac rhythm changes and subjects' motion. However, this variability will impact in similar manner the standard dual-VENC approach as well as the method proposed here. Another limitation is that data acquisition was performed for the two VENCs in a serial fashion, and therefore MRI scan protocols tailored to the ODV reconstructions have to be developed yet. This could be also done by including k-space undersampling techniques as in [Net+12], what would allow dual-VENC protocols comparable in scan time to single-VENC ones, what is of high interest for the application of ODV to 4Dflow. Moreover, as in standard PC-MRI, there is the implicit assumption that the velocity is constant in space and time and therefore, neither the single- nor the dual-VENC approaches count for effects like dephasing of spins and turbulence.

2.6 Conclusion

We present a robust method for estimating velocities from dual-VENC data in PC-MRI. The main contribution of this work is that both a theoretical and an extensive empirical analysis was carried out, turning out that there are high- and low-VENC combinations that can considerably reduce the aliasing issues. For example, in the volunteer data the ODV allows to choose the high-VENC up to a third of the maximal velocity. In clinical practice, the scanner operator has only to choose a single expected velocity, as for standard single-VENC PC-MRI. Then, the low-VENC value can be automatically fixed by the scanner in terms of the high-VENC. Moreover, the reconstruction method is simple enough to be implemented directly in the MRI scanner. Next steps are to assess the ODV in cases with high velocity variability, like stenotic vessels or valves, and 4Dflow, and application to other phase-contrast techniques, like elastography.

Appendix

2.A Supplementary material

In this appendix of Chapter 2 we show the velocity profiles on the descending aorta for the different VENC combinations and different reconstruction methods for eight volunteers. The profiles are shown in Figures 2.10, 2.11, 2.12, 2.13, 2.14, 2.15, 2.16, 2.17.

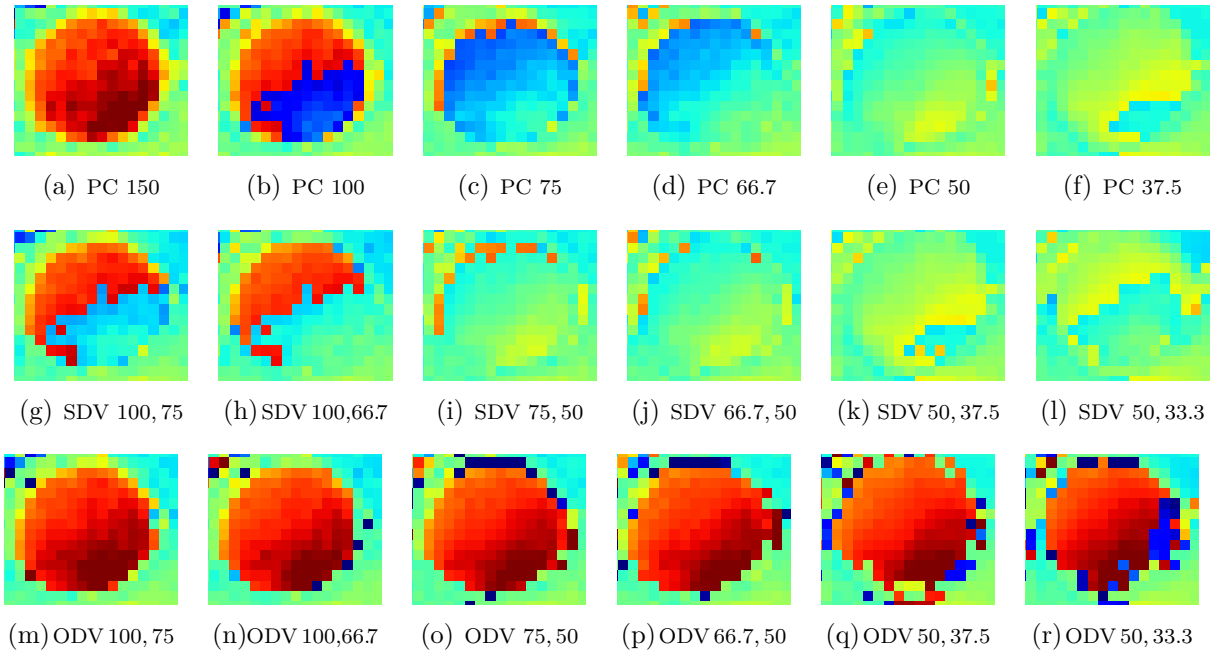

(a) PC 150 (b) PC 100 (c) PC 75 (d) PC 66.7 (e) PC 50 (f) PC 37.5

(g) SDV 100, 75 (h) SDV 100,66.7 (i) SDV 75, 50 (j) SDV 66.7, 50 (k) SDV 50, 37.5 (l) SDV 50, 33.3

(m) ODV 100, 75 (n) ODV 100,66.7 (o) ODV 75, 50 (p) ODV 66.7, 50 (q) ODV 50, 37.5 (r) ODV 50, 33.3

Figure 2.10: Volunteer 1. First row: single-VENC PC-MRI. Second row: SDV. Third row: ODV. Velocities are colored as in Figure 2.6. Numbers indicate the VENC(s).

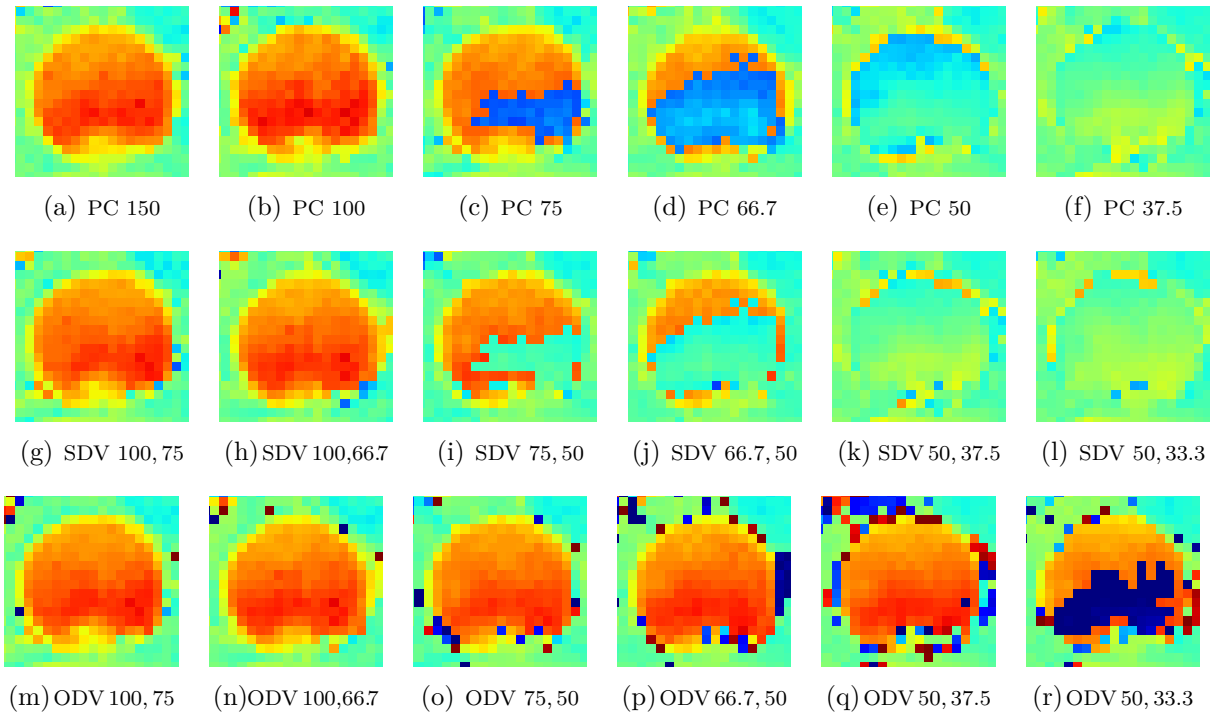

(a) PC 150 (b) PC 100 (c) PC 75 (d) PC 66.7 (e) PC 50 (f) PC 37.5

(g) SDV 100, 75 (h) SDV 100,66.7 (i) SDV 75, 50 (j) SDV 66.7, 50 (k) SDV 50, 37.5 (l) SDV 50, 33.3

(m) ODV 100, 75 (n) ODV 100,66.7 (o) ODV 75, 50 (p) ODV 66.7, 50 (q) ODV 50, 37.5 (r) ODV 50, 33.3

Figure 2.11: Volunteer 2. First row: single-VENC PC-MRI. Second row: SDV. Third row: ODV. Velocities are colored as in Figure 2.6. Numbers indicate the VENC(s).

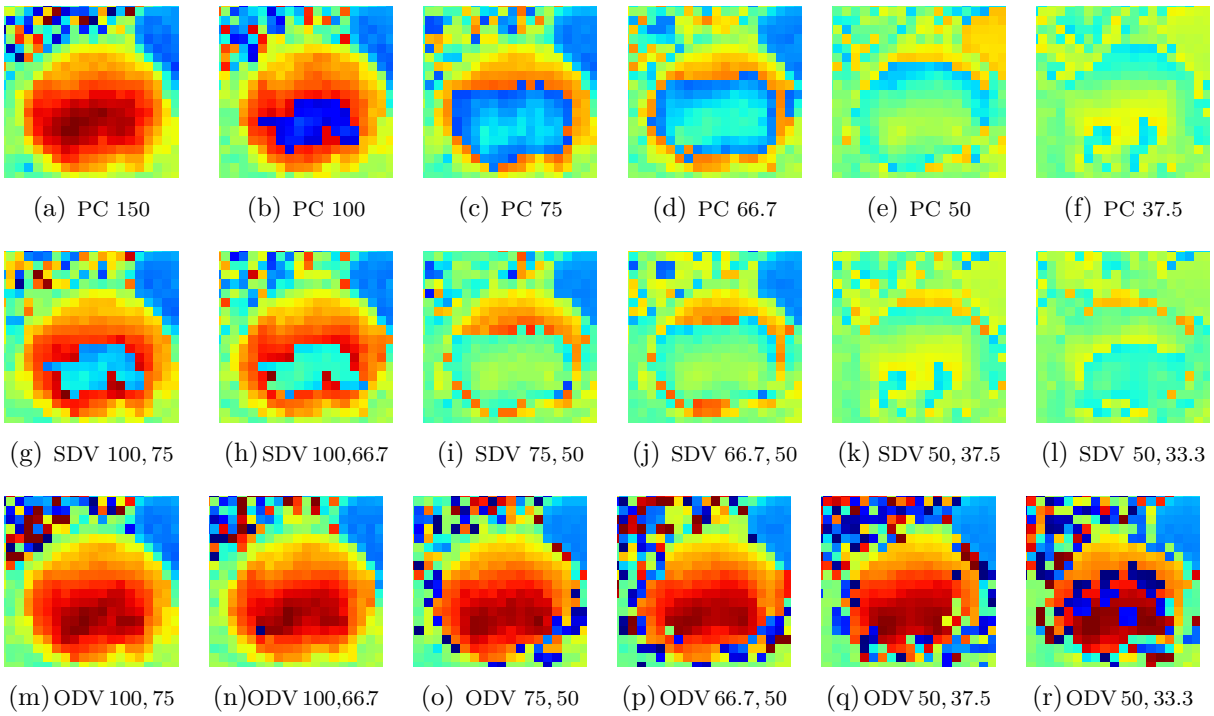

(a) PC 150 (b) PC 100 (c) PC 75 (d) PC 66.7 (e) PC 50 (f) PC 37.5

(g) SDV 100, 75 (h) SDV 100,66.7 (i) SDV 75, 50 (j) SDV 66.7, 50 (k) SDV 50, 37.5 (l) SDV 50, 33.3

(m) ODV 100, 75 (n) ODV 100,66.7 (o) ODV 75, 50 (p) ODV 66.7, 50 (q) ODV 50, 37.5 (r) ODV 50, 33.3

Figure 2.12: Volunteer 3. First row: single-VENC PC-MRI. Second row: SDV. Third row: ODV. Velocities are colored as in Figure 2.6. Numbers indicate the VENC(s).

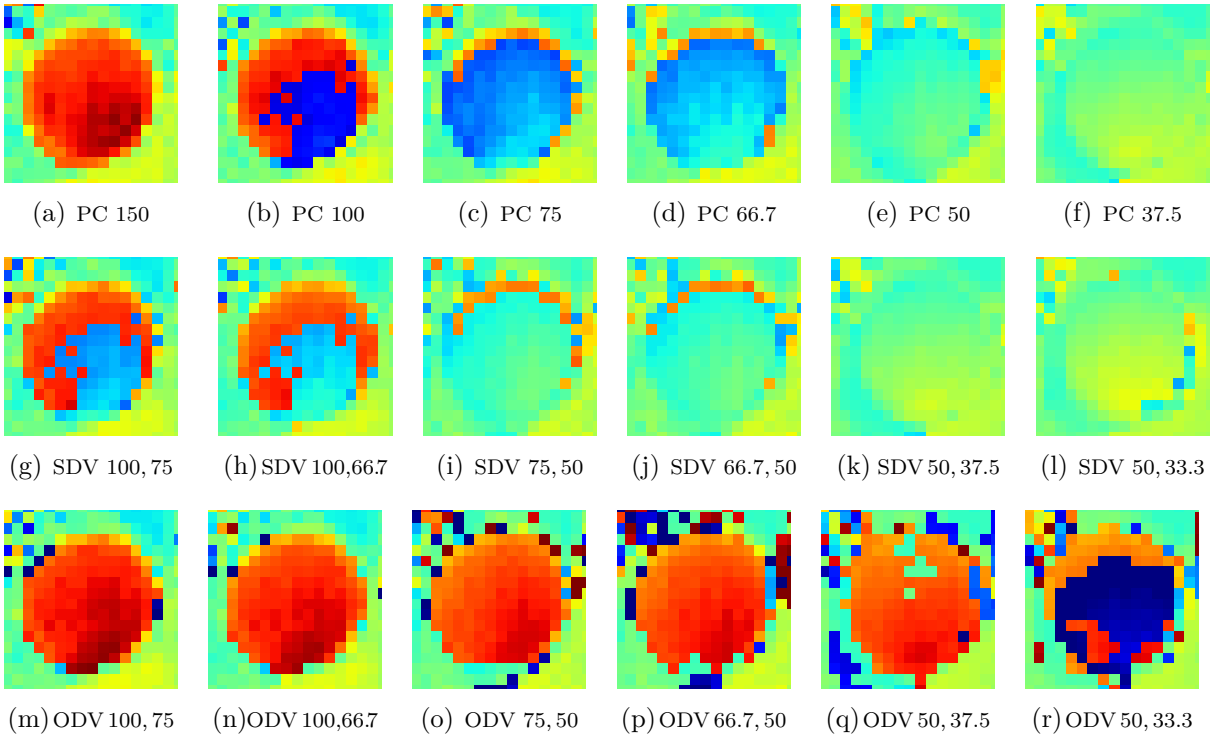

(a) PC 150 (b) PC 100 (c) PC 75 (d) PC 66.7 (e) PC 50 (f) PC 37.5

(g) SDV 100, 75 (h) SDV 100,66.7 (i) SDV 75, 50 (j) SDV 66.7, 50 (k) SDV 50, 37.5 (l) SDV 50, 33.3

(m) ODV 100, 75 (n) ODV 100,66.7 (o) ODV 75, 50 (p) ODV 66.7, 50 (q) ODV 50, 37.5 (r) ODV 50, 33.3

Figure 2.13: Volunteer 4. First row: single-VENC PC-MRI. Second row: SDV. Third row: ODV. Velocities are colored as in Figure 2.6. Numbers indicate the VENC(s).

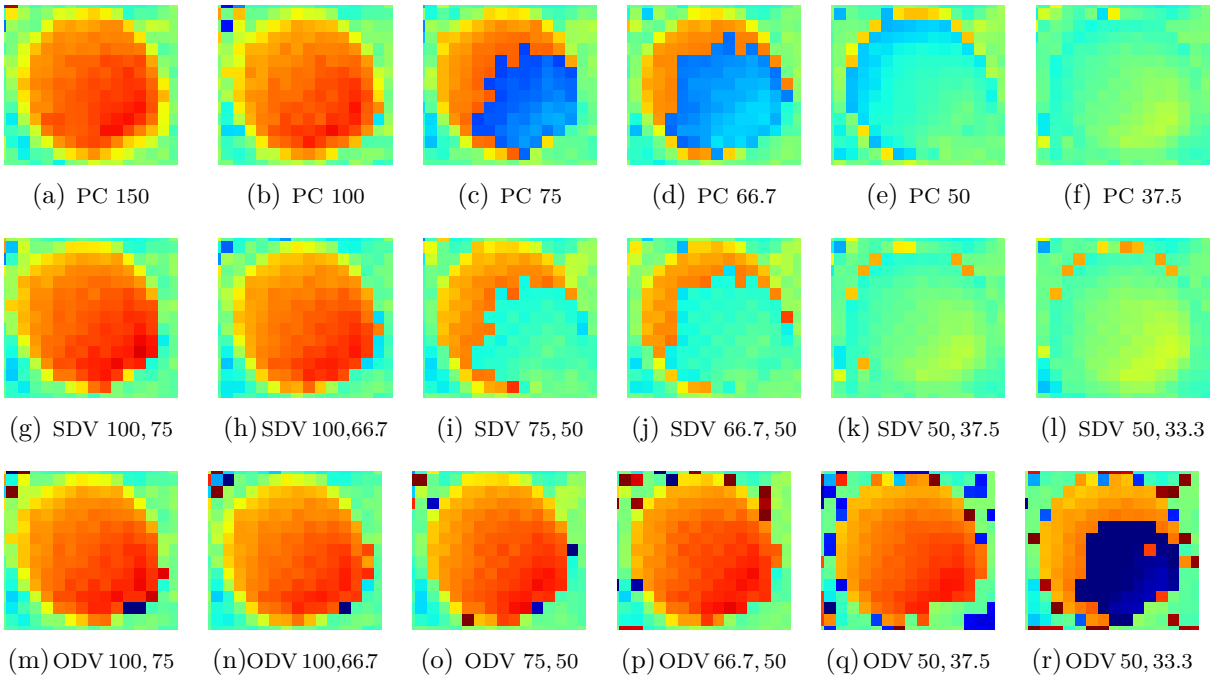

(a) PC 150 (b) PC 100 (c) PC 75 (d) PC 66.7 (e) PC 50 (f) PC 37.5

(g) SDV 100, 75 (h) SDV 100,66.7 (i) SDV 75, 50 (j) SDV 66.7, 50 (k) SDV 50, 37.5 (l) SDV 50, 33.3

(m) ODV 100, 75 (n) ODV 100,66.7 (o) ODV 75, 50 (p) ODV 66.7, 50 (q) ODV 50, 37.5 (r) ODV 50, 33.3

Figure 2.14: Volunteer 5. First row: single-VENC PC-MRI. Second row: SDV. Third row: ODV. Velocities are colored as in Figure 2.6. Numbers indicate the VENC(s).

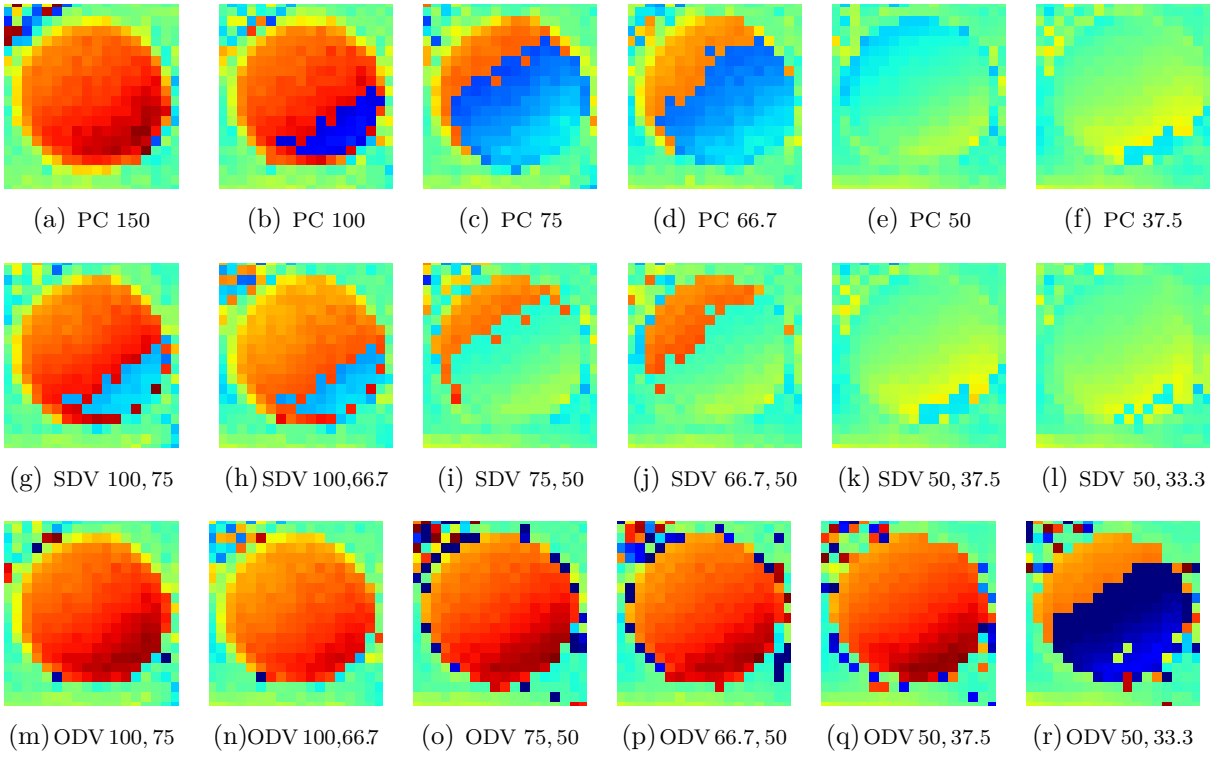

(a) PC 150 (b) PC 100 (c) PC 75 (d) PC 66.7 (e) PC 50 (f) PC 37.5

(g) SDV 100, 75 (h) SDV 100,66.7 (i) SDV 75, 50 (j) SDV 66.7, 50 (k) SDV 50, 37.5 (l) SDV 50, 33.3

(m) ODV 100, 75 (n) ODV 100,66.7 (o) ODV 75, 50 (p) ODV 66.7, 50 (q) ODV 50, 37.5 (r) ODV 50, 33.3

Figure 2.15: Volunteer 6. First row: single-VENC PC-MRI. Second row: SDV. Third row: ODV. Velocities are colored as in Figure 2.6. Numbers indicate the VENC(s).

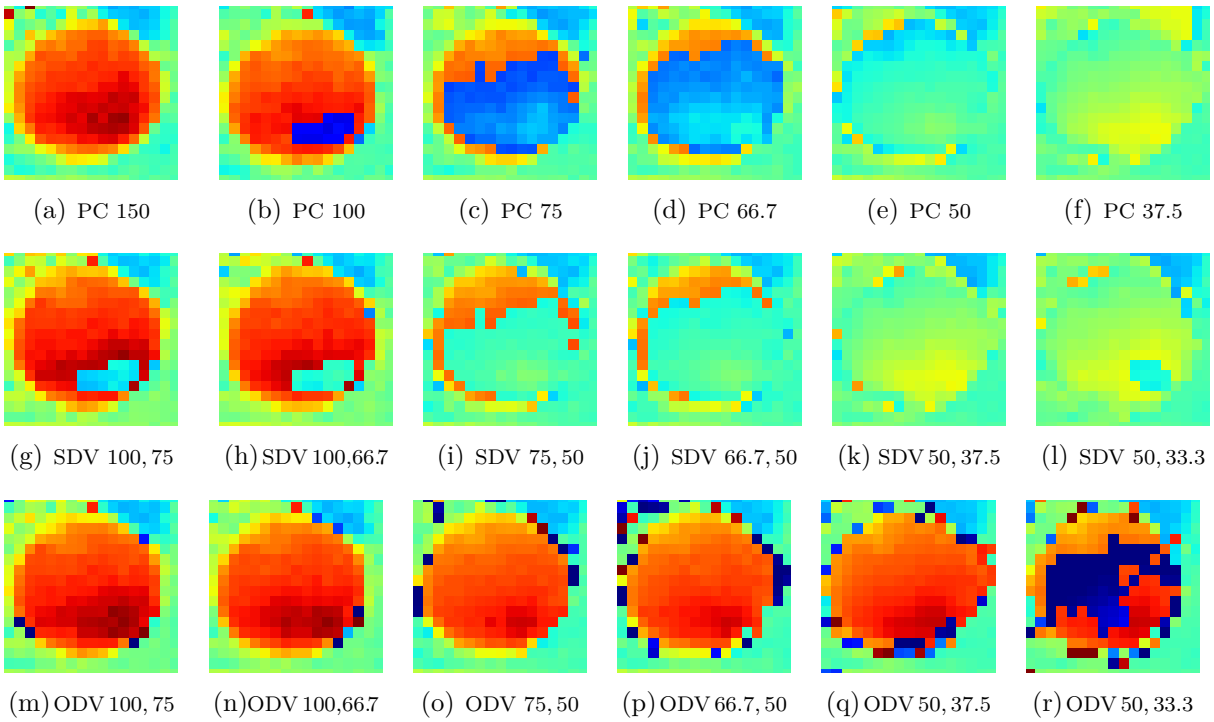

(a) PC 150 (b) PC 100 (c) PC 75 (d) PC 66.7 (e) PC 50 (f) PC 37.5

(g) SDV 100, 75 (h) SDV 100,66.7 (i) SDV 75, 50 (j) SDV 66.7, 50 (k) SDV 50, 37.5 (l) SDV 50, 33.3

(m) ODV 100, 75 (n) ODV 100,66.7 (o) ODV 75, 50 (p) ODV 66.7, 50 (q) ODV 50, 37.5 (r) ODV 50, 33.3

Figure 2.16: Volunteer 7. First row: single-VENC PC-MRI. Second row: SDV. Third row: ODV. Velocities are colored as in Figure 2.6. Numbers indicate the VENC(s).

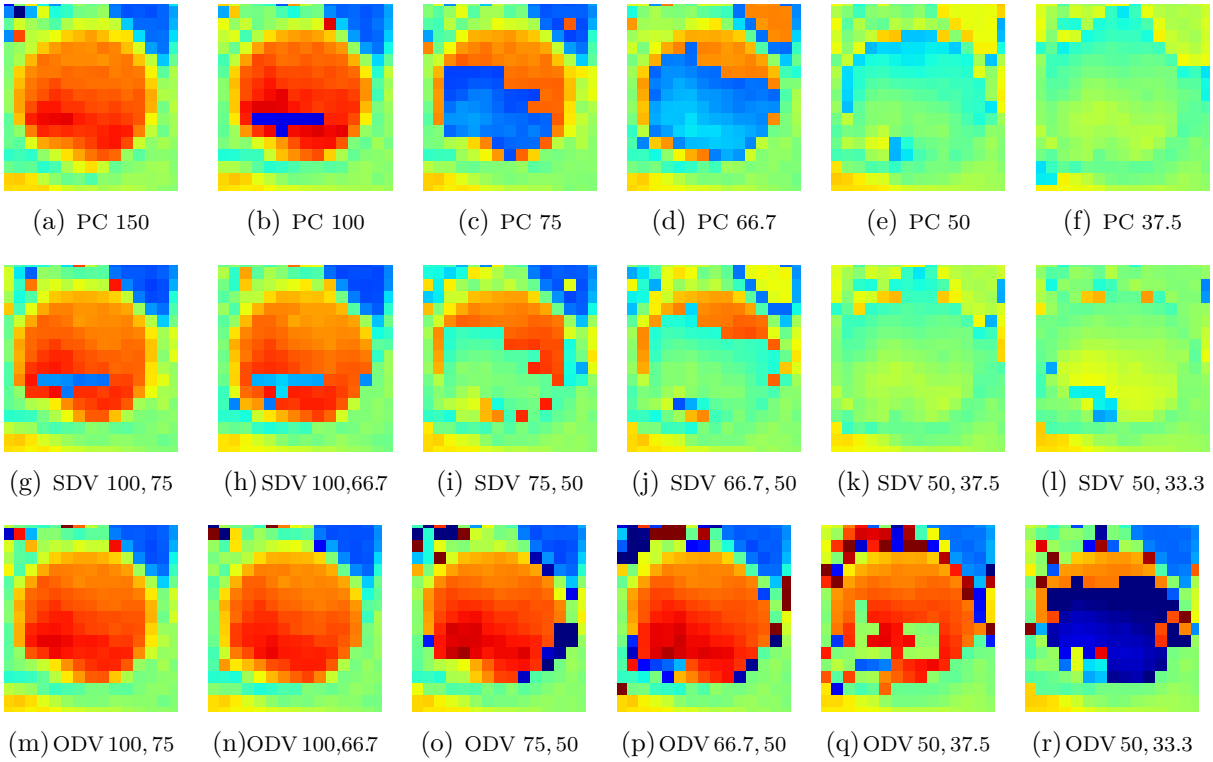

(a) PC 150 (b) PC 100 (c) PC 75 (d) PC 66.7 (e) PC 50 (f) PC 37.5

(g) SDV $100, 75$ (h) SDV $100,66.7$ (i) SDV $75, 50$ (j) SDV $66.7, 50$ (k) SDV $50, 37.5$ (l) SDV $50, 33.3$

(m) ODV $100, 75$ (n) ODV $100,66.7$ (o) ODV $75, 50$ (p) ODV $66.7, 50$ (q) ODV $50, 37.5$ (r) ODV $50, 33.3$

Figure 2.17: Volunteer 8. First row: single-VENC PC-MRI. Second row: SDV. Third row: ODV. Velocities are colored as in Figure 2.6. Numbers indicate the VENC(s).

Chapter 3

Dual-encoding for motion unwrapping in harmonic MRE

The experimental data of this work was provided by Helge Hertum and Ingolf Sack, Elastography Group, Charité University Hospital, Berlin, Germany. These results are the basis for an article currently in preparation in collaboration with Charité.

3.1 Introduction

In this chapter we briefly present an extension of the work shown in Chapter 2 in the case of magnetic resonance elastography, introduced in Chapter 1, section 1.3.3. Unwrapping in MRE has been treated in the literature, as in MRI for velocity encoding, by smoothing with respect to neighbor pixels or even the neighbor timesteps [Ito82; GP98; Fly97; Sac+09; SZ03; Bar+15; JSD15], but since our technique will not follow the same idea, we will not compare them. However, smoothing techniques can be used after applying the technique presented in this chapter.

3.2 Theory

3.2.1 Harmonic displacement encoding (Henc)

Similar to the VENC idea, we define the harmonic displacement encoding, *henc*, by

$$henc = \frac{\pi}{\xi(\omega, T)}$$

Then (1.14) can be re-written as follows:

$$\vartheta_n(\boldsymbol{x}) = \frac{\pi}{henc} u_n(\boldsymbol{x})$$

From this equation we note that $|henc|$ is the maximum possible displacement which is not aliased, because $|\vartheta_n(\boldsymbol{x})| < \pi$, which could be a problematic constraint in the application of phase contrast for recovering the displacement.

In the rest of this chapter, we emphasize the dependence of ϑ_n on henc explicitly by writing

$$\vartheta_n(\boldsymbol{x}; u_n, henc) = \frac{\pi}{henc} u_n(\boldsymbol{x}) \tag{3.1}$$

3.2.2 Cost Functionals

For each time τ_n with $n = 0, 1, \ldots, N-1$, we will now reformulate the phase-contrast problem like a least-squares estimator, as we did for the velocity encoding problem. We will denote the true displacement $\hat{u}_n$, and the phase measured for that displacement for a given *henc* as $\hat{\vartheta}_n(\boldsymbol{x}; \hat{u}_n, henc)$.

For a fixed $\boldsymbol{x}$, we consider the functionals

$$J_n(\boldsymbol{x}; u, henc) = \frac{1}{2}\left| e^{i\hat{\vartheta}_n(\boldsymbol{x}; \hat{u}_n, henc)} - e^{i\vartheta_n(\boldsymbol{x}; u, henc)} \right|^2 \tag{3.2}$$

which is, after some calculations, equal to

$$J_n(\boldsymbol{x}; u, henc) = 1 - \cos\left(\hat{\vartheta}_n(\boldsymbol{x}; \hat{u}_n, henc) - \vartheta_n(\boldsymbol{x}; u, henc)\right) \tag{3.3}$$

Observe that $\hat{\vartheta}_n(\boldsymbol{x}; \hat{u}_n, henc) = \hat{\varphi}_n(\boldsymbol{x}; \hat{u}_n, henc) - \hat{\varphi}_0(x)$, so we need to measure $\hat{\varphi}_n(\boldsymbol{x}; \hat{u}_n, henc)$ and $\hat{\varphi}_0(x)$ by:

- $\hat{\varphi}_n(\boldsymbol{x}; \hat{u}_n, henc)$ is acquired by considering the equations described in the previous section, applying the gradient corresponding to the respective henc.
- $\hat{\varphi}_0(\boldsymbol{x})$ is acquired once in the experiment. It is obtained when we *apply a null gradient*.

In addition, observe that equation (3.3) asserts that, the minimum of J_n is reached when $\hat{\varphi}_n = \varphi_n + 2\pi\ell,\ \ell \in \mathbb{Z}$. In terms of the displacement u, the periodicity of $J_n(\boldsymbol{x}; \cdot, henc)$ is $2henc$. Therefore, as in standard phase-contrast MRI, aliasing arises if $|henc|$ is less or equal to the true displacement.

3.2.3 Dual encoding strategy

To overcome aliasing, we apply the following dual encoding strategy:

- We define the sum of functionals J_n with hencs H_1 and H_2:

  $$J_{\Sigma,n}(\boldsymbol{x}; u, H_1, H_2) = J_n(\boldsymbol{x}; u, H_1) + J_n(\boldsymbol{x}; u, H_2) \tag{3.4}$$

  Note that for each n we perform three measurements: the corresponding to H_1, H_2 and the null gradient.

- For each n, we can estimate $u_n(x)$ by the *unwrapped displacement* $u_n^*(\boldsymbol{x}; H_1, H_2)$ by solving the problem

  $$u_n^*(\boldsymbol{x}; H_1, H_2) = \underset{u \in [-u_{max}, u_{max}]}{\arg\min} J_{\Sigma,n}(\boldsymbol{x}; u, H_1, H_2) \tag{3.5}$$

  where $u_{max} = \mathrm{lcm}(2henc_1, henc_2)/2$, as in Section 2.2.6.

- If we need to obtain a displacement in a steady-state and $\tau_n = \dfrac{2\pi n}{N}$, we apply the following discrete Fourier transform in time of $\{u_n^*\}_{n=0}^{N-1}$ in order to obtain u_c by equation (1.15)

The advantage of the dual henc strategy is that the minimum $v_n(x; H_1, H_2)$ of $J_{\Sigma,n}(x; \cdot, H_1, H_2)$ is reached uniquely in an interval of width $2lcm\{H_1, H_2\}$, where lcm is the (rational) least common multiple, and, moreover, $u_n^*(x; H_1, H_2)$ is a minimum for $J_n(x; \cdot, H_1)$ and $J_n(x; \cdot, H_2)$. Therefore, if we take a *good* pair (H_1, H_2), such that $2lcm\{H_1, H_2\}$ is maximized, we can obtain an estimation for v_n which is unique in a wide interval, even when both (H_1, H_2) are smaller than the true displacement $\hat{u}_n$. Aliasing will only happens when $lcm\{H_1, H_2\} \leq |\hat{u}_n|$

3.3 Methods

We consider a phantom consisting of a plastic box of approximately 10x10x10 centimeters filled with an heparin gel to emulate soft tissue.
The scan parameters are:

- $TR = 2000$ ms, $TE = 95$ ms.
- $N = 8$ timesteps τ_n to sample one wave period of time $T = 20$ ms.
- Mechanical and MEG frequency are the same: $f_{mech} = f_{grad} = 50$ Hz, and then $\omega = 2\pi f_{mech} = 314.159$ rad/s.
- The gradient has the form

$$G(t) = \begin{cases} A & \text{if } t \in [0, T/2] \\ -A & \text{if } t \in [-T/2, 0[\\ 0 & \text{otherwise} \end{cases}$$

  with MEG amplitudes $A = \{2, 8, 9, 12, 16, 18\}$ [mT/m].

According to section 1.3.3, the encoding efficiency is

$$\xi(\omega, T) = -\gamma \int_{-T/2}^{T/2} G(t) \sin(\omega t) dt = -\frac{4\gamma A}{\omega} \tag{3.6}$$

where we used the fact that $T = \frac{2\pi}{\omega}$. Hence we see that in practice, for fixed ω, the encoding efficiency is controlled by the parameter A. Note that since aliasing occurs if $|henc(A)| < |u|$, aliasing occurs in this case if

$$|henc(A)| = \left| \frac{\pi}{\xi(\omega, T)} \right| = \frac{\pi\omega}{4\gamma A} < |u_{true}| \tag{3.7}$$

In the following table we show *henc* as a function of the amplitude for the amplitudes used in our experiment:

The following table shows the critical displacement for the dual encoding technique, following Table 2.1:

$A\ [10^{-3}mT/m]$	2	8	9	12	16	18	24
$\lvert henc(A)\rvert\ [10^{-4}m]$	4.612	1.153	1.025	0.769	0.576	0.512	0.384

Table 3.1: Correspondence between amplitude (A) and the henc, which can be seen as the critical observed displacement.

(A_1, A_2)	(9, 12)	(8, 12)	(12, 16)	(12, 18)	(16, 24)	(18, 24)
$\lvert henc_{eff}\rvert\ [10^{-4}m]$	3.074	2.306	2.306	1.537	1.153	1.537

Table 3.2: Correspondence between the pair (A_1, A_2) of amplitudes and the effective henc, that is, the critical displacement for the dual-henc technique.

3.4 Results

3.4.1 Results for a fixed time

We show the results for the phantom experiments for $n = 3, 5, 7$ in Figures 3.1, 3.2 and 3.3, respectively. The peak displacement is different at each time, which can be seen in the single-henc figure corresponding to $A = 2$. We can distinguish the shape of the phantom by separating it from the noisy part near the boundaries of each image. We first show the single-henc phase contrast MRI and the dual-henc technique, where we observe the aliasing in pixels corresponding to displacements according to Tables 3.1 and 3.2, respectively. That is,

- For single-henc, we observe aliasing from $A = 8$ onwards for $n = 3, 5$ and $A = 12$ for $n = 7$. It is also clear how the noise in the image decreases when increasing the encoding gradient.

- For dual-henc, we observe aliasing only for the pair $(12, 18)$ onwards for $n = 3, 5$ and we do not observe aliasing in any image for $n = 7$, because the critical value shown in Table 3.2 is not reached.

In addition, by observing the images for the different times, we can see the propagation of the displacement.

3.4.2 Results for the discrete Fourier transform in time

We perform a discrete Fourier transform in time and show the results for the phantom experiments in Figure 3.4. The peak displacement can be seen in the single-henc figure corresponding to $A = 2$, and we see that it is bigger than the peak of each time. The transition to aliased images is not inferred directly from Tables 3.1 and 3.2, but we can notice that if one of the recovered displacements has aliasing for any time, then the Fourier transform in time has aliasing, that is:

- For single-henc, we observe aliasing from $A = 8$ onwards, because aliasing is present for that amplitude and some n, specifically, at least for $n = 3, 5$.

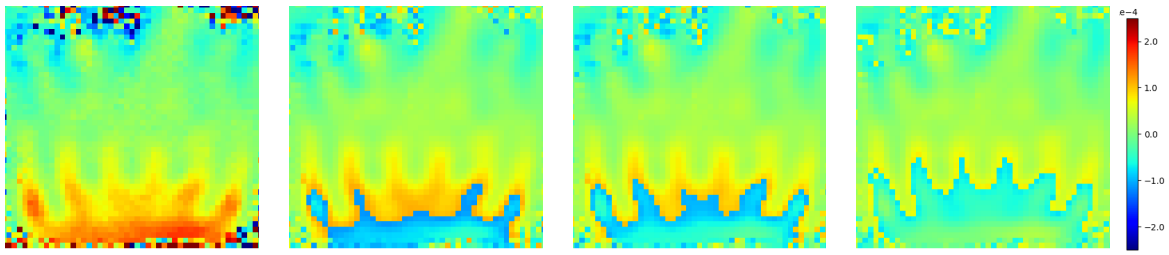

(a) PC $A = 2$ (b) PC $A = 8$ (c) PC $A = 9$ (d) PC $A = 12$

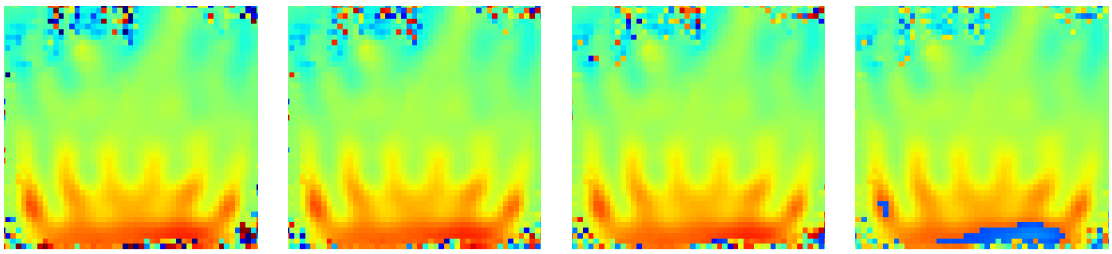

(e) ODV $9, 12$ (f) ODV $8, 12$ (g) ODV $12, 16$ (h) ODV $12, 18$

Figure 3.1: Phantom data: single- (PC) and dual-HENC, for $n = 3$

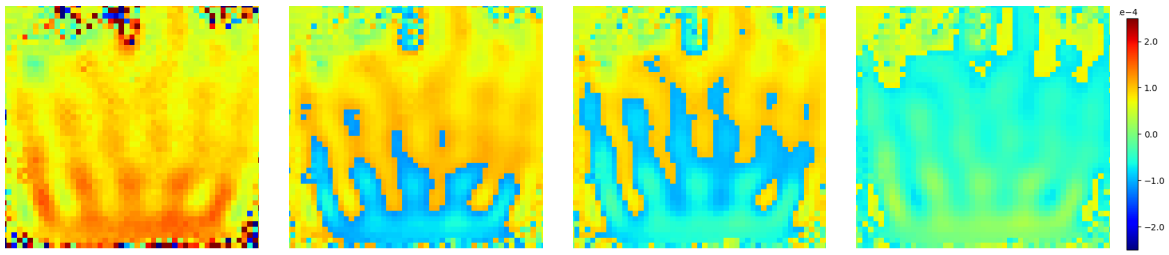

(a) PC $A = 2$ (b) PC $A = 8$ (c) PC $A = 9$ (d) PC $A = 12$

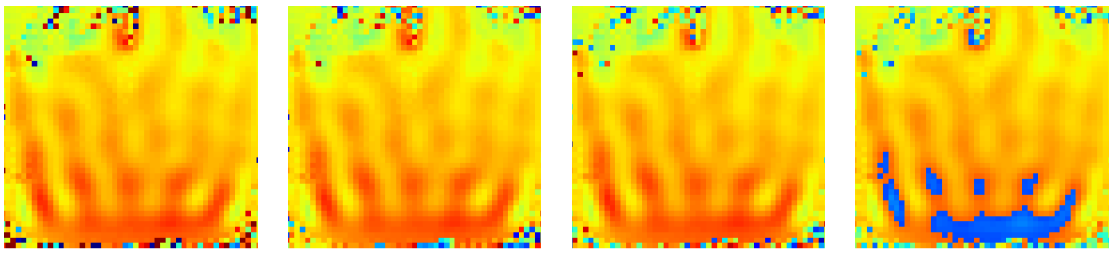

(e) ODV $9, 12$ (f) ODV $8, 12$ (g) ODV $12, 16$ (h) ODV $12, 18$

Figure 3.2: Phantom data: single- (PC) and dual-HENC, for the time corresponding to $n = 5$.

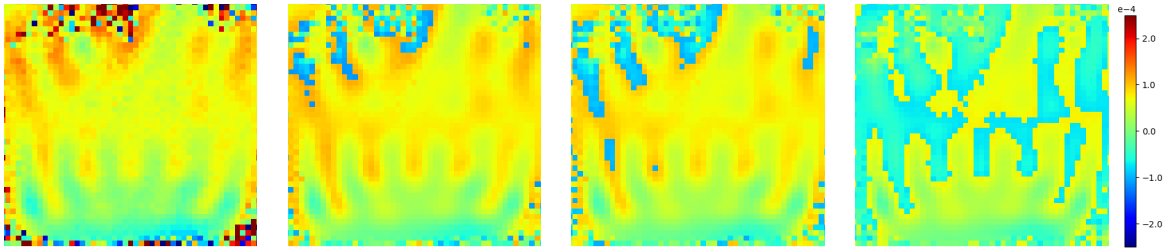

(a) PC $A = 2$ (b) PC $A = 8$ (c) PC $A = 9$ (d) PC $A = 12$

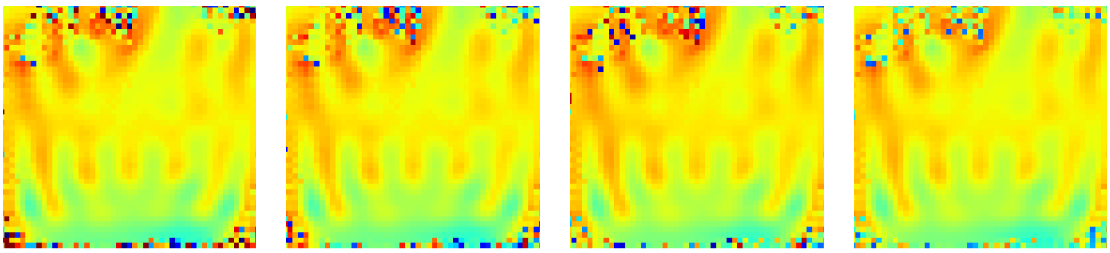

(e) ODV $9, 12$ (f) ODV $8, 12$ (g) ODV $12, 16$ (h) ODV $12, 18$

Figure 3.3: Phantom data: single- (PC) and dual-HENC, for the time corresponding $n = 7$.

- For dual-henc, we observe aliasing in $(A_1, A_2) = (12, 18)$ since aliasing is present for that amplitude pair and at least $n = 3, 5$.

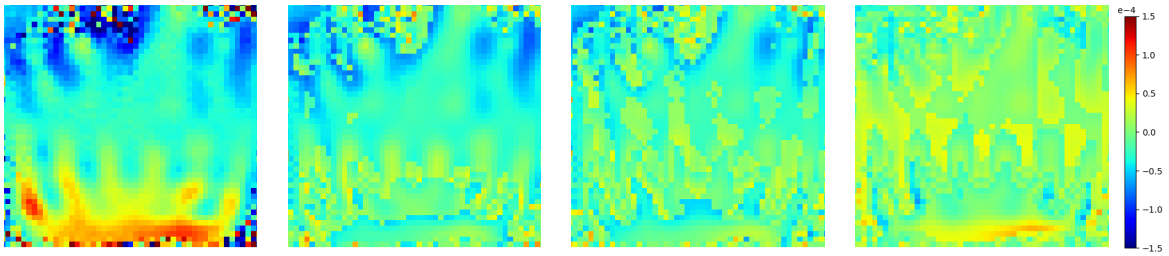

(a) PC $A = 2$ (b) PC $A = 8$ (c) PC $A = 9$ (d) PC $A = 12$

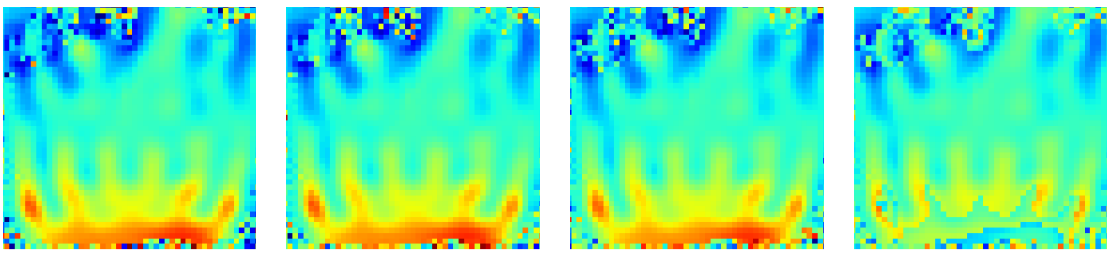

(e) ODV $9, 12$ (f) ODV $8, 12$ (g) ODV $12, 16$ (h) ODV $12, 18$

Figure 3.4: Phantom data: single- (PC) and dual-HENC, for $\mathrm{Re}(u_c)$ obtained from the discrete Fourier transform in time.

3.5 Discussions and conclusions

We see that the theory is confirmed at least in a phantom experiment, showing properly the predictions given. At this moment, we haven't performed any experiment with volunteers. The dual-henc MRE technique presented has a potential advantage: we can reconstruct very small displacements, which usually correspond to points distant to the mechanical source, with less noise and at the same time we can reconstruct larger displacements, corresponding to points close to the mechanical source, without aliasing.

Here we aim to keep henc constant. Equation (3.7) has as a consequence that, if the frequency is halved, the amplitude must be doubled. This does not cause serious problems in actual implementations.

However, if the frequency is halved, i.e., if the period is doubled, the corresponding repetition time and echo times become much larger than those used for velocity recovering in MRI. This could cause practical problems that are not solved by the dual-henc technique, since they are related with the relaxation times showed in equation (1.1). Therefore it is still a challenge to explore deeper in tissues by reducing the frequency.

Chapter 4

Nonlinear hybrid inverse problems in elasticity

The content of this chapter corresponds to the article H. Carrillo and A. Waters. "Nonlinear hybrid inverse problems in elasticity". In preparation.

4.1 Introduction

We consider an isotropic nonlinear elastic wave equation in a bounded domain Ω. The stress the material is under going is described by the Lamé parameters, λ, μ, and ρ. We study the following problem: is it possible to determine the Lamé parameters λ, μ and ρ from the knowledge of Neumann data of the solution on the boundary? We are interested in the global recovery problem of the displacement field.

Our main motivation is the structure of hyper-elastic materials, many of which are not accurately described by linear elastic models. A hyperelastic model is one for an ideally elastic material in which the stress-strain relationship is derived from the strain energy density function. This type of model is often known as Green's model which was made rigorous by Ogden [Ogd97]. Hyper-elastic models accurately describe the stress-strain behaviour of materials such as rubber, [Muh05]. Unfilled vulcanized elastomers almost always conform to the hyperelastic ideal. Filled elastomers and biological tissues are also modelled via the hyper-elastic idealisation, [Gao+14]. In the linear case, for reconstruction of the Lamé coefficients concerning biological tissues, one can see [Amm08] for example. Our focus is on a non-linear model, and the reduction of the amount of required data to recover the coefficients uniquely. Of the three parameters required to recover the material structure, it is often the most natural to recover the parameter μ which encodes more about possible disease in patients than the other parameters. Several diseases involve changes in the mechanical properties of tissue and normal function of tissue, for example in skeletal muscle, heart, lungs and gut [**mclaughlin2010calculating**; HSB17; GME12].

From power density measurements we are able to to prove a stability estimate for both the solution and the parameter μ. Even in the linear case for elasticity this has not been shown before in the literature. For the linear problem, the closest works in 2 and 3 dimensions are for the anisotropic conductivity problem [Bal+14] and for full solution measurements in [BMU15; AWZ15; WS15]. However, this list is not exhaustive there are numerous results on recovering the parameters μ and λ from knowledge of the solution in a domain for the

linear problem [Bal+11; SKS12; NTT11; KS12; KK08]. As such, the significant contribution of this article is the extension to the nonlinear problem. The difficult symbol computations used to find stability estimates for the nonlinear problem can also be used to extend known results on the linear problem.

In Section 4.4, we give precise stability estimates for the linearized incompressible model of elasticity in 2 dimensions with the background pressure held fixed, see Theorem 4.5. These stability estimates have no kernel (they are injective) for all ω sufficiently large on the entirety of the domain with two measurements. In Section 4.5, we can extend these estimates to include some generic nonlinear forcing terms. This is the first time global injectivity with a single fixed ω has been shown under any conditions.

For the later part of the article, in Section 4.7, we consider the Saint-Venant model of elasticity. Because the (nonlinear) Saint-Venant model depends on the parameter λ and this in practice is large, we also prove convergence of the linearized Saint Venant model in 2 and 3 dimensions using a differential operator (the curl) which removes the parameter λ. In the process of doing so, in Section 4.6, we correct an earlier computational error in the stability estimates for the linearized compressible problem in two dimensions in [AWZ15] which affects the 2d stability estimates. The size of the parameter λ aversely affects the size of the class of solutions which can be considered in the linearized Saint-Venant model, unless we apply the curl. This means our convergence results are sharper than in [Hub+18]. Indeed, the main assumption on their nonlinear models does not give any convergence result for the Saint-Venant model when λ is very large. We use solution measurements in the linearized Saint-Venant model, since power density measurements do not work well when using the annihilation (curl) operator.

Iterative algorithms for the recovery of μ and convergence results are presented for each model in Sections 4.4.5, 4.5.3 and 4.7.3. Main tools in this article come from the theory of over-determined elliptic boundary-value problems. In Section 4.3 we present necessary preliminaries.

4.2 Notation

In this paper we use the Einstein summation convention. For two vectors a and b, the exterior product is denoted by

$$a \otimes b = ab^{\intercal},$$

i.e., $a \otimes b$ is a matrix with entries

$$(a \otimes b)_{ij} = a_i b_j.$$

More generally, the exterior product between a tensor A of order m and B of order n is a new tensor $A \otimes B$ of order $m + n$ with entries

$$(A \otimes B)_{i_1 \dots i_m j_1 \dots j_n} = A_{i_1 \dots i_m} B_{j_1 \dots j_n}.$$

For two matrices A and B of the same size, the inner product is denoted by

$$A : B = a_{ij} b_{ji},$$

and we write $|A|^2 = A : A$. In addition, we consider the product between a tensor A of order $(n + 1)$ and other B of order n as the vector AB with entries

$$(AB)_{i_0} = A_{i_0 i_1 \dots i_n} B_{i_1 \dots i_n}.$$

Let $\Omega \subset \mathbb{R}^d$ be a simply-connected smooth bounded domain in $\mathbb{R}^d$. For vector–valued functions

$$f(x) = (f_1(x), f_2(x), \dots, f_d(x)) : \Omega \to \mathbb{R}^d \ ,$$

the Hilbert space $H_m(\Omega)^d$, $m \in \mathbb{N}$ is defined as the completion of the space $\mathcal{C}_c^\infty(\Omega)^d$ with respect to the norm

$$\|f\|_m^2 = \|f\|_{m,\Omega}^2 = \sum_{|i|=1}^{m} \int_\Omega |\nabla^i f(x)|^2 + |f(x)|^2 \, dx,$$

where we write $\nabla^i = \partial^{i_1} \dots \partial^{i_d}$ for $i = (i_1, \dots, i_d)$ for the higher-order derivative. Let E be the symmetric gradient acting on $u \in H_0^1(\Omega)^d$ as

$$Eu = \frac{1}{2}(\nabla u + (\nabla u)^\intercal) = \nabla^S u. \tag{4.1}$$

In general, we assume the Lamé coefficients are $C^3(\overline{\Omega})$ where $\overline{\Omega}$ denotes the closure of Ω and that they satisfy the following conditions

$$\begin{aligned} \lambda(x) &\geq \lambda_{\min} = \min\{\lambda(x) : x \in \overline{\Omega}\} > 0, \\ \mu(x) &\geq \mu_{\min} = \min\{\mu(x) : x \in \overline{\Omega}\} > 0, \\ \rho(x) &\geq \rho_{\min} = \min\{\rho(x) : x \in \overline{\Omega}\} > 0. \end{aligned} \tag{4.2}$$

We consider the density $\rho(x)$ to be fixed for this article, and as such we remove it from the symbol computations. We remind the definition of the divergence for a matrix function: if $T : \bar{\Omega} \to \mathbb{M}^n$ (square matrices of order n) is differentiable, then

$$\operatorname{div}(T)(x) = \partial_j T_{ij}(x) \hat{e}_i \ \in \mathbb{R}^d.$$

Also we remind the definition of the curl of a function $f : \Omega \to \mathbb{R}^d$:

$$\nabla \times f = \partial_1 f_2 - \partial_2 f_1$$

in dimension $d = 2$, and

$$\nabla \times f = (\partial_2 f_3 - \partial_3 f_2)\boldsymbol{e}_1 - (\partial_1 f_3 - \partial_3 f_1)\boldsymbol{e}_2 + (\partial_1 f_2 - \partial_2 f_1)\boldsymbol{e}_3$$

in dimension $d = 3$.
And finally we remind the reader of a useful integration by parts identity. If $S : \bar{\Omega} \to \mathbb{S}^d$ (symmetric matrices) and $v : \bar{\Omega} \to \mathbb{R}^d$, then

$$\int_\Omega \operatorname{div}(S) \cdot v \ dx = \int_{\partial\Omega} (S\nu) \cdot v \ da - \int_\Omega S : \nabla^S v \ dx,$$

where ν denotes the outward unit normal on $\partial\Omega$.

We will also need the following lemma.

Lemma 4.1. *[Korn's inequality] Let Ω be as above. Let $u \in H_0^1(\Omega)^d$ then*

$$\int_\Omega |\nabla u|^2 \, dx \leq 2 \int_\Omega |\nabla^S u|^2 \, dx,$$

c.f., for instance, [Amm+15].

We now review the existence and uniqueness results for the elasticity system. We consider the following boundary value problem for the elasticity equations

$$\begin{cases} \nabla(\lambda(x)\nabla\cdot u_\lambda) + \omega^2 u_\lambda(x) + 2\nabla\cdot\mu(x)\nabla^S u_\lambda(x) = 0 \quad \text{in } \Omega, \\ \\ u_\lambda(x) = g(x) \quad \text{on} \quad \partial\Omega, \end{cases} \tag{4.3}$$

with $\mu(x), \lambda(x) \in \mathcal{C}^1(\bar{\Omega})$ the Lamé coefficients.

The solution $u_\lambda(x)$ is such that

$$u_\lambda(x) : \Omega \to \mathbb{R}^d.$$

It is known that the solution $u_\lambda(x)$ exists and is unique. In particular, $\nabla^S u_\lambda(x) \in L^2(\Omega)^d$ if $g(x) \in H^{1/2}(\partial\Omega)$, $\lambda, \mu \in L^\infty(\Omega)$ and satisfy (4.2) and $\nabla^S u_\lambda(x) \in H^4(\Omega)^d$ under the additional assumptions that $\mu(x), \lambda(x) \in \mathcal{C}^4(\bar{\Omega})$, $g \in H^{9/2}(\partial\Omega)^d$. We need the latter regularity assumption for later stability estimates.

The Poisson ratio σ of the anomaly is given in terms of the Lamé coefficients by

$$\sigma = \frac{\lambda/\mu}{1 + 2\lambda/\mu}.$$

It is known in soft tissues $\sigma \approx 1/2$ or equivalently $\lambda >> \mu$. This makes it difficult to reconstruct both parameters μ and λ simultaneously [Man+01],[GFI03]. Therefore we first construct asymptotic solutions to the problem (4.3) when $\lambda_{\min} \to \infty$. The following theorem loosely follows [Amm+08] and [Amm+13] which consider piecewise constant Lamé coefficients. We recall that in the limit, the elasticity equations (4.3) reduces to the following Stokes system

$$\begin{cases} \omega^2 u(x) + 2\nabla\cdot\mu(x)\nabla^S u(x) + \nabla p(x) = 0 \quad \text{in } \Omega, \\ \\ \nabla\cdot u(x) = 0 \quad \text{in} \quad \Omega, \\ \\ u(x) = g(x) \quad \text{on} \quad \partial\Omega, \\ \\ \int\limits_\Omega p(x)\,dx = 0. \end{cases} \tag{4.4}$$

Theorem 4.1 ([AWZ15] '14)**.** *Suppose that ω^2 is not an eigenvalue of the problem (4.4) with $g(x) = 0$, then there exists a positive constant C which is independent of λ such that the following error estimates hold for λ_{min} large enough*

$$||u_\lambda - u||_{H^1(\Omega)^d} \leq \frac{C}{\sqrt{\lambda_{min}}}. \tag{4.5}$$

Remark 1. *The relation between the pressure p in* (4.4) *and u_λ in* (4.3) *is that p is the limit of $\lambda\nabla\cdot u_\lambda$ as $\lambda_{min} \to \infty$.*

4.3 Preliminaries on Over-determined Elliptic Boundary-Value Problems

In this section, we present some basic properties about over-determined elliptic boundary-value problems which plays a key role in our stability estimates in the next sections. The presentation follows closely to the ones in [Sol73; WS15]. We present it here for the convenience of the reader.

We first recall the definition of ellipticity in the sense of Douglis-Nirenberg. Consider the (possibly) redundant system of linear partial differential equations

$$\begin{aligned} \mathcal{L}(x, \frac{\partial}{\partial x})y &= \mathcal{S}, \\ \mathcal{B}(x, \frac{\partial}{\partial x})y &= \phi, \end{aligned} \tag{4.6}$$

for m unknown functions $y = (y_1, \dots, y_m)$ comprising in total of M equations. Here $\mathcal{L}(x, \frac{\partial}{\partial x})$ is a matrix differential operator of dimension $M \times m$ with entries $L_{ij}(x, \frac{\partial}{\partial x})$. For each $1 \le i \le M$, $1 \le j \le m$ and for each point x, the entry $L_{ij}(x, \frac{\partial}{\partial x})$ is a polynomial in $\frac{\partial}{\partial x_i}$ $i = 1, \dots, d$. If the system is redundant, then there are possibly more equations than unknowns, $M \ge m$. The matrix $\mathcal{B}(x, \frac{\partial}{\partial x})$ has entries $B_{ij}(x, \frac{\partial}{\partial x})$ for $1 \le k \le Q, 1 \le j \le m$ consisting of Q equations at the boundary. The operators are also polynomial in the partials of x. Naturally, the vector $\mathcal{S}$ is a vector of length M, and ϕ is a vector of length Q.

Definition 4.1. *[c.f.[ADN59],[DN55]] Let integers $s_i, t_j \in \mathbb{Z}$ be given for each row $1 \le i \le M$ and column $1 \le j \le m$ with the following property: for $s_i + t_j \ge 0$ the order of L_{ij} does not exceed $s_i + t_j$. For $s_i + t_j < 0$, one has $L_{ij} = 0$. Furthermore, the numbers are normalized so that for all i one has $s_i \le 0$. The numbers s_i, t_j are known as Douglis-Nirenberg numbers.*

The principal part of $\mathcal{L}$ for this choice of numbers s_i, t_j is defined as the matrix operator $\mathcal{L}^0$ whose entries are composed of those terms in L_{ij} which are exactly of order $s_i + t_j$.

The principal part $\mathcal{B}^0$ of $\mathcal{B}$ is composed of the entries which are composed of those terms in B_{kj} which are exactly of order $\sigma_k + t_j$. The numbers σ_k, $1 \le k \le Q$ are computed as

$$\sigma_k = \max_{1 \le j \le m} (b_{kj} - t_j)$$

with b_{kj} denoting the order of B_{kj}. Real directions with $\xi \ne 0$ and

$$\operatorname{rank} \mathcal{L}^0(x, i\xi) < m$$

are called characteristic directions of $\mathcal{L}$ at x. The operator $\mathcal{L}$ is said to be (possibly) over-determined elliptic in Ω if $\forall x \in \overline{\Omega}$ and for all real nonzero vectors ξ one has

$$\operatorname{rank} \mathcal{L}^0(x, i\xi) = m.$$

We next recall the following Lopatinskii boundary condition.

Definition 4.2. *Fix $x \in \partial\Omega$ and let ν be the inward unit normal vector at x. Let ζ be any non-zero tangential vector to Ω at x. We consider the line $\{x + z\nu, z > 0\}$ in the upper half plane and the following system of ODE's*

$$\mathcal{L}^0(x, i\zeta + \nu \frac{d}{dz})\tilde{y}(z) = 0 \qquad z > 0, \tag{4.7}$$

$$\mathcal{B}^0(x, i\zeta + \nu \frac{d}{dz})\tilde{y}(z) = 0 \qquad z = 0. \tag{4.8}$$

We define the vector space V of all solutions to the system (4.7)-(4.8) which are such that $\tilde{y}(z) \to 0$ as $z \to \infty$. If $V = \{0\}$, then we say that the Lopatinskii condition is fulfilled for the pair $(\mathcal{L}, \mathcal{B})$ at x.

Now, let $\mathcal{A}$ be the operator defined by

$$\mathcal{A} = (\mathcal{L}, \mathcal{B}).$$

Then the equations (4.6) read as $\mathcal{A}y = (\mathcal{S}, \phi)$.

Let $\mathcal{A}$ act on the space

$$D(p,l) = W_p^{l+t_1}(\Omega) \times \ldots \times W_p^{l+t_m}(\Omega)$$

with $l \geq 0$, $p > 1$. Here W_p^α denotes the standard Sobolev space with α's order partial derivatives in the L^p space. With some regularity assumptions on the coefficients of $\mathcal{L}$ and $\mathcal{B}$, $\mathcal{A}$ is bounded with range in the space

$$R(p,l) = W_p^{l-s_1}(\Omega) \times \ldots \times W_p^{l-s_m}(\Omega) \times W_p^{l-\sigma_1-\frac{1}{p}} \times \ldots \times W_p^{l-\sigma_q-\frac{1}{p}}(\partial\Omega).$$

We have the following result, see [WS15, Theorem 1].

Theorem 4.2. *Let the integers $l \geq 0, p > 1$ be given. Let $(\mathcal{S}, \phi) \in \mathcal{R}(p,l)$. Let the Douglis-Nirenberg numbers s_i and t_j be given for $\mathcal{L}$ and σ_k be as in Definition 4.1. Let Ω be a bounded domain with boundary in $\mathcal{C}^{l+\max t_j}$. Also assume that $p(l-s_i) > d$ and $p(l-\sigma_k) > d$ for all i and k. Let the coefficients L_{ij} be in $W_p^{l-s_i}(\Omega)$ and the coefficients of B_{kj} be in $W^{l-\sigma_k-\frac{1}{p}}$. The following statements are equivalent:*

1. *$\mathcal{L}$ is over-determined elliptic and the Lopatinskii condition is fulfilled for $(\mathcal{L}, \mathcal{B})$ on $\partial\Omega$.*
2. *There exists a left regularizer $\mathcal{R}$ for the operator $\mathcal{A} = \mathcal{L} \times \mathcal{B}$ such that*

$$\mathcal{R}\mathcal{A} = \mathcal{I} - \mathcal{T}$$

with $\mathcal{T}$ compact from $R(p,l)$ to $D(p,l)$.

3. *The following a priori estimate holds*

$$\sum_{j=1}^{m} ||y_j||_{W_p^{l+t_j}(\Omega)} \leq C_1 \left(\sum_{i=1}^{M} ||\mathcal{S}_i||_{W_p^{l-s_i}(\Omega)} + \sum_{k=1}^{Q} ||\phi_k||_{W_p^{l-\sigma_j-\frac{1}{p}}(\partial\Omega)} \right) + C_2 \sum_{t_j>0} ||y_j||_{L^p(\Omega)},$$

where y_j is the j-th component of the solution y.

4.4 Linear elasticity with elastic energy density measurements

Given Theorem 4.1 for the system (4.4), we chose to consider the system

$$\begin{cases} \omega^2 u_j + 2\nabla \cdot \mu \nabla^S u_j = -\nabla p_j & \text{in } \Omega, \\ \nabla \cdot u_j = 0 & \text{in } \Omega, \\ u_j = g_j & \text{on } \partial\Omega, \end{cases} \tag{4.9}$$

for $j = 1, \dots, J$. We add the power density measurements:

$$\frac{\mu}{2}|\nabla^S u_j|^2 = H_j \quad \text{in } \Omega, \tag{4.10}$$

for $j = 1, \dots, J$. Power density measurements are essentially a measure of the local energy of the solution, as a result of the Lebesgue differentiation theorem. An example of imaging technique that measures power densities, but under an similar scalar model, is ultrasound modulated electrical impedance tomography (UMEIT) [Bal+11].

Let $v = (\mu, \{u_j\}_{j=1}^J)$. Then the system (4.9)-(4.10) may be recast as

$$\begin{cases} \mathcal{F}v &= \mathcal{H} \quad \text{in } \Omega, \\ \mathcal{B}v &= g \quad \text{on } \partial\Omega. \end{cases} \tag{4.11}$$

where $\mathcal{F}$ and $\mathcal{B}$ are the differential operators defining the system (4.9)-(4.10). We know that the underlying unperturbed equations are well posed, and the main result of section 4.4.5 will be to provide an existence and uniqueness result for the linearisation of this equation (4.11). We consider the background pressure ∇p to be fixed. The stability estimates given here then would allow us to go back and solve for p as soon as u and μ are known, since by applying divergence we can determine Δp and then obtain an elliptic equation in p. We do not perform this calculation here, but it is the motivation behind our choice of model in this section.

4.4.1 Ellipticity arguments in dimension 2

In dimension $d = 2$, notice that $\xi \in \mathbb{R}^2$ can be written as

$$\xi = |\xi| \begin{pmatrix} \cos(\theta) \\ \sin(\theta) \end{pmatrix}$$

for some $\theta \in]-\pi, \pi]$. Moreover, the symmetric gradient of a incompressible vector valued function u satisfies

$$\nabla^S u = (\nabla^S u)^\intercal, \quad \operatorname{tr}(\nabla^S u) = 0,$$

then $\nabla^S u$ can be written as

$$\nabla^S u(x) = \frac{|\nabla^S u(x)|}{\sqrt{2}} \begin{bmatrix} \cos(\alpha(x)) & \sin(\alpha(x)) \\ \sin(\alpha(x)) & -\cos(\alpha(x)) \end{bmatrix}$$

for some $\alpha(x) \in]-\pi, \pi]$. We will use these structures along the section. We also use the following notation where F is a vector or a matrix:

$$\hat{F} = \frac{F}{|F|}.$$

One measurement, lack of invertibility

We consider the case of dimension $d = 2$ only in this section. Consider the case $J = 1$, that is, only one measurement. Let us define $F_j = \nabla^S u_j$ and assume that $|F_j| > 0$ for all $x \in \Omega$. From equation (4.10) we obtain

$$\mu = \frac{2H_j}{|F_j|^2} \tag{4.12}$$

and then we can replace μ in equation (4.9) to obtain:

Lemma 4.2.

$$\frac{\omega^2|F_j|^2}{2H_j}u_j + \nabla^S u_j \nabla \ln(H_j) + (\mathbb{I} - 2\hat{F}_j \otimes \hat{F}_j)\nabla \otimes \nabla^S u_j = -\frac{|F_j|^2}{2H_j}\nabla p_j \tag{4.13}$$

where $\mathbb{I}$ is a fourth order tensor whose entries are defined as

$$\mathbb{I}_{ijkl} = \delta_{ik}\delta_{jl} + \delta_{jk}\delta_{il}.$$

Proof. We have (dropping the sub-index j):

$$2\nabla \cdot \mu \nabla^S u + \omega^2 u + \nabla p = 0$$

where μ is given by (4.12). We analyze the first term in the left side of the equation, considering additionally that $\nabla \cdot u = 0$:

$$2\nabla \cdot \mu \nabla^S u = 2\mu\Delta u + 2\nabla^S u \nabla \mu = \frac{4H}{|F|^2}\Delta u - 4\nabla^S u \nabla\Big(\frac{H}{|F|^2}\Big).$$

Then we compute $\nabla\Big(\frac{H}{|F|^2}\Big)$:

$$\nabla\Big(\frac{H}{|F|^2}\Big) = \frac{1}{|F|^4}\Big(|F|^2\nabla H - H\nabla|F|^2\Big)$$

where:

$$\nabla|F|^2 = \frac{\partial|F|^2}{\partial x_k}\hat{e}_k = 2F_{ij}\frac{\partial F_{ij}}{\partial x_k}\hat{e}_k = 2(\nabla \otimes F)F.$$

Therefore

$$2\nabla \cdot \mu \nabla^S u = \frac{2H}{|F|^2}\Delta u + \frac{2}{|F|^2}\nabla H - \frac{4H}{|F|^4}(\nabla \otimes F)F$$

and then

$$\frac{2H}{|F|^2}\Delta u + \frac{2}{|F|^2}\nabla^S u \nabla H - \frac{4H\nabla^S u}{|F|^4}(\nabla \otimes F)F + \omega^2 u + \nabla p = 0.$$

Multipyling both sides of the equation by $\frac{|F|^2}{2H}$ we obtain:

$$\Delta u + \nabla^S u \nabla \ln(H) - 2\hat{F}(\nabla \otimes F)\hat{F} + \omega^2\frac{|F|^2}{2H}u + \frac{|F|^2}{2H}\nabla p = 0$$

Finally, we notice that

$$\Delta u - 2\hat{F}(\nabla \otimes F)\hat{F} = (\mathbb{I} - 2\hat{F} \otimes \hat{F})\nabla \otimes \nabla^S u.$$

□

Now, identifying the leading term of (4.13), we define the operator:

$$P_j(x, D) = \Big(\mathbb{I} - 2\hat{F}_j \otimes \hat{F}_j\Big)\nabla \otimes \nabla^S$$

and it has the symbol:

$$q_j(x, \xi) = 2(\hat{F}_j\xi) \otimes (\hat{F}_j\xi) - \frac{1}{2}\Big(|\xi|^2 I_d + (\xi \otimes \xi)\Big). \tag{4.14}$$

Lemma 4.3. *In dimension $d = 2$, let*

$$\xi = |\xi| \begin{pmatrix} \cos(\theta) \\ \sin(\theta) \end{pmatrix}, \qquad \hat{F}_j(x) = \frac{1}{\sqrt{2}} \begin{bmatrix} \cos(\alpha(x)) & \sin(\alpha(x)) \\ \sin(\alpha(x)) & -\cos(\alpha(x)) \end{bmatrix}. \tag{4.15}$$

Computing we have that

$$det(q_j(x,\xi)) = -\frac{|\xi|^4}{2} \sin^2\Big(2\theta - \alpha(x)\Big). \tag{4.16}$$

The conclusion is the operator is not elliptic for only one set of measurements given by (4.10) *with $J = 1$.*

Proof. In this case, we have

$$\begin{aligned} q_j(x,\xi) &= -\frac{1}{2}\Big(\begin{bmatrix} |\xi|^2 & 0 \\ 0 & |\xi|^2 \end{bmatrix} + \begin{bmatrix} \xi_1^2 & \xi_1\xi_2 \\ \xi_1\xi_2 & \xi_2^2 \end{bmatrix} \Big) + 2 \begin{bmatrix} A^2 & AB \\ AB & B^2 \end{bmatrix} \\ &= \begin{bmatrix} -\frac{1}{2}(|\xi|^2 + \xi_1^2) + 2A^2 & -\frac{\xi_1\xi_2}{2} + 2AB \\ -\frac{\xi_1\xi_2}{2} + 2AB & -\frac{1}{2}(|\xi|^2 + \xi_2^2) + 2B^2 \end{bmatrix} \end{aligned}$$

where

$$A = (\hat{F}_j\xi)_1, \qquad B = (\hat{F}_j\xi)_2.$$

Then,

$$\begin{aligned} \det(q_j(x,\xi)) &= \frac{1}{4}(|\xi|^2 + \xi_1^2)(|\xi|^2 + \xi_2^2) - B^2(|\xi|^2 + \xi_1^2) - A^2(|\xi|^2 + \xi_2^2) \\ &\quad +4A^2B^2 - \Big(2AB - \frac{\xi_1\xi_2}{2}\Big)^2 \\ &= \frac{|\xi|^4}{2} - |\xi|^2(A^2 + B^2) - B^2\xi_1^2 - A^2\xi_2^2 + 2AB\xi_1\xi_2 \\ &= \frac{|\xi|^4}{2} - |\xi|^2(A^2 + B^2) - (A\xi_2 - B\xi_1)^2 \end{aligned}$$

In addition, notice that using the representation (4.15), we have

$$A = (F_{11}\xi_1 + F_{12}\xi_2) = \frac{|\xi|}{\sqrt{2}}(\cos(\alpha)\cos(\theta) + \sin(\alpha)\sin(\theta)) = \frac{|\xi|}{\sqrt{2}}\cos(\alpha - \theta),$$

$$B = (F_{21}\xi_1 + F_{22}\xi_2) = \frac{|\xi|}{\sqrt{2}}(\sin(\alpha)\cos(\theta) + \cos(\alpha)\sin(\theta)) = \frac{|\xi|}{\sqrt{2}}\sin(\alpha - \theta).$$

So, the determinant of $q_j(x,\xi)$ can be written as

$$\begin{aligned}
\det(q_j(x,\xi)) &= \frac{|\xi|^4}{2} - |\xi|^2\Big(\frac{|\xi|^2}{2}\cos^2(\alpha-\theta) - \frac{|\xi|^2}{2}\sin^2(\alpha-\theta)\Big) - (A\xi_2 - B\xi_1)^2 \\
&= -(A\xi_2 - B\xi_1)^2 \\
&= -\Big(\frac{|\xi|^2}{\sqrt{2}}\cos(\alpha-\theta)\sin(\theta) - \frac{|\xi|^2}{\sqrt{2}}\sin(\alpha-\theta)\cos(\theta)\Big)^2 \\
&= -\frac{|\xi|^4}{2}\sin^2(2\theta-\alpha)
\end{aligned}$$

and we conclude the proof of the estimate on the principal symbol. Notice that for all $\hat{F}_j(x)$ with the structure given in equation (4.15), the operator $P_j(x,D)$ is not elliptic, since for all $x \in \Omega$ and for all $\hat{F}_j(x)$ it is possible to find $\xi = (\cos(\alpha(x)/2), \sin(\alpha(x)/2)) \in \mathbb{S}^1$ such that $\det(q_j(x,\xi)) = 0$, i.e., $q_j(x,\xi)$ is not of full rank. □

Remark 2. *Although this result gives us an idea about the ellipticity for the equation, this is a result of the ellipticity for the operator $P_j(x,D)$. Similar problems have been studied in [Bal+11; Bal13], where a result says that an analogue system (in scalar case) is in fact hyperbolic. It seems natural to linearize in nonlinear models, since the problem is reduced to a linear one, and better mathematical results are known to hold. In the remaining of the article, we show results concerning to linearization of the models in study.*

Linearisation of the model problem for J measurements

We consider the background pressure to be fixed, and let d be the dimension which is arbitrary for this system. The linearized problem for $j \in \{1,\dots,J\}$ is then given by

$$\begin{cases}
2\nabla\cdot\delta\mu\nabla^S u_j + 2\nabla\cdot\mu\nabla^S\delta u_j + \omega^2\delta u_j &= 0 & \text{in } \Omega, \\
\dfrac{\delta\mu}{2}|\nabla^S u_j|^2 + \mu\nabla^S u_j : \nabla^S\delta u_j &= \delta H_j & \text{in } \Omega, \\
\nabla\cdot\delta u_j &= 0 & \text{in } \Omega, \\
\delta u_j &= 0 & \text{on } \partial\Omega.
\end{cases} \tag{4.17}$$

We make the definition $w = (\delta\mu, \{\delta u_j\}_{j=1}^J)$ which allows us to re-write the system as:

$$\begin{cases}
\mathcal{L}w &= \mathcal{S} & \text{in } \Omega, \\
\mathcal{B}w &= g & \text{on } \partial\Omega.
\end{cases} \tag{4.18}$$

The principal symbol associated to (4.17) is, rearranging rows, the following:

$$\mathcal{P}_J(x,\xi) =$$

$$\begin{bmatrix}
\frac{|F_1|^2}{2} & i\mu(F_1\xi)^\intercal & 0 & \cdots & 0 \\
2iF_1\xi & -\mu\Big(|\xi|^2 I_d + (\xi\otimes\xi)\Big) & 0 & \cdots & 0 \\
0 & i\xi^\intercal & 0 & \cdots & 0 \\
\frac{|F_2|^2}{2} & 0 & i\mu(F_2\xi)^\intercal & \cdots & 0 \\
2iF_2\xi & 0 & -\mu\Big(|\xi|^2 I_d + (\xi\otimes\xi)\Big) & \cdots & 0 \\
0 & 0 & i\xi^\intercal & \cdots & 0 \\
\vdots & \vdots & \vdots & \ddots & \vdots \\
\frac{|F_J|^2}{2} & 0 & 0 & \cdots & i\mu(F_J\xi)^\intercal \\
2iF_J\xi & 0 & 0 & \cdots & -\mu\Big(|\xi|^2 I_d + (\xi\otimes\xi)\Big) \\
0 & 0 & 0 & \cdots & i\xi^\intercal
\end{bmatrix}$$

which is a matrix of size $J(d+2)\times(Jd+1)$. We can recognize the following family of submatrices

$$\rho_j(x,\xi) = \begin{bmatrix} \frac{|F_j|^2}{2} & i\mu(F_j\xi)^\intercal \\ 2iF_j\xi & -\mu\Big(|\xi|^2 I_d + (\xi\otimes\xi)\Big) \end{bmatrix} \tag{4.19}$$

and we have from the formulas for the determinant of block matrices that (see, for example, Section 6.2 in [**meyer2000matrix**]):

$$\det\Big(\rho_j(x,\xi)\Big) = 2^{d-1}\mu^d |F_j|^2 \det\Big(q_j(x,\xi)\Big), \tag{4.20}$$

where q_j is defined in (4.14). Note that Lemma 4.3 now says that the linearized operator $\mathcal{L}$ is not elliptic.
On the other hand, if we take determinant for the submatrices with the rows containing the highest power of ξ in $\mathcal{P}_j$, we obtain, by applying properties for determinant of block matrices, the following:

$$(-1)^{(J-1)d}\frac{\mu^{Jd}}{2^{(J-1)d}}|F_j|^2 \det\Big(|\xi|^2 I_d + \xi\otimes\xi\Big)^{J-1}\det\Big(q_j(x,\xi)\Big).$$

Definition 4.3. *We say that a family $\{Op(\rho_j(x,\xi))\}_{j=1}^J$ of operators is elliptic if $\rho_j(x,\xi)$ is invertible for all $x\in\Omega$ and all $j=1,\dots,J$ implies $\xi=0$.*

This definition is inspired by the one in [Bal14], Definition 2.1.

Lemma 4.4. *If $\{\rho_j\}$ forms an elliptic family and $|F_j|>0$ for all $x\in\Omega$ and $j=1,...J$, then the full linearized operator $\mathcal{L}(x,\xi)$ is elliptic.*

Proof. Let C_0 and $\{C_j\}_{j=1}^J$ be the submatrices of $\mathcal{P}_J$ defined by

$$C_0 = \begin{pmatrix} |F_1|^2 \\ 2iF_1\xi \\ 0 \\ |F_2|^2 \\ 2iF_2\xi \\ 0 \\ \vdots \\ |F_J|^2 \\ 2iF_J\xi \\ 0 \end{pmatrix}, \qquad C_j = \begin{pmatrix} 0 \\ \vdots \\ 0 \\ 2i\mu(F_j\xi)^\intercal \\ -\mu(|\xi|^2 I_d + \xi\otimes\xi) \\ i\xi^\intercal \\ 0 \\ \vdots \\ 0 \end{pmatrix} \leftarrow \text{row } ((j-1)(d+2)+1)$$

where $C_0 \in \mathcal{M}_{J(d+2)\times 1}(\mathbb{C})$ and $C_j \in \mathcal{M}_{J(d+2)\times d}(\mathbb{C})$ for $j = 1, \dots, J$.
Let $\xi \neq 0$. Then we can see easily that $-\mu(|\xi|^2 + \xi\otimes\xi)$ is invertible, hence C_j has complete column rank. In addition, if $j_1 \neq j_2$, then C_{j_1} and C_{j_2} do not have the same nonzero rows. If $\mathcal{L}(x,\xi)$ is not full rank, then it is clear that there exists j_0 and $\alpha_{j_0} \in \mathbb{R}^d\backslash\{0\}$ such that in the nonzero rows of C_{j_0} we have

$$\begin{pmatrix} |F_{j_0}|^2 \\ 2i\mu F_{j_0}\xi \\ 0 \end{pmatrix} = \begin{pmatrix} 2i\mu(F_{j_0}\xi)^\intercal \\ -\mu(|\xi|^2 I_d + \xi\otimes\xi) \\ i\xi^\intercal \end{pmatrix} \begin{pmatrix} \alpha_{j_0 1} \\ \vdots \\ \alpha_{j_0 d} \end{pmatrix}$$

and then we have that $\xi^\intercal \alpha_{j_0} = 0$ and

$$\begin{pmatrix} |F_{j_0}|^2 & 2i\mu(F_{j_0}\xi)^\intercal \\ 2i\mu F_{j_0}\xi & -\mu(|\xi|^2 I_d + \xi\otimes\xi) \end{pmatrix} \begin{pmatrix} -1 \\ \alpha_{j_0 1} \\ \vdots \\ \alpha_{j_0 d} \end{pmatrix} = \begin{pmatrix} 0 \\ \vdots \\ 0 \end{pmatrix}.$$

That is, $\rho_{j_0}(x,\xi)$ is not invertible. □

Theorem 4.3. *For $J = 2$, $d = 2$, if $\alpha_2(x) \neq \alpha_1(x) + k\pi$ for all $k \in \mathbb{Z}$ and for all $x \in \Omega$, then the differential operator corresponding with the system* (4.17) *is elliptic.*

Proof. We have to prove that

$$\det(q_j(x,\xi)) = 0 \ \ \forall j \ \Rightarrow \xi = 0$$

since equation (4.20) establishes that $\rho_j(x,\xi)$ is invertible if and only if $q_j(x,\xi)$ is invertible. If $\det(q_j(x,\xi)) = 0$ for $j = 1, 2$, then we have

$$\sin(2\theta - \alpha_1(x)) = 0 \quad \wedge \quad \sin(2\theta - \alpha_2(x)) = 0 \tag{4.21}$$

or

$$\xi = 0$$

but (4.21) implies

$$\alpha_2 = \alpha_1 + k\pi \quad \text{for some } k \in \mathbb{Z}$$

which is false by hypothesis. So we conclude that $\xi = 0$. That is, (q_1, q_2) forms an elliptic family. We conclude the proof using Lemma 4.4. □

4.4.2 Lopatinskii condition

We prove now the following in dimension $d = 2$.

Lemma 4.5. *Consider $v = (\mu, \{u_j\}_{j=1,\dots,J})$. Let $x \in \partial\Omega$, ν the outward unit normal to Ω at x, and $\zeta \in \mathbb{S}^{d-1}$ satisfying $\zeta \cdot \nu = 0$. Define $\tilde{v}(z) = v(x - \nu z)$. Then the only solution of the system of ODEs*

$$\begin{cases} \mathcal{P}_J(x, i\zeta + \nu\partial_z)\tilde{v} &= 0, \quad z > 0, \\ \mathcal{B}\tilde{v} &= 0, \quad z = 0, \end{cases} \tag{4.22}$$

such that $\tilde{v}(z) \to 0$ as $z \to \infty$ is $\tilde{v} \equiv 0$.

Proof. The system can be seen as the following

$$\begin{cases} |F_j|^2\tilde{\mu} + 2\mu\Big(F_j[i\zeta + \nu\partial_z]\Big)^{\intercal}\tilde{u}_j = 0, \quad z > 0, \\ F_j[i\zeta + \nu\partial_z]\tilde{\mu} - \dfrac{\mu}{2}\Big((i\zeta + \nu\partial_z)^2 I_d + (i\zeta + \nu\partial_z) \otimes (i\zeta + \nu\partial_z)\Big)\tilde{u}_j = 0, \quad z > 0, \\ i(i\eta + \nu\partial_z)^{\intercal}\tilde{u}_j = 0, \quad z > 0, \\ \tilde{u} = 0, \quad z = 0, \end{cases} \tag{4.23}$$

for all $j = 1, \dots J$.
We can eliminate $\tilde{\mu}$ using the first equation

$$\tilde{\mu} = -\frac{2\mu}{|F_j|^2}\Big(F_j[i\zeta + \nu\partial_z]\Big)^{\intercal}\tilde{u}_j. \tag{4.24}$$

Replacing it in the second equation, after some calculations we have

$$q_j(x, \nu)\partial_z^2\tilde{u}_j + ir_j(x, \nu, \zeta)\partial_z\tilde{u}_j + s_j(x, \zeta)\tilde{u}_j = 0 \tag{4.25}$$

for all $j = 1, \dots, J$, where q_j is the same matrix of previous sections, and r_j, s_j are real matrices given by

$$r_j(x, \nu, \zeta) = 2(\hat{F}_j\nu \otimes \hat{F}_j\zeta + \hat{F}_j\zeta \otimes \hat{F}_j\nu) - \frac{1}{2}(\nu \otimes \zeta + \zeta \otimes \nu), \quad s_j(x, \zeta) = -q_j(x, \zeta).$$

We look the imaginary part of (4.25):

$$r_j\partial_z\tilde{u}_j = 0, \quad z > 0.$$

After some calculations (see Lemma 4.6), we have

$$\det(r_j) \neq 0$$

so we have

$$\partial_z\tilde{u}_j = 0$$

and this implies $\tilde{u}_j \equiv 0$ since $\tilde{u}(0) = 0$. Then using (4.38) we obtain $\tilde{\mu} \equiv 0$. Therefore we conclude $\tilde{v} \equiv 0$. □

Lemma 4.6. *In dimension $d = 2$, we have $det(r_j(x, \nu, \zeta)) \neq 0$.*

Proof. We have

$$r_j(x,\nu,\zeta) \;=\; M+N$$

where

$$M \;=\; \begin{bmatrix} 2AC & AD+BC \\ AD+BC & 2BD \end{bmatrix},$$

$$N \;=\; -\frac{1}{2}\begin{bmatrix} 2\nu_1\zeta_1 & \nu_1\zeta_2+\zeta_1\nu_2 \\ \nu_1\zeta_2+\zeta_1\nu_2 & 2\nu_2\zeta_2 \end{bmatrix}$$

and

$$A=(\hat{F}\nu)_1, \quad B=(\hat{F}\nu)_2, \quad C=(\hat{F}\zeta)_1, \quad D=(\hat{F}\zeta)_2.$$

Since $\nu\cdot\zeta=0$, without loss of generality we can take $\zeta_1=-\nu_2$ and $\zeta_2=\nu_1$, and using the properties of $\hat{F}_j$ we have

$$C=(\hat{F}_j)_{11}\zeta_1+(\hat{F}_j)_{12}\zeta_2=-(\hat{F}_j)_{11}\nu_2+(\hat{F}_j)_{12}\nu_1=B,$$

$$D=(\hat{F}_j)_{21}\zeta_1+(\hat{F}_j)_{22}\zeta_2=-(\hat{F}_j)_{21}\nu_2+(\hat{F}_j)_{22}\nu_1=-A.$$

Then

$$r_j=\begin{bmatrix} 4AB+\nu_1\nu_2 & 2(B^2-A^2)-\frac{1}{2}(\nu_1^2-\nu_2^2) \\ 2(B^2-A^2)-\frac{1}{2}(\nu_1^2-\nu_2^2) & -(4AB+\nu_1\nu_2) \end{bmatrix}$$

and we can compute the determinant

$$-\det(r_j)=\Big(4AB+\nu_1\nu_2\Big)^2+\Big(2(B^2-A^2)-\frac{1}{2}(\nu_1^2-\nu_2^2)\Big)^2. \tag{4.26}$$

Using the fact that $\nabla^S u_j$ are divergence free, we have

$$A=\frac{1}{\sqrt{2}}\cos(\alpha_j-\theta), \quad B=\frac{1}{\sqrt{2}}\sin(\alpha_j-\theta)$$

where $\theta=\arg(\nu)$, so that $\nu=(\cos(\theta),\sin(\theta))$. Then

$$\begin{aligned} -\det(r_j) \;&=\; \Big(2\cos(\alpha_j-\theta)\sin(\alpha_j-\theta)+\cos(\theta)\sin(\theta)\Big)^2 \\ &\qquad +\Big((\cos^2(\alpha_j-\theta)-\sin^2(\alpha_j-\theta))+\frac{\cos^2(\theta)-\sin^2(\theta)}{2}\Big)^2 \\ &=\; \Big(\sin(2(\alpha_j-\theta))+\frac{\sin(2\theta)}{2}\Big)^2+\Big(\cos(2(\alpha_j-\theta))+\frac{\cos(2\theta)}{2}\Big)^2 \\ &=\; \frac{5}{4}+\cos(2\alpha_j-3\theta) \\ &\neq\; 0 \qquad \forall x,\nu,\zeta. \end{aligned}$$

□

Remark 3. *It should be possible to show the theorem holds under weaker assumptions given the form of the determinant* (4.26).

4.4.3 Stability estimates

In any dimension d with J measurements, we can see the problem (4.17) in the framework of Section 4.3. The Douglis-Niernberg numbers are

$$s_i = \begin{cases} -1 & \text{if } i = k' \cdot (d+2) + k'',\ k' = 0, 1, \dots, J,\ k'' = 0, 1, \\ 0 & \text{otherwise,} \end{cases}$$

$$t_j = \begin{cases} 1 & \text{if } j = 1, \\ 2 & \text{otherwise ,} \end{cases}$$

$$\sigma_k = -1,\ k = 1, \dots, Jd.$$

where $i = 1, \dots, J(d+2)$ and $j = 1, \dots, Jd+1$. The operator $\mathcal{A} = (\mathcal{L}, \mathcal{B})$ is defined from

$$\mathcal{X} = \prod_{j=1}^{Jd+1} H^{l+t_j}(\Omega)$$

to

$$\mathcal{Y} = \prod_{i=1}^{J(d+2)} H^{l-s_i}(\Omega) \times \prod_{j=1}^{Jd} H^{l-\sigma_j-1/2}(\partial\Omega)$$

where we choose l such that $2(l - s_i) > d$, $2(l - \sigma_k) > d$. In dimension $d = 2$, we can choose $l = 2$.
Moreover, if $d = 2$ and $J = 2$, the we have

$$\mathcal{X} = H^3(\Omega) \times \left(H^4(\Omega)^2\right)^2 \tag{4.27}$$

with norm

$$||(\delta\mu, \{\delta u_j\}_{j=1}^J)||_{\mathcal{X}} = ||\delta\mu||_{H^3(\Omega)} + \sum_{j=1}^{J} ||\delta u_j||_{H^4(\Omega)^2}$$

and

$$\mathcal{Y} = \left(H^3(\Omega) \times H^2(\Omega)^2 \times H^3(\Omega)\right)^2 \times \left(H^{5/2}(\partial\Omega)^2\right)^2 \tag{4.28}$$

with norm

$$||(\{\delta f_j^{pd}\}_{j=1}^J, \{\delta f_j^{ec}\}_{j=1}^J, \{\delta f_j^{div}\}_{j=1}^J, \{\delta g_j\}_{j=1}^J)||_{\mathcal{Y}}$$

$$= \sum_{j=1}^{J} ||\delta f_j^{pd}||_{H^3(\Omega)} + ||\delta f_j^{ec}||_{H^2(\Omega)^2} + ||\delta f_j^{div}||_{H^3(\Omega)} + ||\delta g_j||_{H^{5/2}(\partial\Omega)^2}.$$

Theorem 4.4. *Let $d = 2, J = 2$, we have the estimate for $w = (\delta\mu, \{\delta u_j\}_{j=1}^J)$ a solution to (4.17)*

$$||\delta\mu||_{H^3(\Omega)}+\sum_{j=1}^{2}||\delta u_j||_{H^4(\Omega)^2} \leq C\sum_{j=1}^{J}\Big(||\mathcal{L}_j^{ec}(\delta\mu,\delta u_j)||_{H^2(\Omega)^2}+||\mathcal{L}_j^{pd}(\delta\mu,\delta u_j)||_{H^3(\Omega)}$$

$$+||\mathcal{L}^{div}(\delta\mu,\delta u_j)||_{H^3(\Omega)}+||\mathcal{B}\delta u_j||_{H^{5/2}(\Omega)^2}\Big) \tag{4.29}$$

$$+C_2\Big(||\delta\mu||_{L^2(\Omega)^2}+\sum_{j=1}^{J}||\delta u_j||_{L^2(\Omega)^2}\Big)$$

where $\mathcal{L}_j^{ec}, \mathcal{L}_j^{pd}, \mathcal{L}^{div}$ are the parts of $\mathcal{L}$ coming from the elasticity equations, the power density measurements and the divergence condition, respectively. If $C_2 = 0$, then the inverse operator is locally well-defined.

Proof. Since $(\mathcal{L}, \mathcal{B})$ satisfies the Lopatinskii condition, by Theorem 4.2 we have the estimate

$$||w||_{\mathcal{X}} \leq C||(\mathcal{S}, g)||_{\mathcal{Y}} + C_2||w||_{L^2(\Omega)^{d\cdot J}}. \tag{4.30}$$

If $C_2 = 0$, then the inverse operator is locally well-defined. We remark that in dimension 2, we can choose $l = 2$. □

4.4.4 Injectivity

Lemma 4.7. *Let the dimension be $d = 2$. The boundary value problem given by*

$$\begin{cases} \tilde{\mathcal{L}}_j\delta u_j := -2\nabla\cdot\Big(\dfrac{2\mu}{|F_j|^2}(F_j : \nabla^S\delta u_j)F_j\Big) + 2\nabla\cdot\mu\nabla^S u_j + \omega^2\delta u_j = \tilde{f} \quad \text{in } \Omega, \\ \\ \tilde{\mathcal{B}}_j\delta u_j := \delta u_j = \tilde{g}_j \quad \text{on } \partial\Omega, \end{cases} \tag{4.31}$$

is elliptic. In addition, we have:

$$\sum_{j=1}^{2}||\delta u_j||_{H^4(\Omega)^2} \leq \tilde{C}\sum_{j=1}^{J}\Big(||\tilde{\mathcal{L}}_j\delta u_j||_{H^2(\Omega)^2}+||\tilde{\mathcal{B}}_j\delta u_j||_{H^{5/2}(\Omega)^2}\Big)+\tilde{C}_2\sum_{j=1}^{J}||\delta u_j||_{L^2(\Omega)^2}. \tag{4.32}$$

Proof. In fact, the principal symbol of the operator corresponding with this equation is $c \cdot q_j(x, \xi)$ where c is a constant, hence the ellipticity of the operator is given by Theorem 4.3. The Lopatinskii condition is given by the proof of Lemma 4.5. Therefore we have the proposed estimate by Theorem 4.2. □

Lemma 4.8. *Let $\mathcal{A}$ be the operator corresponding to the equation given in the previous lemma. Let the dimension be 2. If $\delta u_j \in ker(\tilde{\mathcal{L}}_j, \tilde{\mathcal{B}}_j)$, then*

$$\int_\Omega |\delta u_j|^2 \leq \frac{2||\mu||_{L^\infty}^2}{\omega^2}\int_\Omega |\nabla(\delta u_j)|^2. \tag{4.33}$$

Proof. Multiplying the equation (4.31) by δu_j, and integrating by parts we have

$$\int_\Omega 2\mu|\nabla^S \delta u_j : \hat{F}_j|^2 dx - \int_\Omega \mu|\nabla^S \delta u_j|^2 + \omega^2 \int_\Omega |\delta u_j|^2 dx = 0. \tag{4.34}$$

On the other hand, let $F_j^\perp$ be such that $F_j : F_j^\perp = 0$ and $|F_j^\perp| = |F_j|$. Then $\nabla^S \delta u_j$ can be expressed as

$$\nabla^S \delta u_j = (\nabla^S \delta u_j : \hat{F}_j)\hat{F}_j + (\nabla^S \delta u_j : \hat{F}_j^\perp)\hat{F}_j^\perp \tag{4.35}$$

and then

$$\int_\Omega \mu|\nabla^S \delta u_j|^2 = \int_\Omega \mu\Big(|\nabla^S \delta u_j : \hat{F}_j|^2 + |\nabla^S \delta u_j : \hat{F}_j^\perp|^2\Big)dx. \tag{4.36}$$

Summing (4.34) and (4.36) we have

$$\begin{aligned}
\omega^2 \int_\Omega |\delta u_j|^2 dx &= \int_\Omega \mu\Big(|\nabla^S \delta u_j : \hat{F}_j^\perp|^2 - |\nabla^S \delta u_j : \hat{F}_j|^2\Big)dx \\
&\leq \int_\Omega \mu\Big(|\nabla^S \delta u_j : \hat{F}_j|^2 + |\nabla^S \delta u_j : \hat{F}_j^\perp|^2\Big)dx \\
&= \int_\Omega \mu|\nabla^S \delta u_j|^2 dx
\end{aligned}$$

and we conclude noticing that

$$\begin{aligned}
|\nabla^S \delta u_j|^2 &= \frac{1}{4}\Big|\nabla \delta u_j + \nabla \delta u_j^\intercal\Big|^2 \\
&= \frac{1}{4}\Big(|\nabla \delta u_j|^2 + |\nabla \delta u_j^\intercal|^2 + 2\nabla \delta u_j : \nabla \delta u_j^\intercal\Big) \\
&\leq \frac{1}{4}\Big(2|\nabla \delta u_j|^2 + 2|\nabla \delta u_j^\intercal|^2\Big) \\
&= |\nabla \delta u_j|^2.
\end{aligned}$$

□

Lemma 4.9. *In dimension $d = 2$, there exists $\omega_0 > 0$ such that $\forall \omega \geq \omega_0$ we have $ker(\tilde{\mathcal{L}}_j, \tilde{\mathcal{B}}_j) = \{0\}$ for all j. In other words, the operator $(\tilde{\mathcal{L}}, \tilde{\mathcal{B}})$ is injective, where $\tilde{\mathcal{L}} = \{\tilde{\mathcal{L}}_j\}_{j=1}^J$ and $\tilde{\mathcal{B}} = \{\tilde{\mathcal{B}}_j\}_{j=1}^J$.*

Proof. From Lemma 4.7 with $(\tilde{\mathcal{L}}_j w, \tilde{\mathcal{B}}_j \delta u_j) = (0, 0)$ for all j and from Lemma 4.8, we have

$$\sum_{j=1}^J ||\delta u_j||_{H^4(\Omega)^2} \leq \tilde{C}_2 \sum_{j=1}^J ||\delta u_j||_{L^2(\Omega)^2} \leq \frac{\tilde{C}_2 ||\mu||_{L^\infty(\Omega)}}{\omega} \sum_{j=1}^J ||\nabla \delta u_j||_{L^2(\Omega)^2}.$$

If we take ω large enough such that $\tilde{C}_2||\mu||_{L^\infty} < \omega$, we can absorb the right side of the estimate into the left hand side. So we conclude $\delta u_j = 0$. □

As a result we have the following result.

Theorem 4.5. *Let $d = 2, J = 2$, $\omega \geq \omega_0$ as in the previous lemma and the hypothesis of Theorem 4.4. Then we have the estimate for $(\delta\mu, \delta u_j)$ a solution to* (4.17)

$$||\delta\mu||_{H^3(\Omega)} + \sum_{j=1}^{2} ||\delta u_j||_{H^4(\Omega)^2} \leq C \sum_{j=1}^{2} \Big(||\mathcal{L}_j^{ec}(\delta\mu, \delta u_j)||_{H^2(\Omega)^2} + ||\mathcal{L}_j^{pd}(\delta\mu, \delta u_j)||_{H^3(\Omega)} + ||\mathcal{L}^{div}(\delta\mu, \delta u_j)||_{H^3(\Omega)} + ||\mathcal{B}\delta u_j||_{H^{5/2}(\Omega)^2} \Big). \tag{4.37}$$

Proof. Considering equation (4.17) with the right hand side equal to zero, we can take the second equation and obtain

$$\delta\mu = -\frac{2\mu}{|F_j|^2} F_j : \nabla^S \delta u_k. \tag{4.38}$$

Then we replace $\delta\mu$ in the first equation, so we obtain the equation (4.31). By Lemma 4.9 we obtain $\delta u_j = 0$ and using equation (4.38) we conclude $\delta\mu = 0$. Hence, we can eliminate the terms multiplying C_2 in equation (4.29), which is valid because we have the hypothesis of Theorem 4.4. □

4.4.5 Fixed-point algorithm

We introduce the general fixed point Lemmas which are needed to solve nonlinear PDE with small data. Let J be a linear operator, and N a power nonlinearity. We view the nonlinear PDE as

$$\begin{aligned} J(w) &= N(w) \quad \text{in } \Omega, \\ w &= f \quad \text{in } \Omega, \\ w &= 0 \quad \text{on } \partial\Omega. \end{aligned}$$

The solution then looks like

$$w = w_{lin} + J^{-1} N(w). \tag{4.39}$$

We also have the following abstract iteration result:

Lemma 4.10. *[[Tao06] Prop 1.38] Let $\mathcal{N}, \mathcal{S}$ be two Banach spaces and suppose we are given an invertible linear operator $J : \mathcal{N} \to \mathcal{S}$ with the bound*

$$||J^{-1}F||_{\mathcal{S}} \leq C_0 ||F||_{\mathcal{N}} \tag{4.40}$$

for all $F \in \mathcal{N}$ and some $C_0 > 0$. Suppose that we are given a nonlinear operator $N : \mathcal{S} \to \mathcal{N}$ which is a sum of a u dependent part and a u independent part. Assume the u dependent part N_u is such that $N_u(0) = 0$ and obeys the following Lipschitz bounds

$$||N(u) - N(v)||_{\mathcal{N}} \leq \frac{1}{2C_0} ||u - v||_{\mathcal{S}} \tag{4.41}$$

for all $u, v \in B_\epsilon = \{u \in \mathcal{S} : ||u||_S \leq \epsilon\}$ for some $\epsilon > 0$. In other words we have that $||N||_{\dot{C}^{0,1}(B_\epsilon \to \mathcal{N})} \leq \frac{1}{2C_0}$. Then, for all $u_{lin} \in B_{\epsilon/2}$ there exists a unique solution $u \in B_\epsilon$ with the map $u_{lin} \mapsto u$ Lipschitz with constant at most 2. In particular we have that

$$||u||_{\mathcal{S}} \leq 2||u_{lin}||_{\mathcal{S}}. \tag{4.42}$$

Remark 4. *The proof of Lemma 4.10 consists in establishing the convergence of the following iterative sequence:*

$$u^{(n)} = \begin{cases} u_{lin} & \text{if } n = 0, \\ u_{lin} + J^{-1}N(u^{(n-1)}) & \text{if } n \geq 1. \end{cases}$$

Therefore, the Lemma 4.10 also establishes the convergence of this kind of sequences.

Given the abstract convergence Lemma above, we want to apply this to the linearised elasticity problem to give a direct proof of existence and uniqueness to the system (4.17).

We set the following notation:

- $v_j = (\mu, \{u_j\}_j)$ and $v = \{v_j\}_{j=1}^J$.
- Also, $v = v_0 + \delta v$, where $v_0 = (\mu_0, \{u_{0,j}\}_{j=1}^J) = \{v_j\}_{j=1}^J$.
- $\delta v = (\delta\mu, \{\delta u_j\}_j) = \{w_j\}_{j=1}^J = w$.
- $\mathcal{F}(v_j) = \begin{pmatrix} \frac{\mu}{2}|\nabla^S u_j|^2 \\ 2\nabla \cdot \mu\nabla^S u_j + \omega^2 u_j \\ \nabla \cdot u_j \end{pmatrix}$, $\mathcal{H}_j = \begin{pmatrix} H_j \\ G_j \\ 0 \end{pmatrix}$, $\mathcal{B}v_j = g_j$.
- $\mathcal{F}v = \{\mathcal{F}v_j\}_{j=1}^J$, $\mathcal{H} = \{\mathcal{H}_j\}_{j=1}^J$, $\mathcal{B}v = \{\mathcal{B}v_j\}_{j=1}^J$.
- $\mathcal{L}_j = \mathcal{F}'(v_{0j})$, that is,
$$\mathcal{L}_j w_j = \mathcal{F}'(v_{0j})w_j = \begin{pmatrix} \frac{\delta\mu}{2}|\nabla^S u_{0j}|^2 + \mu\nabla^S u_{0j} : \nabla^S \delta u_{0j} \\ 2\nabla \cdot \delta\mu\nabla^S u_{0j} + 2\nabla \cdot \mu\nabla^S \delta u_{0j} + \omega^2 \delta u_{0j} \\ \nabla \cdot \delta u_{0j} \end{pmatrix}.$$
- $\mathcal{S}_j = \begin{pmatrix} \delta H_j \\ \delta G_j \\ 0 \end{pmatrix}$.
- $\mathcal{L}w = \{\mathcal{L}_j w_j\}_{j=1}^J$, $\mathcal{S} = \{\mathcal{S}_j\}_{j=1}^J$.
- $\mathcal{H}_0 := \mathcal{F}(v_{0j})$, $g_0 = \mathcal{B}v_0$.

And consider the following nonlinear problem:

$$\begin{cases} \mathcal{F}(v_0 + w) &= \mathcal{H} & \text{in } \Omega, \\ \mathcal{B}w &= g - g_0 & \text{on } \partial\Omega, \end{cases} \tag{4.43}$$

and the linear problem

$$\begin{cases} \mathcal{L}w &= \mathcal{S} & \text{in } \Omega, \\ \mathcal{B}w &= g - g_0 & \text{on } \partial\Omega. \end{cases} \tag{4.44}$$

The system (4.44) can be written as

$$\mathcal{A}w = \begin{pmatrix} \mathcal{S} \\ q - q_0 \end{pmatrix}. \tag{4.45}$$

Note that

$$\mathcal{F}(v_0 + w) = \mathcal{F}(v_0) + \mathcal{F}'(v_0)w + \mathcal{G}(w; v_0)$$

where $\mathcal{G}(w; v_0)$ is given by

$$\mathcal{G}_j(w; v_0) = \begin{pmatrix} \delta\mu\nabla^S u_{0j} : \nabla^S \delta u_j + \dfrac{(\mu_0 + \delta\mu)}{2}|\nabla^S \delta u_j|^2 \\ 2\nabla \cdot \delta\mu\nabla^S \delta u_j \\ 0 \end{pmatrix} \tag{4.46}$$

is such that

$$||(\mathcal{G}(w; v_0)||_{\mathcal{Y}} \leq C||w||^2_{\mathcal{X}} \tag{4.47}$$

where the constant C depends only on the $L^\infty(\Omega)$ norm of $|\nabla^S u_j|$ and μ for $j = 1, 2$ so that we can write the problem as

$$\begin{cases} \mathcal{L}w &= \mathcal{H} - \mathcal{H}_0 - \mathcal{G}(w; v_0) & \text{in } \Omega, \\ \mathcal{B}w &= g - g_0 & \text{on } \partial\Omega. \end{cases} \tag{4.48}$$

We define the following fixed point Algorithm:

Algorithm 1:

Input.

- A function $v_0 = (\mu_0, \{u_{0j}\})$, where μ_0 is given and then $u_{0,j}$ is the solution of the system:

$$\begin{cases} 2\nabla \cdot \mu_0\nabla^S u_j + \omega^2 u_j &= -\nabla p_j & \text{in } \Omega, \\ \nabla \cdot u_j &= 0 & \text{in } \Omega, \\ u_j &= g_j & \text{on } \partial\Omega. \end{cases} \tag{4.49}$$

- Observations $\mathcal{H}$ in Ω and boundary information g on $\partial\Omega$, i.e., $\mathcal{H} = \mathcal{F}(v_0 + w_{true})$ and $g = g_0 + \mathcal{B}w_{true}$.
- A tolerance $\varepsilon > 0$.

Steps.

- Compute $\mathcal{H}_0$ via the formula $\mathcal{H}_0 = \mathcal{F}(v_0)$.
- Define $w^0 = 0$.
- Iterations, from k to $k + 1$:
  - $w^{k+1} = \mathcal{I}(w^k) := \mathcal{A}^{-1}(\mathcal{H} - \mathcal{H}_0 - \mathcal{G}(w^k; v_0), g - g_0)$,
  - Stop if $||w^{k+1} - w^k|| < \varepsilon$.
- Define $v = v_0 + w^{k+1}$

Return v

Lemma 4.11. *There exist a constant $c_1 = c_1(\varepsilon) > 0$ such that*

$$||\mathcal{G}(w; v_0) - \mathcal{G}(\tilde{w}; v_0)||_{\mathcal{Y}} \leq c_1\Big(||\delta\mu - \delta\tilde{\mu}||_{H^3(\Omega)} + \sum_j ||\delta u_j - \delta\tilde{u}_j||_{(H^4(\Omega))^2}\Big) \tag{4.50}$$

provided $||\delta\mu||_{H^3(\Omega)}, ||\delta u_j||_{H^4(\Omega)^2} \leq \varepsilon$, for some $\varepsilon > 0$. Such a constant satisfies $c_1(\varepsilon) \to 0$ whenever $\varepsilon \to 0$.

Proof. The definition of $\mathcal{G}_j(w, v_0)$ in (4.46), implies $\mathcal{G}_j(w, v_0)$ is a differentiable function of w. The mean value theorem gives the result. Alternatively, using that $H^2(\Omega)^d$ and $H^3(\Omega)^d$ are Banach algebras gives a bound for c_1:

$$c_1 \leq C_{BA}\varepsilon\Big(JC_{BA}\max_j ||u_{0j}||_{H^4(\Omega)^d} + J||\mu_0||_{H^3(\Omega)} + 5\varepsilon\Big)$$

with $C_{BA} > 0$ the constant from the bound given by the fact $H^2(\Omega)$ and $H^3(\Omega)$ are Banach algebras, c.f. [Cia88] Theorem 6.1-4. □

Theorem 4.6. *If $\varepsilon > 0$ is sufficiently small so that*

$$c_1(\varepsilon)||\mathcal{A}^{-1}||_{\mathcal{L}(\mathcal{Y},\mathcal{X})} < \frac{1}{2}$$

where $c_1(\varepsilon)$ is given by the previous Lemma. Then the algorithm converges if in addition we have

$$||(\mathcal{H} - \mathcal{H}_0, g - g_0)||_{\mathcal{X}} \leq \frac{\varepsilon}{2},$$

and we obtain

$$||w||_{\mathcal{X}} < \varepsilon. \tag{4.51}$$

Proof. We take

$$J = \mathcal{A}, \quad N(w) = (\mathcal{G}(w; v_0), 0), \quad w_{lin} = (\mathcal{H} - \mathcal{H}_0, g - g_0).$$

Because the nonlinearity satisfies the conditions for the fixed point iteration by Lemma 4.11 application of the previous convergence Lemma 4.10 gives the desired result. □

Remark 5. *Note that the bound on $\mathcal{A}^{-1}\tilde{w}$ can be made precise by taking the constant from (4.37), with $w = \mathcal{A}^{-1}\tilde{w}$, but it depends on the constant C appearing in Theorem 4.2.*

4.5 Model with generic forcing term $f(u)$

Let $f \in \mathcal{C}^3(H^3(\mathbb{R}^d)^d, L^2(\mathbb{R}^d)^d)$ be a differentiable function whose symbol is a polynomial with degree at most 1. The model studied in this section is

$$\begin{cases} 2\nabla \cdot \mu\nabla^S u_j + \omega^2 u_j - f(u_j) &= -\nabla p_j & \text{in } \Omega, \\ \dfrac{\mu}{2}|\nabla^S u_j|^2 - f(u_j) \cdot u_j &= H_j & \text{in } \Omega, \\ \nabla \cdot u_j &= 0 & \text{in } \Omega, \\ u_j &= g_j & \text{on } \partial\Omega, \end{cases} \tag{4.52}$$

where $j = 1, \dots, J$. The motivation for considering the term $f(u_j)$ is to have a first intuition on more general nonlinear elasticity models in dimension $d = 2$. In [Wat19], a simplified nonlinear elasticity model is studied in dimension $d = 3$ with scalar valued functions.

The system (4.52) can be written as

$$\begin{cases} \mathcal{F}_{FT} v &= \mathcal{H} \quad \text{in } \Omega, \\ \mathcal{B} v &= g \quad \text{on } \partial\Omega, \end{cases} \tag{4.53}$$

where $v = (\mu, \{u_j\}_{j=1}^J)$. The linearized problem for $j \in \{1, \dots, J\}$ is then given by

$$\begin{cases} 2\nabla \cdot \delta\mu \nabla^S u_j + 2\nabla \cdot \mu \nabla^S \delta u_j + \omega^2 \delta u_j &= Df(u_j)\delta u_j \quad \text{in } \Omega, \\ W_j[\delta\mu, \delta u_j] &= \delta H_j \quad \text{in } \Omega, \\ \nabla \cdot \delta u_j &= 0 \quad \text{in } \Omega, \\ \delta u_j &= 0 \quad \text{on } \partial\Omega, \end{cases} \tag{4.54}$$

where

$$W_j[\delta\mu, \delta u_j] = \frac{\delta\mu}{2} |\nabla^S u_j|^2 + \mu \nabla^S u_j : \nabla^S \delta u_j - (Df(u_j)\delta u_j) \cdot u_j - f(u_j) \cdot \delta u_j$$

and if we take $w = (\delta\mu, \{\delta u_j\}_{j=1}^J)$ it can be re-written as

$$\begin{cases} \mathcal{L}_{FT} w &= \mathcal{S} \quad \text{in } \Omega, \\ \mathcal{B} w &= g \quad \text{on } \partial\Omega, \end{cases} \tag{4.55}$$

and it can be seen as the equation

$$\mathcal{A}_{FT} w = \begin{pmatrix} \mathcal{S} \\ g \end{pmatrix}.$$

4.5.1 Ellipticity and Lopatinskii condition

The principal symbol associated to (4.54) measurements is exactly $\mathcal{P}_J(x, \xi)$ given in section (4.4.1). That is, for $J = 2$ measurements:

$$\mathcal{P}_J(x, \xi) = \begin{bmatrix} \frac{|F_1|^2}{\mu} & i\mu(F_1\xi)^\intercal & 0 \\ 2iF_1\xi & -\mu\Big(|\xi|^2 + (\xi \otimes \xi)\Big) & 0 \\ 0 & i\xi^\intercal & 0 \\ \frac{|F_2|^2}{2} & 0 & i\mu(F_2\xi)^\intercal \\ 2iF_2\xi & 0 & -\mu\Big(|\xi|^2 + (\xi \otimes \xi)\Big) \\ 0 & 0 & i\xi^\intercal \end{bmatrix}$$

which is a matrix of size $J(d+2) \times (Jd+1)$.

Corollary 4.1. *Let $d = 2, J = 2$. Then the operator $\mathcal{L}_{FT}$ is elliptic and $\mathcal{B}$ covers $\mathcal{L}_{FT}$. Moreover we have the estimate for $w = (\delta\mu, \{\delta u_j\}_{j=1}^2)$ a solution to* (4.54)

$$||\delta\mu||_{H^3(\Omega)} + \sum_{j=1}^{2} ||\delta u_j||_{H^4(\Omega)^2} \leq C \sum_{j=1}^{2} \Big(||\mathcal{L}_{FT,j}^{ec}(\delta\mu, \delta u_j)||_{H^2(\Omega)^2} + ||\mathcal{L}_{FT,j}^{pd}(\delta\mu, \delta u_j)||_{H^3(\Omega)} + ||\mathcal{L}_{FT}^{div}(\delta\mu, \delta u_j)||_{H^3(\Omega)} + ||\mathcal{B}\delta u_j||_{H^{5/2}(\Omega)^2} \Big) + C_2 \Big(||\delta\mu||_{L^2(\Omega)^2} + \sum_{j=1}^{2} ||\delta u_j||_{L^2(\Omega)^2} \Big) \tag{4.56}$$

where $\mathcal{L}_{FT,j}^{ec}, \mathcal{L}_{FT,j}^{pd}, \mathcal{L}_{FT}^{div}$ are the parts of $\mathcal{L}_{FT}$ coming from the elasticity equations, the power density measurements and the divergence condition, respectively.

Proof. Since the ellipticity and Lopatinskii condition depend only on the principal symbol, then we have the result inmediatly from Theorem 4.4. □

4.5.2 Injectivity

Lemma 4.12. *The following boundary problem is elliptic:*

$$\begin{cases} L_{j,FT}[\delta u_j] = 0 & \text{in } \Omega, \\ \nabla \cdot \delta u_j = 0 & \text{in } \Omega, \\ \delta u_j = 0 & \text{on } \partial\Omega, \end{cases} \tag{4.57}$$

for $j = 1, 2$, $d = 2$, where

$$L_{j,FT}[\delta u_j] = 2\nabla\Big(\Big[-\frac{2\mu}{|F|^2}(F : \nabla^S \delta u_j) + h(u_j)\delta u_j \Big] F_j \Big) + 2\nabla \cdot \mu \nabla^S \delta u_j + \omega^2 \delta u_j - Df(u_j)\delta u_j$$

and

$$h(u_j) = \frac{2}{|F_j|^2}\Big(u_j^\intercal Df(u_j) - f(u_j)^\intercal \Big)$$

is elliptic. Therefore we have

$$\sum_{j=1}^{2} ||\delta u_j||_{H^4(\Omega)^2} \leq C \sum_{j=1}^{2} \Big(||\mathcal{L}_{FT}\delta u_j||_{H^2(\Omega)^2} + ||\mathcal{B}_{FT}\delta u_j||_{H^{5/2}(\Omega)^2} \Big) + C_2 \sum_{j=1}^{2} ||\delta u_j||_{L^2(\Omega)^2}.$$

Proof. In fact, since the symbol of f is a polynomial with degree at most 1, we notice that the principal symbol for the system (4.57) is given by the principal symbol associated to (4.17). The Lopatinskii condition is satisfied because it depends only on the principal symbol. Therefore we conclude the ellipticity and the estimate by considering Theorem 4.4. □

Lemma 4.13. *Let $\tilde{\mathcal{A}}_{FT}$ be the operator corresponding to the equation given in the previous lemma. In dimension 2, if $\{\delta u_j\} \in ker(\tilde{\mathcal{A}}_{FT})$, then*

$$\int_\Omega |\delta u_j|^2 \leq \tilde{C}(\omega^2) \int_\Omega |D\delta u_j|^2 \tag{4.58}$$

where $\tilde{C}(\omega^2) = \dfrac{1 + 2||\mu||_{L^\infty}}{\omega^2 - (||Df(u_j)||_{L(H^1,L^2)} + ||h(u_j)||_{L(H^1,L^2)})}$.

Proof. If $\delta u_j \in \ker(\tilde{\mathcal{A}}_{FT})$, then:

$$\left\{\begin{array}{rcll} L_{j,FT}[\delta\mu, \delta u_j] & = & 0 & \text{in } \Omega, \\ \nabla \cdot \delta u_j & = & 0 & \text{in } \Omega, \\ \delta u_j & = & 0 & \text{on } \partial\Omega. \end{array}\right. \tag{4.59}$$

Note that

$$\frac{1}{|F_j|^2}(Df(u_j)\delta u_j) \cdot u_j = \frac{1}{|F_j|^2}(u_j^{\intercal} Df(u_j))\delta u_j.$$

From the second equation in (4.59) we obtain:

$$\delta\mu = -\frac{2\mu}{|F_j|^2}(F_j : \nabla^S \delta u_j) + h(u_j)\delta u_j.$$

On the other hand, multiplying the first equation of (4.59) by δu_j and integrating, we obtain:

$$\begin{aligned} \omega^2 \int_\Omega |\delta u_j|^2 &= \int_\Omega (Df(u_j)\delta u_j) \cdot \delta u_j - 4\int_\Omega \mu |\hat{F}_j : \nabla^S \delta u_j|^2 \\ &\quad + 2\int_\Omega (h(u_j)\delta u_j)(\hat{F}_j : \nabla^S \delta u_j) + 2\int_\Omega \mu |\nabla^S \delta u_j|^2 \end{aligned}$$

and considering the identity (4.36):

$$\begin{aligned} \omega^2 \int_\Omega |\delta u_j|^2 &= \int_\Omega (Df(u_j)\delta u_j) \cdot \delta u_j + 2\int_\Omega (h(u_j)\delta u_j)(\hat{F}_j : \nabla^S \delta u_j) \\ &\quad + 2\int_\Omega \mu |\hat{F}_j^{\perp} : \nabla^S \delta u_j|^2 - 2\int_\Omega \mu |\hat{F}_j : \nabla^S \delta u_j|^2 \\ &\leq \Big(||Df(u_j)||_{L(H^1,L^2)} + ||h(u_j)||_{L(H^1,L^2)} \Big) ||\delta u_j||_{L^2}^2 \\ &\quad + (1 + 2||\mu||_{L^\infty}) \int_\Omega |\nabla^S \delta u_j|^2. \end{aligned}$$

Therefore we obtain the desired result

$$\int_\Omega |\delta u_j|^2 \leq \frac{1 + 2||\mu||_{L^\infty}}{\omega^2 - (||Df(u_j)||_{\mathcal{L}(H^3,L^2)} + ||h(u_j)||_{\mathcal{L}(H^3,L^2)})} \int_\Omega |\nabla u_j|^2.$$

□

Lemma 4.14. *In dim 2, there exists $\omega_0 > 0$ such that $\forall \omega \geq \omega_0$ we have $ker(\tilde{\mathcal{A}}_{FT}) = \{0\}$. In other words, the operator is injective.*

Proof. From Corollary 4.1 taking $\tilde{\mathcal{A}}_{FT} w = (0, 0)$, we have, using the previous lemma:

$$\sum_j ||\delta u_j||_{H^4(\Omega)^2} \leq C_2 \sum_j ||\delta u_j||_{L^2(\Omega)^2} \leq C_2 \tilde{C}(\omega) \sum_j ||\nabla \delta u_j||_{L^2}$$

where $\tilde{C}(\omega^2)$ is given in (4.58). If we take ω large enough such that $C_2\tilde{C}(\omega^2) < 1$, we can absorb the right side of the estimate. So we conclude that $\delta u_j = 0$. □

As a result we have the following corollary.

Corollary 4.2. *Let $d = 2, J = 2$, and $\omega \geq \omega_0$ as in the previous lemma. Then we have the estimate for $(\delta\mu, \delta u_j)$ a solution to* (4.54)

$$||\delta\mu||_{H^3(\Omega)} + \sum_{j=1}^{2} ||\delta u_j||_{H^4(\Omega)^2} \leq C \sum_{j=1}^{2} \Big(||\mathcal{S}_j||_{H^3(\Omega)\times H^2(\Omega)^2} + ||g_j||_{H^{5/2}(\Omega)^2} \Big). \tag{4.60}$$

Proof. Considering equation (4.54) with the terms not depending on u_j equal to zero, we can take the second equation and obtain

$$\delta\mu = \frac{1}{|F_j|^2} \Big[\Big(f(u_j) + u_j^{\intercal} Df(u_j) \Big) \cdot \delta u_j - 2\mu \nabla^S u_j : \nabla^S \delta u_j \Big]. \tag{4.61}$$

Then we replace $\delta\mu$ in the first equation, so we obtain the equation (4.57). By Lemma 4.14 we obtain $\delta u_j = 0$ and using equation (4.61) we conclude $\delta\mu = 0$. Hence, we can eliminate the terms multiplying C_2 in equation (4.56), which is valid because we have the hypothesis of Corollary 4.1. □

4.5.3 Fixed point algorithm

We note that $\mathcal{F}_{FT} = \mathcal{F} + \mathcal{F}_{add}$ and $\mathcal{L}_{FT} = \mathcal{L} + \mathcal{L}_{add}$ with $\mathcal{F}$ and $\mathcal{L}$ given in the previous case and

$$\mathcal{F}_{add} v_j = \begin{pmatrix} -f(u_j) \cdot u_j \\ -f(u_j) \\ 0 \end{pmatrix}, \quad \mathcal{L}_{j,add} v_j = \begin{pmatrix} -(Df(u_j)\delta u_j) \cdot u_j - f(u_j) \cdot \delta u_j \\ -Df(u_j)\delta u_j \\ 0 \end{pmatrix}.$$

In addition we define $\mathcal{G}_{FT}(w; v) = \mathcal{F}(v + w) - \mathcal{F}v - \mathcal{L}w$. It is clear that $\mathcal{G}_{FT}(w; v) = \mathcal{G}(w; v) + \mathcal{G}_{add}(w; v)$ with $\mathcal{G}$ defined as before and

$$\mathcal{G}_{j,add}(w; v) = \begin{pmatrix} o(\delta u_j) \cdot (u_j + \delta u_j) - (Df(u_j)\delta u_j) \cdot u_j \\ o(\delta u_j) \\ 0 \end{pmatrix}$$

where

$$o(\delta u_j) = \int_0^1 (1 - t) D^2 f(u + t\delta u_j)[\delta u_j, \delta u_j] dt$$

comes from Taylor's formula

$$f(u_j + \delta u_j) = f(u_j) + Df(u_j)\delta u_j + \int_0^1 (1 - t) D^2 f(u + t\delta u_j)[\delta u_j, \delta u_j] dt.$$

The Fixed Point Algorithm for this case is the same as Algorithm 1, with the following changes:

- Instead of $\mathcal{F}, \mathcal{L}, \mathcal{G}, \mathcal{A}$, we use $\mathcal{F}_{FT}, \mathcal{L}_{FT}, \mathcal{G}_{FT}, \mathcal{A}_{FT}$
- In the step of solving equation (4.49), we solve

$$\begin{cases} 2\nabla \cdot \mu_0 \nabla^S u_j + \omega^2 u_j - f(u_j) &= -\nabla p_j & \text{in } \Omega, \\ \nabla \cdot u_j &= 0 & \text{in } \Omega, \\ u_j &= g_j & \text{on } \partial\Omega. \end{cases} \tag{4.62}$$

Lemma 4.15. *There exists a constant $c_2 = c_2(\varepsilon) > 0$ such that*

$$||\mathcal{G}_{FT}(w; v_0) - \mathcal{G}_{FT}(\tilde{w}; v_0)||_{\mathcal{Y}} \leq c_2\Big(||\delta\mu - \delta\tilde{\mu}||_{H^3(\Omega)} + \sum_j ||\delta u_j - \delta\tilde{u}_j||_{(H^4(\Omega))^2}\Big), \tag{4.63}$$

provided $||\delta\mu||_{H^3(\Omega)}, ||\delta u_j||_{H^4(\Omega)^2} \leq \varepsilon$, for some $\varepsilon > 0$.

Proof. Let

$$\begin{aligned}\psi(\delta u_j, \delta\tilde{u}_j) &= D^2 f(u + t\delta u_j)[\delta u_j, \delta u_j] - D^2 f(u + t\delta\tilde{u}_j)[\delta\tilde{u}_j, \delta\tilde{u}_j] \\ &= D^2 f(u_j + t\delta u_j)[\delta u_j - \delta\tilde{u}_j, \delta u_j] + D^2 f(u_j + t\delta u_j)[\delta\tilde{u}_j, \delta u_j - \delta\tilde{u}_j] \\ &\quad + \Big(D^2 f(u_j + t\delta u_j) - D^2 f(u_j + t\delta\tilde{u}_j)\Big)[\delta\tilde{u}_j, \delta\tilde{u}_j],\end{aligned}$$

hence

$$||\psi(\delta u_j, \delta\tilde{u}_j)||_{L^2(\Omega)^2} \leq c_3\varepsilon||\delta u_j - \delta\tilde{u}_j||_{H^1(\Omega)^2},$$

with c_3 being the maximum between

$$2\sup\{||D^2 f(h)||_{\mathcal{L}(H^4(\Omega)^2, \mathcal{L}(H^4(\Omega)^2, L^2(\Omega)^2))};\ ||u_j - h||_{H^3(\Omega)^2} \leq \varepsilon\}$$

and

$$2\varepsilon^2\sup\{||D^3 f(h)||_{\mathcal{L}(H^4(\Omega)^2, \mathcal{L}(H^4(\Omega)^2, \mathcal{L}(H^4(\Omega)^2, L^2(\Omega)^2)))}; ||u_j - h||_{H^4(\Omega)^2} \leq \varepsilon\}$$

given by the mean value theorem over $D^2 f$. Then

$$\begin{aligned}||o(\delta u_j) - o(\delta\tilde{u}_j)||_{L^2(\Omega)^2} &= \int_0^1 |1 - t|c_3\varepsilon||\delta u_j - \delta\tilde{u}_j||_{H^4(\Omega)^2} dt \\ &\leq c_3\varepsilon||\delta u_j - \delta\tilde{u}_j||_{H^4(\Omega)^2}.\end{aligned}$$

Then the conclusion is direct from Lemma 4.11 and the definition of $\mathcal{G}_{add}$. □

Then we have the following analogue to Theorem 4.6:

Corollary 4.3. *If $\varepsilon > 0$ is sufficiently small so that*

$$c_2(\varepsilon)||\mathcal{A}_{FT}^{-1}||_{\mathcal{L}(\mathcal{Y}, \mathcal{X})} < \frac{1}{2}$$

then the algorithm of this case converges if in addition we have

$$||(\mathcal{H} - \mathcal{H}_0, g - g_0)||_{\mathcal{X}} \leq \frac{\varepsilon}{2},$$

and we obtain

$$||w||_{\mathcal{X}} < \varepsilon. \tag{4.64}$$

4.6 Linear Elasticity with internal measurements, incompressible case

The model considered in this section is given by the system (4.9), but with internal measurements of u_j, i.e.,

$$u_j = H_j \quad \text{in } \Omega. \tag{4.65}$$

In [WS15], Proposition 1 c), they proved that there is no ellipticity for the joint recovery of μ and p. Therefore we must either apply the curl to the operator to remove ∇p or we must hold ∇p fixed. This last case is studied in [WS15], establishing the ellipticity and Lopatinskii condition with at least one measurement, but null kernel with two measurements. If we are to use the model with ∇p fixed, then we know that λ is large. This causes serious convergence problems when considering the Saint-Venant model of non-linear elasticity, for example with results like 4.10, where we need to have a contraction map, so we chose to apply the curl operator, which eliminates the λ terms.

Hence, we consider the model

$$\begin{cases} \omega^2 \nabla \times u_j + 2\nabla \times \nabla \cdot \mu \nabla^S u_j &= 0 & \text{in } \Omega, \\ u_j &= H_j & \text{in } \Omega, \\ \nabla \cdot u_j &= 0 & \text{in } \Omega, \\ u_j &= g_j & \text{on } \partial\Omega. \end{cases} \tag{4.66}$$

The linearization of (4.66) gives the following system:

$$\begin{cases} \omega^2 \nabla \times \delta u_j + 2\nabla \times \nabla \cdot \mu \nabla^S \delta u_j + 2\nabla \times \nabla \cdot \delta\mu \nabla^S u_j &= 0 & \text{in } \Omega, \\ \delta u_j &= \delta H_j & \text{in } \Omega, \\ \nabla \cdot \delta u_j &= 0 & \text{in } \Omega, \\ \delta u_j &= 0 & \text{on } \partial\Omega. \end{cases} \tag{4.67}$$

4.6.1 Ellipticity

Let $\Sigma_{\text{curl}}(\xi)$ be the symbol of the curl operator, that is

$$\Sigma_{\text{curl}}(\xi) = i \begin{pmatrix} -\xi_2 & \xi_1 \end{pmatrix}$$

in dimension 2, and

$$\Sigma_{\text{curl}}(\xi) = i \begin{bmatrix} 0 & -\xi_3 & \xi_2 \\ \xi_3 & 0 & -\xi_1 \\ -\xi_2 & \xi_1 & 0 \end{bmatrix}$$

in dimension 3. Note that if $b \in \mathbb{R}^d$, then $\Sigma_{\text{curl}}(\xi)\, b = i\, b \times \xi$.

The linearized system then has the following principal symbol:

$$\mathcal{P}(x,\xi) = \begin{bmatrix} 2(\nabla^S u\ \xi) \times \xi & -2\mu\ \Sigma_{\text{curl}}(\xi)\Big(|\xi|^2 I_d + \xi \otimes \xi\Big) \\ 0 & I_d \\ 0 & i\xi^\intercal \end{bmatrix}$$

with is a matrix with size $(2d+1) \times (d+1)$. Let $\xi \neq 0$ and $\boldsymbol{C}_1, \ldots, \boldsymbol{C}_{d+1}$ the columns of that matrix. Let $\alpha_1, \ldots, \alpha_{d+1} \in \mathbb{C}$ such that

$$\sum_{i=1}^{d+1} \alpha_i \boldsymbol{C}_i = \boldsymbol{0}.$$

We see that, because of the identity matrix, necessarily $\alpha_2 = \cdots = \alpha_{d+1} = 0$, so we have to analyse the equation $\alpha_1 \boldsymbol{C}_1 = \mathbf{0}$. This last equation can be reduced to the case studied in [AWZ15], giving the nonellipticity for 1 measurement. If we consider the augmented system for 2 measurements, we obtain the ellipticity as in [AWZ15] for 3 dimensions. Notice that this computation in 2 dimensions corrects a mistake in the original computations presented there.
The symbol for the augmented system is

$$\mathcal{P}_2(x,\xi) = \begin{bmatrix} 2(\nabla^S u_1\ \xi)\times\xi & P(\xi) & 0 \\ 0 & I_d & 0 \\ 0 & i\xi^\intercal & 0 \\ 2(\nabla^S u_2\ \xi)\times\xi & 0 & P(\xi) \\ 0 & 0 & I_d \\ 0 & 0 & i\xi^\intercal \end{bmatrix}$$

where

$$P(\xi) = -2\mu\Sigma_{\text{curl}}(\xi)\Big(|\xi|^2 I_d + \xi\otimes\xi\Big).$$

In order to have ellipticity, that is, in order to $\mathcal{P}_2(x,\xi)$ being column rank, we need that he following condition holds:

$$|(\nabla^S u_1\xi)\times\xi| + |(\nabla^S u_2\xi)\times\xi| \neq 0 \quad \forall |\xi| \neq 0. \tag{4.68}$$

This is slightly different to the case in [AWZ15] where the following is considered:

$$|(\nabla^S u_1\xi)\times\xi| + |(\nabla^S u_2\xi)\times\xi| \geq |\xi|^2. \tag{4.69}$$

It is unclear to the authors which condition is more natural.

Condition (4.68) is equivalent to the following: let $A^{(j)} = \nabla^S u_j$, and the matrices $B^{(j)}$ defined in two dimensions by

$$B^{(j)} = \begin{pmatrix} a_{11}^{(j)} - a_{22}^{(j)} & 2(a_{12}^{(j)} + a_{21}^{(j)}) \end{pmatrix} \tag{4.70}$$

and in three dimensions by

$$B^{(j)} = \begin{pmatrix} a_{23}^{(j)} & 0 & 0 & a_{22}^{(j)} - a_{33}^{(j)} & a_{12}^{(j)} & -a_{13}^{(j)} \\ 0 & -a_{13}^{(j)} & 0 & -a_{12}^{(j)} & a_{33}^{(j)} - a_{11}^{(j)} & a_{23}^{(j)} \\ 0 & 0 & a_{12}^{(j)} & a_{13}^{(j)} & -a_{23}^{(j)} & a_{11}^{(j)} - a_{22}^{(j)} \end{pmatrix}. \tag{4.71}$$

A condition in dimension $d = 2, 3$ for having ellipticity is that the $d \times d$ matrix

$$\begin{pmatrix} B^{(1)} \\ B^{(2)} \end{pmatrix} \text{ must be invertible.} \tag{4.72}$$

The equivalence between (4.68) and (4.72) comes from the equality

$$\begin{pmatrix} ((A^{(1)}\xi)\times\xi)^\intercal \\ ((A^{(1)}\xi)\times\xi)^\intercal \end{pmatrix} = \begin{pmatrix} B^{(1)} \\ B^{(2)} \end{pmatrix} \begin{pmatrix} \xi_2^2 - \xi_1^2 \\ \xi_1\xi_2 \end{pmatrix}$$

in dimension 2, and

$$\begin{pmatrix}((A^{(1)}\xi)\times\xi)^\intercal\\((A^{(1)}\xi)\times\xi)^\intercal\end{pmatrix}=\begin{pmatrix}B^{(1)}\\B^{(2)}\end{pmatrix}\begin{pmatrix}\xi_3^2-\xi_2^2\\\xi_3^2-\xi_1^2\\\xi_2^2-\xi_1^2\\\xi_2\xi_3\\\xi_1\xi_3\\\xi_1\xi_2\end{pmatrix}$$

in dimension 3. Note that condition (4.72) is a sufficient condition for $\nabla^S u_1 \neq \alpha\nabla^S u_2\ \forall\alpha\in\mathbb{R}$.

4.6.2 Lopatinskii condition

The Lopatinskii condition we show is based in [AWZ15]. The analysis is the same, but in certain step we consider the condition (4.68) instead of (4.69).
If

$$\mathcal{P}_2(x, i\eta+\nu\partial_z)(\tilde{\mu},\tilde{u})=0,$$

then we easily see that $\tilde{u}\equiv 0$, due to the identity blocks. Then, consider $A^{(j)}=\nabla^S u_j$. Then we have the equation

$$(A^{(j)}\nu\times\nu)\partial_z^2\tilde{\mu}+i(A^{(j)}\eta\times\nu+A^{(j)}\nu\times\eta)\partial_z\tilde{\mu}-(A^{(j)}\eta\times\eta)\tilde{\mu}=0,\quad j=1,2.$$

If in each equation we apply the dot product with $A^{(j)}\nu\times\nu$, and then we sum both equations, we obtain:

$$a\partial_z^2\tilde{\mu}+b\partial_z\tilde{\mu}+c\tilde{\mu}=0 \tag{4.73}$$

with

$$a=\sum_j |A^{(j)}\nu\times\nu|^2$$

which is nonzero by (4.68). Then, let $\lambda_{1,2}=\dfrac{-ib\pm\sqrt{-b^2-4ac}}{2a}$ the roots of the characteristic polynomial related to equation (4.73). The solutions have the structure

$$\tilde{\mu}(z)=\alpha(\exp(\lambda_1 z)-\exp(\lambda_2 z))$$

since $\tilde{\mu}(0)=0$. If $\lambda_{1,2}$ is purely imaginary, the only option for $\tilde{\mu}$ going to 0 when $z\to\infty$ is when $\alpha=0$. If $\lambda_{1,2}$ has a real part, then one of the exponentials goes to infinity and the other goes to zero when $z\to\infty$, so the only option we have is $\alpha=0$. That is, we have the Lopatinskii condition.

The Douglis numbers are:

$$s_i=\begin{cases}0 & \text{if } i\in\{1,\dots,d+1,2d+2,\dots,3d+1\},\\-2 & \text{otherwise,}\end{cases}$$

$$t_j=\begin{cases}2 & \text{if } i=1,\\3 & \text{otherwise,}\end{cases}$$

$$\sigma_k=-1,\quad k=1,\dots,2d.$$

Then the operator over $(\delta\mu, \{\delta u_j\}_{j=1}^J)$ given by equation (4.67) with 2 measurements is defined from

$$\mathcal{X} = H^{l+2}(\Omega) \times H^{l+3}(\Omega)^d \times H^{l+3}(\Omega)^d$$

to

$$\mathcal{Y} = \left(H^l(\Omega)^d \times H^{l+2}(\Omega)^d \times H^{l+2}(\Omega) \times H^{l+1/2}(\Omega)^d \right)^2$$

where we can take $l = 2$ in dimension 2 and dimension 3. Then we have the following estimate:

$$\begin{aligned} ||\delta\mu||_{H^{l+2}(\Omega)} + \sum_{j=1}^{2} ||\delta u_j||_{H^{l+3}(\Omega)^d} \leq C \sum_{j=1}^{2} \Big(& ||\mathcal{L}_j^{ec}(\delta\mu, \delta u_j)||_{H^l(\Omega)^d} \\ & + ||\mathcal{L}_j^{int}(\delta\mu, \delta u_j)||_{H^{l+2}(\Omega)^d} \\ & + ||\mathcal{L}_j^{div} \delta u_j||_{H^{l+2}(\Omega)} + ||\delta u_j||_{H^{l+1/2}(\partial\Omega)^d} \Big) \\ & + C_2 \Big(||\delta\mu||_{L^2(\Omega)} + \sum_{j=1}^{2} ||\delta u_j||_{L^2(\Omega)^d} \Big). \end{aligned}$$

4.6.3 Local injectivity

The results in [GW16] prove local injectivity and the convergence of an algorithm for the recovery of μ. They use unique continuation properties assuming $\delta\mu|_{\partial\Omega} = 0$ (in our notation). In this section we show another injectivity argument, based on [Bal14].

If we consider the right hand side of (4.66) being 0, then we have

$$\nabla \times \nabla \cdot \left(\delta\mu A^{(j)} \right) = 0, \quad j = 1, 2.$$

Let $\rho(x, \xi)$ be the principal symbol for this last equation. Then

$$\rho(x, \xi) = \begin{pmatrix} (A^{(1)}\xi) \times \xi \\ (A^{(2)}\xi) \times \xi \end{pmatrix}.$$

In dimension 2, we need to assume that $A_{12}^{(j)} \neq 0$ to obtain that $(0, 1)$ is non characteristic at the origin, since

$$A^{(j)} \begin{pmatrix} 0 \\ 1 \end{pmatrix} \times \begin{pmatrix} 0 \\ 1 \end{pmatrix} = A_{12}^{(j)}.$$

In dimension 3, we need to assume that $a_{13}^{(j)}, a_{23}^{(j)} \neq 0$ to obtain that $(0, 0, 1)$ is non characteristic at the origin, since

$$A^{(j)}(0, 0, 1) \times (0, 0, 1) = (a_{23}^{(j)}, -a_{13}^{(j)}, 0).$$

The condition (4.68) provides the hypothesis for Theorem 3.6 in [Bal14], since there are not real roots, and then, due to the fundamental algebra theorem, we have two different complex roots. Therefore, we have a unique continuation principle for μ and we can take $C_2 = 0$ in the last estimate above.

4.7 Nonlinear Elasticity (Saint-Venant model) with internal measurements

Saint-Venant model is the first nonlinear model in elasticity that is studied in the literature. It is a generalization of the linear model studied before, and it comes from the simplification of the Green strain tensor

$$Eu = \nabla^S u + \frac{1}{2}\nabla u^\intercal \nabla u. \tag{4.74}$$

In linear elasticity, it is assumed that the displacements are sufficiently small for neglecting the term $\nabla u^\intercal \nabla u$, considering the *small strain tensor*,

$$\epsilon u = \nabla^S u, \tag{4.75}$$

c.f. [Ogd97] for the constant coefficient calculations. The Saint Venant-Kirchhoff model considers (4.74) instead of (4.75), since it is assumed that the deformations are not so small, and Eu plays the role of ϵu in the constitutive equations of linear elasticity.
In this section, we consider the Saint-Venant's model under a periodic force with frequency ω, which can be written as a "steady state" equation by:

$$\begin{cases} (L_{\mu,\lambda} + N_{\mu,\lambda})u + \omega^2 u &= 0 \quad \text{in } \Omega, \\ u &= g \quad \text{on } \partial\Omega. \end{cases} \tag{4.76}$$

where

$$\begin{aligned} L_{\mu,\lambda}u &= 2\nabla \cdot \mu\nabla^S u + \nabla(\lambda \nabla \cdot u), \\ N_{\mu,\lambda}u &= 2c_\tau \nabla \cdot (\mu \nabla u^\intercal \nabla u) + \nabla(\lambda |\nabla u|^2). \end{aligned}$$

and c_τ is a constant in x coming from the fact that we cannot obtain a time independent equation by applying a periodic force in time, as in the previous cases, since they are linear in u. So, our model is considered for a fixed time τ.
The measurements are

$$u = H \quad \text{in } \Omega. \tag{4.77}$$

Applying the curl operator in (4.76), we obtain

$$\begin{cases} (\tilde{L}_\mu + \tilde{N}_\mu)u + \omega^2 \nabla \times u &= 0 \quad \text{in } \Omega, \\ u &= 0 \quad \text{on } \partial\Omega. \end{cases} \tag{4.78}$$

where

$$\tilde{L}_\mu u = 2\nabla \times \nabla \cdot \mu \nabla^S u, \qquad \tilde{N}_\mu u = 2c_\tau \nabla \times \nabla \cdot (\mu \nabla u^\intercal \nabla u).$$

The linearized system from (4.78) with internal measurements is

$$\begin{cases} D\tilde{L}(\mu,u)[\delta\mu,\delta u] + D\tilde{N}(\mu,u)[\delta\mu,\delta u] + \omega^2 \nabla \times \delta u &= 0 \quad \text{in } \Omega, \\ \delta u &= \delta H \quad \text{in } \Omega, \\ \delta u &= 0 \quad \text{on } \partial\Omega. \end{cases} \tag{4.79}$$

where $D\tilde{L}$ and $D\tilde{N}$ are the Fréchet derivatives of $\tilde{L}$ and $\tilde{N}$, respectively, given by:

$$\begin{aligned} D\tilde{L}(\mu,u)[\delta\mu,\delta u] &= 2\nabla \times \nabla \cdot \delta\mu \nabla^S u + 2\nabla \times \nabla \cdot \mu \nabla^S \delta u \\ D\tilde{N}(\mu,u)[\delta\mu,\delta u] &= 2c_\tau \nabla \times \nabla \cdot (\delta\mu \nabla u^\intercal \nabla u) + 2\nabla \times \nabla \cdot (\mu \nabla \delta u^\intercal \nabla u), \\ &\quad +2\nabla \times \nabla \cdot (\mu \nabla u^\intercal \nabla \delta u). \end{aligned}$$

4.7.1 Ellipticity

The symbol of the linearized operator is

$$\mathcal{P}(x,\xi) = \begin{bmatrix} 2\Big((\nabla^S u + c_\tau \nabla u^\intercal \nabla u)\xi\Big) \times \xi & P(\xi) \\ 0 & I_d \end{bmatrix}$$

where

$$P(\xi) = -2\mu\Sigma_{\text{curl}}(\xi)\Big(|\xi|^2 I_d + \xi \otimes \xi\Big)(I_d + \nabla u^\intercal).$$

We see that $Op(\mathcal{P}(x,\xi))$ is not elliptic. If we add a measurement, we will have the symbol

$$\mathcal{P}_2(x,\xi) = \begin{bmatrix} 2\Big((\nabla^S u_1 + c_\tau \nabla u_1^\intercal \nabla u_1)\xi\Big) \times \xi & P(\xi) & 0 \\ 0 & I_d & 0 \\ 2\Big((\nabla^S u_2 + c_\tau \nabla u_2^\intercal \nabla u_2)\xi\Big) \times \xi & 0 & P(\xi) \\ 0 & 0 & I_d \end{bmatrix}$$

and we see that the linearized operator is elliptic if

$$\left|\Big((\nabla^S u_1 + c_\tau \nabla u_1^\intercal \nabla u_1)\xi\Big) \times \xi\right| + \left|\Big((\nabla^S u_2 + \nabla c_\tau u_2^\intercal \nabla u_2)\xi\Big) \times \xi\right| \neq 0 \quad \forall \xi \neq 0.$$

Let $A^{(j)} = \nabla^S u_j + c_\tau \nabla u_j^\intercal \nabla u_j$, and and the matrices $B^{(j)}$ defined as in (4.70)-(4.71). Then a condition for having ellipticity is (4.72).

4.7.2 Lopatinskii condition and local injectivity

The deduction of the Lopatinskii condition and local injectivity are the same as the presented in section 4.6, with the change

$$A^{(j)} = \nabla^S u_j + c_\tau \nabla u_j^\intercal \nabla u_j, \quad j = 1, 2.$$

The Douglis numbers are:

$$s_i = \begin{cases} 0 & \text{if } i \in \{1, \dots, d, 2d+1, \dots, 3d\}, \\ -2 & \text{otherwise,} \end{cases}$$

$$t_j = \begin{cases} 2 & \text{if } i = 1, \\ 3 & \text{otherwise} \end{cases}$$

$$\sigma_k = -1, \quad k = 1, \dots, 2d.$$

Then the operator over $(\delta\mu, \{\delta u_j\}_{j=1}^J)$ given by equation (4.79) with 2 measurements is defined from

$$\mathcal{X} = H^{l+2}(\Omega) \times H^{l+3}(\Omega)^d \times H^{l+3}(\Omega)^d$$

to

$$\mathcal{Y} = \Big(H^l(\Omega)^d \times H^{l+2}(\Omega)^d \times H^{l+1/2}(\Omega)^d\Big)^2$$

with $l = 2$ in dimension 2 and 3. Then we have the following estimate:

$$\begin{aligned}||\delta\mu||_{H^{l+2}(\Omega)}+\sum_{j=1}^{2}||\delta u_j||_{H^{l+3}(\Omega)^d} \leq \; & C\sum_{j=1}^{2}\Big(||\mathcal{L}_j^{ec}(\delta\mu,\delta u_j)||_{H^l(\Omega)^d} \\ & +||\mathcal{L}_j^{int}(\delta\mu,\delta u_j)||_{H^{l+2}(\Omega)^d}+||\delta u_j||_{H^{l+\frac{1}{2}}(\partial\Omega)^d}\Big) \\ & +C_2\Big(||\delta\mu||_{L^2(\Omega)}+\sum_{j=1}^{2}||\delta u_j||_{L^2(\Omega)^d}\Big).\end{aligned}$$

Since we have local injectivity, we can take $C_2 = 0$. That is, we have

$$\begin{aligned}||\delta\mu||_{H^{l+2}(\Omega)}+\sum_{j=1}^{2}||\delta u_j||_{H^{l+3}(\Omega)^d} \leq \; & C\sum_{j=1}^{2}\Big(||\mathcal{L}_j^{ec}(\delta\mu,\delta u_j)||_{H^l(\Omega)^d} \\ & +||\mathcal{L}_j^{int}(\delta\mu,\delta u_j)||_{H^{l+2}(\Omega)^d}+||\delta u_j||_{H^{l+\frac{1}{2}}(\partial\Omega)^d}\Big).\end{aligned} \tag{4.80}$$

4.7.3 Algorithm

We define μ_0 as our first guess for μ and u_0 a solution of the equation (4.78) corresponding to $\mu = \mu_0$. Let $\delta\hat{u}$ be the displacement satisfying $H = u_0+\delta\hat{u}$, and $\delta\mu_{tr}$ such that $\mu_{tr} = \mu_0+\delta\mu_{tr}$.

In order to reconstruct μ_{tr} from the measurements H, we define the discrepancy functional:

$$\mathcal{J}[\delta\mu] = \mathcal{J}_1[\delta\mu] + \mathcal{J}_2[\delta\mu] = \frac{1}{2}\Big(||P_1[\delta\mu]-\delta\hat{u}_1||^2_{X_u} + ||P_2[\delta\mu]-\delta\hat{u}_2||^2_{X_u}\Big)$$

where P_j is the operator given by $P_j : \delta\mu \mapsto \delta u_j$ defined by equation (4.79) and $X_u = H^{l+3}(\Omega)^d$. Our strategy for determining μ from $\{H_1, H_2\}$ is to solve the problem

$$\min_{\delta\mu\in X_\mu}\mathcal{J}[\delta\mu]$$

where $X_\mu = H^{l+2}(\Omega)$.

Following [AWZ15], we consider the following iterations

$$\left\{\begin{array}{rcl}\delta\mu_{n+1} &=& \delta\mu_n - \eta D\mathcal{J}[\delta\mu_n], \\ \delta\mu_0 &=& 0.\end{array}\right. \tag{4.81}$$

For each α multi-index of dimension d satisfying $|\alpha| \leq l+3$, let $\psi_j^\alpha = \dfrac{\partial^{|\alpha|}P_j[\delta\mu]}{\partial x^\alpha}$, $\psi_{j,tr}^\alpha = \dfrac{\partial^{|\alpha|}\delta\hat{u}_j}{\partial x^\alpha}$ and the functionals:

$$\mathcal{J}_j^\alpha[\delta\mu] = \frac{1}{2}||\psi_j^\alpha - \psi_{j,tr}^\alpha||^2_{L^2(\Omega)^d},$$

The derivative of $\mathcal{J}_j^\alpha$ can be written

$$D\mathcal{J}_j^\alpha[\delta\mu] = \Big(\frac{\partial^{|\alpha|}}{\partial x^\alpha}DP_j[\delta\mu]\Big)^*\Big(\frac{\partial^{|\alpha|}}{\partial x^\alpha}P_j[\delta\mu] - \frac{\partial^{|\alpha|}}{\partial x^\alpha}P_j[\delta\mu_{tr}]\Big). \tag{4.82}$$

This expression allows to conclude that the algorithm given by (4.81) converges (see [AWZ15] Theorem 6) when (4.80) holds and the initial guess μ_0 is close enough to μ.

On the other hand we need to determine each $D\mathcal{J}_j^\alpha[\delta\mu]$ in a more explicit form.

Lemma 4.16. *Let ϕ_j^α be a solution of the following adjoint system:*

$$\begin{cases} 2\nabla\cdot\Big[\Big(\delta\mu(I_d+2c_\tau\nabla u_j)+2c_\tau\mu\nabla\delta u_j\Big)\nabla^S(\nabla\times\phi_j^\alpha)\Big] = \psi_j^\alpha-\psi_{j,tr}^\alpha & \text{in } \Omega,\\ \nabla^S(\nabla\times\phi_j^\alpha) = 0 & \text{on } \partial\Omega,\\ \nabla\times\phi_j^\alpha = 0 & \text{on } \partial\Omega,\\ \phi_j^\alpha = 0 & \text{on } \partial\Omega, \end{cases} \tag{4.83}$$

Then, the Fréchet-derivative of $\mathcal{J}_j^\alpha$ is given by:

$$D\mathcal{J}_j^\alpha[\delta\mu] = 2\Big[\nabla^S\delta u_j + c_\tau\Big((\nabla\delta u_j^\intercal\nabla u_j)+(\nabla\delta u_j^\intercal\nabla u_j)^\intercal\Big)\Big]:\nabla^S(\nabla\times\phi_j^\alpha).$$

Proof. We compute the second order derivatives of $\tilde{L}$ and $\tilde{N}$:

$$\begin{aligned} D^2\tilde{L}(\mu,u_j)[\delta\mu,\delta u_j;\gamma,w] &= 2\nabla\times\nabla\cdot(\delta\mu\nabla^S w)+\omega^2\nabla\times w\\ &\quad +2\nabla\times\nabla\cdot\gamma\nabla^S\delta u_j,\\ D^2\tilde{N}(\mu,u_j)[\delta\mu,\delta u_j;\gamma,w] &= 2c_\tau\nabla\times\nabla\cdot\Big(\delta\mu(\nabla w^\intercal\nabla u_j+\nabla u_j^\intercal\nabla w)\\ &\quad +\mu(\nabla\delta u_j^\intercal\nabla w+\nabla w^\intercal\nabla\delta u_j)\Big)\\ &\quad +2c_\tau\nabla\times\nabla\cdot\Big(\gamma(\nabla\delta u_j^\intercal\nabla u_j+\nabla u_j^\intercal\nabla\delta u_j)\Big). \end{aligned}$$

We have, using the adjoint equation and integrating by parts:

$$\begin{aligned} &\int_\Omega(\psi_j^\alpha-\psi_{j,tr}^\alpha)\cdot w dx\\ &=\int_\Omega 2\nabla\cdot\Big[\Big(\delta\mu(I_d+2c_\tau\nabla u_j)+2c_\tau\mu\nabla\delta u_j\Big)\nabla^S(\nabla\times\phi_j^\alpha)\Big]\cdot w\,dx\\ &=\int_\Omega\nabla\times\Big[\Big(2\nabla\cdot\delta\mu\nabla^S w+\omega^2 w\Big)+2c_\tau\Big(\delta\mu(\nabla w^\intercal\nabla u_j+\nabla u_j^\intercal\nabla w)\\ &\qquad +\mu(\nabla\delta u_j^\intercal\nabla w+\nabla w^\intercal\nabla\delta u_j)\Big)\Big]\cdot\phi_j^\alpha dx\\ &=-\int_\Omega\Big[2\nabla\times\nabla\cdot\gamma\Big(\nabla^S\delta u_j+c_\tau(\nabla\delta u_j^\intercal\nabla u_j+\nabla u_j^\intercal\nabla\delta u_j)\Big)\Big]\cdot\phi_j^\alpha dx \end{aligned}$$

where in the last step we used the computation of the second order derivative of $\tilde{L}+\tilde{N}$ and that

$$D^2(\tilde{L}+\tilde{N})(\mu,u_j)[\delta\mu,\delta u_j;\gamma,w]=0.$$

Finally, using (4.82), integrating by parts and considering $w = \gamma \dfrac{\partial^\alpha}{\partial x^\alpha} DP_j[\delta\mu]$, we have:

$$\begin{aligned} D\mathcal{J}_j^\alpha[\delta\mu]\gamma &= \int_\Omega (\psi_j^\alpha - \psi_{j,tr}^\alpha) \cdot w \; dx \\ &= \int_\Omega \gamma \Big[2\Big(\nabla^S \delta u + c_\tau (\nabla \delta u^\intercal \nabla u + \nabla u^\intercal \nabla \delta u) \Big) : \nabla^S (\nabla \times \phi_j^\alpha) \Big] dx. \end{aligned}$$

Therefore,

$$D\mathcal{J}_j^\alpha[\delta\mu] = 2\Big(\nabla^S \delta u + c_\tau (\nabla \delta u^\intercal \nabla u + \nabla u^\intercal \nabla \delta u) \Big) : \nabla^S (\nabla \times \phi_j^\alpha).$$

□

Chapter 5

Conclusion

5.1 Conclusion

In chapter 2 we have presented a robust method for estimating velocities from dual-VENC data by PC-MRI. We presented a theoretical analysis of the phase contrast MRI technique under the approach of least squares functionals and under this comprehension we gave a new idea for a more robust and less noisy estimation of the velocity, involving three measurements. We also presented an empirical analysis by making measurements for a phantom and for volunteers. We reconstructed velocities for different combinations of VENCs, and we propose some convenient combinations for the two VENCs used, such that in practice it would be necessary to choose only one of the VENCs. The reconstruction algorithm is relatively simple and it could be implemented by MRI scanners.

The method proposed has the potential of changing the protocols in PC-MRI, since we change from the need of scanning with $|u_{true}| \leq$ VENC, which is in general not known a priori to hold, to scan with high-VENC satisfying $|u_{true}| \leq 3$VENC, which augment the chance to obtain aliasing-free images at the first try.

In chapter 3 we have presented the extension of ODV in the case of the recovery of harmonic displacements by PC-MRI and we showed a practical analysis for certain types of waveforms. We presented the extension for measurements which can lead us to a discrete Fourier transform in time as well. Therefore we presented useful measurements for obtaining the input of different problems in elastography.

In chapter 4 we studied some hybrid inverse problems in elasticity. We focused on time-independent equations in the displacement field, which is a vector-valued solution. We analyzed ellipticity conditions of the PDE problem augmented with interior data: power density measurements and the internal displacements. Since our information is internal, we obtained better stability estimates than boundary value inverse problems.

The inverse problem of linear elasticity with power density measurements was studied in dimension two with the additional knowledge of the pressure, because there is no ellipticity, according to Definition 4.1, in the case of unknown pressure. We obtained ellipticity for two measurements under certain conditions over the small strain tensors which seem natural to impose, and a trivial kernel if in addition we impose a lower bound for the frequency ω. We showed the convergence of a reconstruction algorithm for the recovery of μ. We also applied the techniques applied for this inverse problem in the study of the recovery of μ if the equation has a nonlinear forcing term, which is a differential operator of order at most

one. This work is an extension of [Bal14] to the case of elasticity, which is not present in the literature, and using different techniques in computations.

The inverse problem of Saint-Venant elasticity model with internal measurements was studied for dimension two and three. We showed ellipticity for two measurements under certain conditions over the strain tensors. We also obtained a trivial kernel without imposing any condition over the frequency ω, which is a good result if we place this problem in the context of the low hencs in MRE. We finally proposed an algorithm for the reconstruction of μ based in the obtained stability estimates. This work can be seen as an extension of [AWZ15] to the case of the Saint-Venant model.

5.2 Perspectives

The ODV idea certainly has questions to explore about, for example, the possibility of adaptation to, for example, 4D-flow [Sta+14] and displacement encoding with stimulated echoes (DEnSE) [Ale+99].

The ODV technique can be explored in cases of high variability of the recovered parameter, since it is a non-smoothing technique as the other techniques found in the literature. Finally, it would be interesting to combine ODV with other approaches in inverse problems in imaging, for example compressed sensing [Lus+08], in order to accelerate acquisitions or coupling the recovered parameter with a physical model in order to denoise the recovery.

The power density measurements is an example of nonlinear model of measurements in hybrid inverse problems and it is open to study other nonlinear models, for example with any arbitrary power over the norm of the small strain tensor, analogue to [Bal13]. In addition, reasonable extensions are to obtain analog results in dimension three and to assume that the pressure is unknown.

About the nonlinear models of elasticity, it would be interesting to extend the study of the inverse problem for the Saint Venant model to another models, for example the Neo-Hookean model.

In real applications, the functions involved in the models of hybrid inverse problems could be not as smooth as we assume them. Hence, it would be useful to reduce the regularity in the estimates obtained in this work. In addition, the studied problems are time-independent. A possible future work is to study the time-dependent case, which would increase the number of potential applications to other modalities of elasticity imaging.

Finally, it would be interesting to implement the proposed algorithms in hybrid inverse problems, verifying the convergence in reasonable times. This would be an important step for showing the applicability of this work.

Appendix A

Summary

In this thesis we present a study of inverse problems and methods for the reconstruction of the following parameters of interest: the velocity of blood in vessels via MRI, the displacements of tissues under a harmonic regime via MRI, and the shear modulus from different models of hybrid imaging: linear elasticity with internal measurements of elastic energy density (power density), and the (nonlinear) Saint-Venant model of elasticity with internal measurements of the displacement field.

In Chapter 1 an introduction is presented giving a context in previous theory and applications. The main motivation comes from medical imaging, where MRI and elastography are prominent examples.

In Chapter 2 we present a robust method for estimating velocities from dual-VENC data by PC-MRI. We present a theoretical analysis of the phase contrast MRI technique using the approach of least squares functionals and under this comprehension we propose a new idea for a more robust and less noisy estimation of the velocity, involving three measurements. We also present an empirical analysis by making measurements for a phantom and for volunteers. We reconstruct velocities for different combinations of VENCs, and we propose some convenient combinations for the two VENCs used, such that in practice it would be necessary to choose only one of the VENCs. The reconstruction algorithm is relatively simple and it could be implemented in MRI scanners. The proposed method has the potential of changing the protocols in PC-MRI, since we change from the need of scanning such that the true velocity is less than the VENC, which is in general not known a priori to hold, to scan with high-VENC being less than the true velocity, even being the third part of it, which augment the chance to obtain aliasing-free images at the first try.

In Chapter 3 we present the extension of ODV to the case of the recovery of harmonic displacements by PC-MRI and we show a practical analysis for certain types of waveforms. We present the extension for measurements which can lead us to a discrete Fourier transform in time as well. Therefore we present useful measurements for obtaining the input of different problems in elastography.

In Chapter 4 we study some hybrid inverse problems in elasticity. We focus on time-independent equations in the displacement field, which is a vector-valued solution. We analyze ellipticity conditions of the PDE problem augmented with interior data: power density measurements and the internal displacements. Since our information is internal, we obtain better stability estimates than boundary value inverse problems.

The inverse problem of linear elasticity with power density measurements is studied in

dimension two with the additional knowledge of the pressure, because there is no ellipticity, in the case of unknown pressure. We obtain ellipticity for two measurements under certain conditions over the small strain tensors which seem natural to impose, and a trivial kernel if in addition we impose a lower bound for the mechanical frequency. We show the convergence of a reconstruction algorithm for the recovery of the shear modulus. We also apply the techniques applied for this inverse problem in the study of the recovery of the shear modulus if the equation has a nonlinear forcing term, which is a differential operator of order at most one.

The inverse problem of Saint-Venant elasticity model with internal measurements is studied for dimension two and three. We show ellipticity for two measurements under certain conditions over the strain tensors. We also obtain a trivial kernel without imposing any condition on the mechanical frequency, which is a good result if we place this problem in the context of the low HENCs in MRE. We finally propose an algorithm for the reconstruction of the shear modulus based on the obtained stability estimates.

Samenvatting

In dit proefschrift presenteren we een studie van inverse problemen en methoden voor de reconstructie van de volgende interessante parameters: de snelheid van bloed in bloedvaten via MRI, de verplaatsingen van weefsels onder een harmonisch regime via MRI en de afschuifmodulus van verschillende elasticiteitsmodellen van hybride beeldvorming: lineaire elasticiteit met interne metingen van elastische energiedichtheid (vermogensdichtheid), en het (niet-lineaire) Saint-Venant elasticiteitsmodel met interne metingen van het verplaatsingsveld.

In Hoofdstuk 1 presenteren we een inleiding die een context biedt voor eerdere theorieën en toepassingen. De belangrijkste motivatie komt van medische beeldvorming, met MRI en elastografie als prominente voorbeelden.

In Hoofdstuk 2 presenteren we een robuuste methode voor het schatten van snelheden op basis van dual-VENC-gegevens met behulp van PC-MRI. We presenteren een theoretische analyse van de fasecontrast-MRI-techniek onder de kleinste kwadraten benadering en daarmee introduceren we een nieuw idee voor een robuustere en minder ruisende schatting van de snelheid, met drie metingen. We hebben ook een empirische analyse gepresenteerd door metingen te doen met een fantoom en met vrijwilligers. We hebben de snelheden voor verschillende combinaties van VENC's gereconstrueerd en we stellen enkele gunstige combinaties voor de twee gebruikte VENC's voor, zodat het in de praktijk nodig zou zijn om slechts één van de VENC's te kiezen. Het reconstructie-algoritme is relatief eenvoudig en kan worden geïmplementeerd in MRI-scanners. Onze methode heeft mogelijk als gevolg dat protocollen in PC-MRI gewijzigd zullen worden. Huidige methodes hebben namelijk meerdere metingen nodig om er voor te zorgen dat de ware snelheid kleiner is dan de VENC. Voor onze methode is het slechts nodig dat de hoge-VENC minstens een derde is van de ware snelheid. Dit vergroot de kans op een aliasing-vrije afbeelding bij de eerste poging.

In Hoofdstuk 3 presenteren we de uitbreiding van ODV in het geval van het bepalen van harmonische verplaatsingen door PC-MRI en we laten een praktische analyse zien voor bepaalde soorten golven. Ook introduceren we een uitbreiding voor metingen die tot een discrete Fourier-transformatie in de tijd kunnen leiden. Daarom hebben we bruikbare metingen gepresenteerd voor het verkrijgen van de input van verschillende problemen in elastografie.

In Hoofdstuk 4 bestuderen we enkele hybride inverse problemen in elasticiteit. We hebben ons gericht op tijdonafhankelijke vergelijkingen in het verplaatsingsveld, die een vectorwaardige oplossing hebben. We analyseren condities voor ellipticiteit van het PDE-probleem aangevuld met interne gegevens: vermogensdichtheidsmetingen en interne verplaatsingen. Omdat onze informatie intern is, hebben we betere stabiliteitsschattingen verkregen dan inverse problemen gebaseerd op grenswaarden. Het inverse probleem van lineaire elasticiteit met vermogensdichtheidsmetingen is bestudeerd in twee dimensies met de aanvullende kennis van de druk, omdat er geen ellipticiteit is in het geval van onbekende druk. We verkrijgen ellipticiteit voor twee metingen onder bepaalde natuurlijke condities op de kleine spanning-

stensoren, en een triviale kern als we ook een ondergrens voor de mechanische frequentie opleggen. We hebben de convergentie aangetoond van een reconstructie-algoritme voor het bepalen van de afschuifmodulus. We hebben de technieken voor dit omgekeerde probleem ook toegepast in de studie van afschuifmodulusherstel als de vergelijking een niet-lineaire forceringsterm heeft, die hoogstens een differentiële operator van orde één is.

Het inverse probleem van het Saint-Venant-elasticiteitsmodel met interne metingen is bestudeerd voor twee en drie ruimtelijke dimensies. We laten ellipticiteit zien voor twee metingen onder bepaalde omstandigheden over de spanningstensoren. We verkrijgen ook een triviale kern zonder enige voorwaarde te stellen aan de mechanische frequentie, wat een goed resultaat is als we dit probleem in de context van de lage HENC's in MRE plaatsen. We stellen uiteindelijk een algoritme voor die de reconstructie van de afschuifmodulus op basis van de verkregen stabiliteitsschattingen mogelijk maakt.

Resumen

En esta tesis presentamos un estudio de problemas inversos y métodos para la reconstrucción de los siguientes parámetros de interés: la velocidad sanguínea en los vasos vía imágenes de resonancia magnética (MRI), el desplazamiento de tejidos bajo un régimen armónico vía MRI, y el módulo de corte a partir de distintos modelos híbridos de imágenes: elasticidad lineal con mediciones internas de densidad de energía (o densidad de potencia) elástica, y el modelo de elasticidad (no-lineal) de Saint-Venant con mediciones internas del campo de desplazamientos.

En el Capítulo 1, se presenta una introducción dando un contexto en teoría previa y aplicaciones. La mayor motivación viene de las imágenes médicas, donde MRI y la elastografía son ejemplos prominentes.

En el Capítulo 2 presentamos un método robusto para la estimación de velocidades a partir de datos de dual-VENC en MRI. Presentamos un análisis teórico de la técnica de contraste de fase (PC-MRI) bajo el enfoque de funcionales de mínimos cuadrados y bajo esta comprensión proporcionamos una nueva idea para una estimación más robusta y menos ruidosa de la velocidad, involucrando tres mediciones. Además presentamos un análisis empírico mediante mediciones en un fantoma y voluntarios. Reconstruimos velocidades para distintas combinaciones de VENCs, y proponemos algunas combinaciones convenientes para los dos VENCs usados, tal que en la práctica sería necesario escoger sólo uno de los VENCs. El algoritmo de reconstrucción es relativamente simple y podría ser implementado por escáneres de resonancia magnética. El método propuesto tiene el potencial de cambiar los protocolos en PC-MRI, ya que cambiamos desde la necesidad de escanear tal que la velocidad real sea menor que el VENC, lo cual, en general, no se sabe si se cumple a priori, a escanear con un VENC alto siendo menor que la velocidad real, incluso siendo la tercera parte, lo cual aumenta las posibilidades de obtener imágenes libres de *aliasing* en el primer intento.

En el Capítulo 3, presentamos la extensión de la técnica ODV al caso de la recuperación de desplazamientos armónicos vía PC-MRI y mostramos un análisis práctico para ciertos tipos de *waveforms*. Además, presentamos la extensión para mediciones que pueden conducirnos a una transformada de Fourier discreta en tiempo. Por lo tanto, presentamos mediciones útiles para la obtención de un input de diferentes problemas en elastografía.

En el Capítulo 4, estudiamos algunos problemas inversos híbridos en elasticidad. Nos enfocamos en ecuaciones independientes del tiempo del campo de desplazamientos, el cual es una solución a valores vectoriales. Analizamos condiciones de elipticidad para el problema de EDP aumentado con datos interiores: mediciones de densidad de potencia y mediciones internas de desplazamientos. Como nuestra información es interna, obtenemos estimaciones de estabilidad mejores que en problemas inversos de valores de frontera.

El problema inverso de elasticidad lineal con mediciones de densidad de potencia es estudiado en dimensión dos con el conocimiento adicional de la presión, ya que no hay elipticidad

en el caso de presión desconocida. Obtenemos elipticidad para dos mediciones bajo ciertas condiciones sobre los tensores de estrés, las cuales parecen ser naturales de imponer, y además obtenemos un *kernel* trivial si además imponemos una cota inferior para la frecuencia mecánica. Mostramos la convergencia de un algoritmo de reconstrucción para el módulo de corte. Además aplicamos las técnicas usadas para este problema inverso en el estudio de la recuperación del módulo de corte en el caso en que la ecuación además tiene un término forzante, el cual es un operador diferencial de orden a lo más uno.

El problema inverso en el modelo de elasticidad de Saint-Venant con mediciones internas es estudiado para dimensión dos y tres. Mostramos la elipticidad para dos mediciones bajo ciertas condiciones sobre los tensores de corte. Además obtenemos un kernel trivial sin imponer ninguna condición sobre la frecuencia mecánica, el cual es un buen resultado si contextualizamos este problema en HENCs bajos en MRE. Finalmente, proponemos un algoritmo para la reconstrucción del módulo de corte basado en las estimaciones de estabilidad obtenidas.

Propositions

1. In dual-VENC technique it is necessary to measure three times, that is, three different velocity encoding magnetic gradients, instead of classical PC-MRI, where the number of measurements is two.

2. Thanks to the additional measurement, the effective VENC increases if both VENCs are chosen appropriately, for instance by a factor of three if the ratio between low and high VENCs is 3/4.

3. The dual-VENC method can be performed by the scanner if it is programmed properly and the high VENC is set, that is, the scanner can perform the choice of the low VENC, the search interval and the minimization. Therefore, it is not necessary any user intervention.

4. It is possible to recover uniquely and in a stable way the shear modulus in a two dimensional harmonic linear elasticity model with two sets of internal power density measurements, if the pressure from the Stokes approximation is given and the mechanical frequency is sufficiently large.

5. It is possible to recover uniquely and in a stable way the shear modulus in a two or three dimensional harmonic Saint-Venant elasticity model with two sets of internal displacement measurements.

6. Stability estimates for the shear modulus in the studied elasticity and measurements models allow to conclude the convergence of reconstruction algorithms for this parameter, provided the initial guess is close enough to the solution.

Curriculum vitae

Hugo Carrillo has born on October 30, 1989 in Angol, Región de la Araucanía, Chile. In 2007, he completed his secondary education at the Instituto Nacional José Miguel Carrera in Santiago, Chile. He holds the Bachelor of Engineering Sciences, mention in Mathematics in 2014 and the professional title of Civil Engineer in Mathematics in 2016, both from University of Chile. His engineering thesis has the title "Study of the T2 decay in MRI and a correction for the partial volume artifact", work performed under the supervision of Prof. Dr. Carlos Conca (University of Chile), and co-supervision of Dr. Raúl Gormaz (University of Chile) and Dr. Hernan Jara (University of Boston). He was awarded a PhD scholarship of the Chilean governmental research institution CONICYT. In 2018 he started a stay in Groningen, The Netherlands, to pursue a double degree with the University of Groningen. Hugo's supervisors are Prof. Dr. A. Osses (University of Chile) and Prof. Dr. R.W.C.P Verstappen (University of Groningen). Dr. C. Bertoglio and Dr. Alden Waters (both from University of Groningen) acted as daily co-supervisors. Before his stay in Groningen, Hugo visited the Laboratory MAP5 at Paris Descartes University under the supervision of Dr. Maya de Buhan (Paris V). During his PhD, Hugo has worked as lecturer at University of Chile, Andrés Bello National University and San Sebastián University.

Bibliography

[Abr61] A. Abragam. *The Principles of Nuclear Magnetism*. International Series of Monographs **32**. Oxford University Press, 1961.

[ADN59] S. Agmon, A. Douglis, and L. Nirenberg. "Estimates near the boundary for solutions of elliptic partial differential equations satisfying general boundary conditions. I". In: *Communications on pure and applied mathematics* 12.4 (1959), pp. 623–727.

[Ale+99] A. H. Aletras, S. Ding, R. S. Balaban, and H. Wen. "DENSE: displacement encoding with stimulated echoes in cardiac functional MRI". In: *Journal of magnetic resonance (San Diego, Calif.: 1997)* 137.1 (1999), p. 247.

[Amm+08] H. Ammari, P. Garapon, H. Kang, and H. Lee. "A method of biological tissues elasticity reconstruction using magnetic resonance elastography measurements". In: *Quarterly of Applied Mathematics* 66.1 (2008), pp. 139–175.

[Amm+13] H. Ammari, H. Kang, K. Kim, and H. Lee. "Strong convergence of the solutions of the linear elasticity and uniformity of asymptotic expansions in the presence of small inclusions". In: *Journal of Differential Equations* 254.12 (2013), pp. 4446–4464.

[Amm+15] H. Ammari, E. Bretin, J. Garnier, H. Kang, H. Lee, and A. Wahab. *Mathematical methods in elasticity imaging*. Vol. 52. Princeton University Press, 2015.

[Amm08] H. Ammari. *An introduction to mathematics of emerging biomedical imaging*. Vol. 62. Springer, 2008.

[AWZ15] H. Ammari, A. Waters, and H. Zhang. "Stability analysis for magnetic resonance elastography". In: *Journal of Mathematical Analysis and Applications* 430.2 (2015), pp. 919–931.

[Bal+11] G. Bal, E. Bonnetier, F. Monard, and F. Triki. "Inverse diffusion from knowledge of power densities". In: *arXiv preprint arXiv:1110.4577* (2011).

[Bal+14] G. Bal, C. Bellis, S. Imperiale, and F. Monard. "Reconstruction of constitutive parameters in isotropic linear elasticity from noisy full-field measurements". In: *Inverse problems* 30.12 (2014), p. 125004.

[Bal13] G. Bal. "Hybrid inverse problems and internal functionals". In: *Inverse problems and applications: inside out. II* 60 (2013), pp. 325–368.

[Bal14] G. Bal. "Hybrid inverse problems and redundant systems of partial differential equations". In: *Inverse problems and applications* 615 (2014), pp. 15–48.

[Bar+15] E. Barnhill, P. Kennedy, C. L. Johnson, M. Mada, and N. Roberts. "Real-time 4D phase unwrapping applied to magnetic resonance elastography". In: *Magnetic resonance in medicine* 73.6 (2015), pp. 2321–2331.

[Ber+18] C. Bertoglio, R. Núnez, F. Galarce, D. Nordsletten, and A. Osses. "Relative pressure estimation from velocity measurements in blood flows: State-of-the-art and new approaches". In: *International Journal for Numerical Methods in Biomedical Engineering* 34.2 (2018), e2925.

[Ber+94] M. Bernstein, M. Grgic, T. Brosnan, and N. Pelc. "Reconstructions of phase contrast, phased array multicoil data". In: *Magnetic resonance in medicine* 32.3 (1994), pp. 330–334.

[Blo46] F. Bloch. "Nuclear induction". In: *Physical Review* 70.7-8 (1946), p. 460.

[BMU15] G. Bal, F. Monard, and G. Uhlmann. "Reconstruction of a fully anisotropic elasticity tensor from knowledge of displacement fields". In: *SIAM Journal on Applied Mathematics* 75.5 (2015), pp. 2214–2231.

[Bro+14] R. W. Brown, Y.-C. N. Cheng, E. M. Haacke, M. R. Thompson, and R. Venkatesan. *Magnetic Resonance Imaging: Physical Principles and Sequence Design*. John Wiley & Sons, 2014.

[BSP92] M. A. Bernstein, A. Shimakawa, and N. J. Pelc. "Minimizing TE in moment-nulled or flow-encoded two-and three-dimensional gradient-echo imaging". In: *Journal of Magnetic Resonance Imaging* 2.5 (1992), pp. 583–588.

[Cal+16] F. Callaghan, R. Kozor, A. Sherrah, M. Vallely, D. Celermajer, G. Figtree, and S. Grieve. "Use of multi-velocity encoding 4D flow MRI to improve quantification of flow patterns in the aorta". In: *Journal of Magnetic Resonance Imaging* 43.2 (2016), pp. 352–363.

[Car+18] H. Carrillo, A. Osses, S. Uribe, and C. Bertoglio. "Optimal Dual-VENC Unwrapping in Phase-Contrast MRI". In: *IEEE transactions on medical imaging* 38.5 (2018), pp. 1263–1270.

[Cia88] P. G. Ciarlet. *Mathematical Elasticity: Volume I: three-dimensional elasticity*. North-Holland, 1988.

[CJ05] K. J. Chang and H. Jara. "Applications of quantitative T1, T2, and proton density to diagnosis." In: *Applied radiology* 34 (2005).

[DN55] A. Douglis and L. Nirenberg. "Interior estimates for elliptic systems of partial differential equations". In: *Communications on Pure and Applied Mathematics* 8.4 (1955), pp. 503–538.

[Dyv+15] P. Dyverfeldt, M. Bissell, A. J. Barker, A. F. Bolger, C.-J. Carlhäll, T. Ebbers, C. J. Francios, A. Frydrychowicz, J. Geiger, D. Giese, M. Hope, P. Kilner, S. Kozerke, S. Myerson, S. Neubauer, O. Wieben, and M. Markl. "4D flow cardiovascular magnetic resonance consensus statement". In: *Journal of Cardiovascular Magnetic Resonance* 17 (2015), p. 72.

[Esk11] G. Eskin. *Lectures on linear partial differential equations*. Vol. 123. American Mathematical Soc., 2011.

[Fly97] T. J. Flynn. "Two-dimensional phase unwrapping with minimum weighted discontinuity". In: *JOSA A* 14.10 (1997), pp. 2692–2701.

[Gao+14] H. Gao, X. Ma, N. Qi, C. Berry, B. E. Griffith, and X. Luo. "A finite strain nonlinear human mitral valve model with fluid-structure interaction". In: *International journal for numerical methods in biomedical engineering* 30.12 (2014), pp. 1597–1613.

[GFI03] J. F. Greenleaf, M. Fatemi, and M. Insana. "Selected methods for imaging elastic properties of biological tissues". In: *Annual review of biomedical engineering* 5.1 (2003), pp. 57–78.

[GME12] K. J. Glaser, A. Manduca, and R. L. Ehman. "Review of MR elastography applications and recent developments". In: *Journal of Magnetic Resonance Imaging* 36.4 (2012), pp. 757–774.

[GP98] D. C. Ghiglia and M. D. Pritt. *Two-dimensional phase unwrapping: theory, algorithms, and software*. Vol. 4. Wiley New York, 1998.

[GW16] H. Gimperlein and A. Waters. "Stability analysis in magnetic resonance elastography II". In: *Journal of Mathematical Analysis and Applications* 434.2 (2016), pp. 1801–1812.

[Ha+16] H. Ha, G. B. Kim, J. Kweon, Y.-H. Kim, N. Kim, D. H. Yang, and S. J. Lee. "Multi-VENC acquisition of four-dimensional phase-contrast MRI to improve precision of velocity field measurement". In: *Magnetic resonance in medicine* 75.5 (2016), pp. 1909–1919.

[HSB17] S. Hirsch, I. Sack, and J. Braun. *Magnetic resonance elastography: physical background and medical applications*. John Wiley & Sons, 2017.

[Hub+18] S. Hubmer, E. Sherina, A. Neubauer, and O. Scherzer. "Lamé parameter estimation from static displacement field measurements in the framework of nonlinear inverse problems". In: *SIAM Journal on Imaging Sciences* 11.2 (2018), pp. 1268–1293.

[Ito82] K. Itoh. "Analysis of the phase unwrapping algorithm". In: *Applied optics* 21.14 (1982), pp. 2470–2470.

[JBP+05] A. Jackson, D. L. Buckley, G. J. Parker, et al. *Dynamic contrast-enhanced magnetic resonance imaging in oncology*. Springer, 2005.

[JSD15] S. Jeught, J. Sijbers, and J. Dirckx. "Fast Fourier-based phase unwrapping on the graphics processing unit in real-time imaging applications". In: *Journal of Imaging* 1.1 (2015), pp. 31–44.

[KJH18] R. Y. Kwong, M. Jerosch-Herold, and B. Heydari. *Cardiovascular magnetic resonance imaging*. Springer, 2018.

[KK08] P. Kuchment and L. Kunyansky. "Mathematics of thermoacoustic tomography". In: *European Journal of Applied Mathematics* 19.2 (2008), pp. 191–224.

[KS12] P. Kuchment and D. Steinhauer. "Stabilizing inverse problems by internal data". In: *Inverse Problems* 28.8 (2012), p. 084007.

[Lau+73] P. C. Lauterbur et al. "Image formation by induced local interactions: examples employing nuclear magnetic resonance". In: (1973).

[LE17] M. Loecher and D. Ennis. "Velocity reconstruction with nonconvex optimization for low-velocity-encoding phase-contrast MRI". In: *Magnetic resonance in medicine* (2017).

[Loe+16] M. Loecher, E. Schrauben, K. Johnson, and O. Wieben. "Phase unwrapping in 4D MR flow with a 4D single-step laplacian algorithm". In: *Journal of Magnetic Resonance Imaging* 43.4 (2016), pp. 833–842.

[LPP95] A. Lee, B. Pike, and N. Pelc. "Three-Point Phase-Contrast Velocity Measurements with Increased Velocity-to-Noise Ratio". In: *Magnetic Resonance in Medicine* 33 (1995), pp. 122–128.

[Lus+08] M. Lustig, D. L. Donoho, J. M. Santos, and J. M. Pauly. "Compressed sensing MRI". In: *IEEE signal processing magazine* 25.2 (2008), p. 72.

[Man+01] A. Manduca, T. E. Oliphant, M. A. Dresner, J. Mahowald, S. A. Kruse, E. Amromin, J. P. Felmlee, J. F. Greenleaf, and R. L. Ehman. "Magnetic resonance elastography: non-invasive mapping of tissue elasticity". In: *Medical image analysis* 5.4 (2001), pp. 237–254.

[Man82] P. Mansfield. *Nmr imaging in biomedicine: Supplement 2 advances in magnetic resonance*. Vol. 2. Elsevier, 1982.

[MBV06] C. B. Marcu, A. M. Beek, and A. C. Van Rossum. "Clinical applications of cardiovascular magnetic resonance imaging". In: *Cmaj* 175.8 (2006), pp. 911–917.

[Mon+17] C. Montalba, J. Urbina, J. Sotelo, M. Andia, C. Tejos, P. Irarrazaval, D. Hurtado, I. Valverde, and S. Uribe. "Variability of 4D flow parameters when subjected to changes in MRI acquisition parameters using a realistic thoracic aortic phantom". In: *Magnetic resonance in medicine* (2017).

[Muh05] A. Muhr. "Modeling the stress-strain behavior of rubber". In: *Rubber chemistry and technology* 78.3 (2005), pp. 391–425.

[NB19] D. Nolte and C. Bertoglio. "Reducing the impact of geometric errors in flow computations using velocity measurements". In: *International journal for numerical methods in biomedical engineering* (2019), e3203.

[Net+12] E. Nett, K. Johnson, A. Frydrychowicz, A. Muñoz, E. Schrauben, C. Francois, and O. Wieben. "Four-dimensional phase contrast MRI with accelerated dual velocity encoding". In: *Journal of Magnetic Resonance Imaging* 35.6 (2012), pp. 1462–1471.

[Nol+19] D. Nolte, J. Urbina, J. Sotelo, L. Sok, C. Montalba, I. Valverde, A. Osses, S. Uribe, and C. Bertoglio. "Validation of 4D-flow-based pressure difference estimators". In: (2019).

[NTT11] A. Nachman, A. Tamasan, and A. Timonov. "Current density impedance imaging". In: *Tomography and inverse transport theory* 559 (2011), pp. 135–149.

[Ogd97] R. W. Ogden. *Non-linear elastic deformations*. Courier Corporation, 1997.

[Pet+06] S. E. Petersen, B. A. Jung, F. Wiesmann, J. B. Selvanayagam, J. M. F rancis, J. Hennig, S. Neubauer, and M. D. Robson. "Myocardial tissue phase mapping with cine phase-contrast mr imaging: regional wall motion ana lysis in healthy volunteers." eng. In: *Radiology* 238.3 (Mar. 2006), pp. 816–826.

[Sac+09] I. Sack, J. Rump, T. Elgeti, A. Samani, and J. Braun. "MR elastography of the human heart: noninvasive assessment of myocardial elasticity changes by shear wave amplitude variations". In: *Magnetic Resonance in Medicine: An Official Journal of the International Society for Magnetic Resonance in Medicine* 61.3 (2009), pp. 668–677.

[Sch+17] S. Schnell, S. Ansari, C. Wu, J. Garcia, I. Murphy, O. Rahman, A. Rahsepar, M. Aristova, J. Collins, J. Carr, and M. Markl. "Accelerated dual-venc 4D flow MRI for neurovascular applications". In: *Journal of Magnetic Resonance Imaging* 46 (2017), pp. 102–114.

[SKS12] J. Song, O. I. Kwon, and J. K. Seo. "Anisotropic elastic moduli reconstruction in transversely isotropic model using MRE". In: *Inverse Problems* 28.11 (2012), p. 115003.

[Sli13] C. P. Slichter. *Principles of Magnetic Resonance*. Springer Series in Solid-State Sciences **1**. Springer Science & Business Media, 2013.

[Sol73] V. A. Solonnikov. "Overdetermined elliptic boundary-value problems". In: *Journal of Mathematical Sciences* 1.4 (1973), pp. 477–512.

[Sot+12] J. A. Sotelo, P. Bächler, S. Chabert, D. Hurtado, P. Irarrazaval, C. Tejos, and S. Uribe. "Normal values of wall shear stress in the pulmonary artery from 4D flow data". In: *Journal of Cardiovascular Magnetic Resonance* 14.S1 (2012), W66.

[Sot+16] J. Sotelo, J. Urbina, I. Valverde, C. Tejos, P. Irarrázaval, M. E. Andia, S. Uribe, and D. E. Hurtado. "3D quantification of wall shear stress and oscillatory shear index using a finite-element method in 3D CINE PC-MRI data of the thoracic aorta". In: *IEEE transactions on medical imaging* 35.6 (2016), pp. 1475–1487.

[Sri+09] M. Srichai, R. Lim, S. Wong, and V. Lee. "Cardiovascular applications of phase-contrast MRI". In: *American Journal of Roentgenology* 192.3 (2009), pp. 662–675.

[Sta+14] Z. Stankovic, B. D. Allen, J. Garcia, K. B. Jarvis, and M. Markl. "4D flow imaging with MRI". In: *Cardiovascular diagnosis and therapy* 4.2 (2014), p. 173.

[SZ03] M. A. Schofield and Y. Zhu. "Fast phase unwrapping algorithm for interferometric applications". In: *Optics letters* 28.14 (2003), pp. 1194–1196.

[Tao06] T. Tao. *Nonlinear dispersive equations: local and global analysis*. 106. American Mathematical Soc., 2006.

[Urb+16] J. Urbina, J. Sotelo, D. Springmüller, C. Montalba, K. Letelier, C. Tejos, P. Irarrázaval, M. Andia, R. Razavi, I. Valverde, and S. Uribe. "Realistic aortic phantom to study hemodynamics using MRI and cardiac catheterization in normal and aortic coarctation conditions". In: *Journal of Magnetic Resonance Imaging* 44.3 (2016), pp. 683–697.

[Wat19] A. Waters. "Unique determination of sound speeds for coupled systems of semilinear wave equations". In: *Indagationes Mathematicae* 30.5 (2019), pp. 904–919.

[WS15] T. Widlak and O. Scherzer. "Stability in the linearized problem of quantitative elastography". In: *Inverse problems* 31.3 (2015), p. 035005.

[Yan+96] G.-Z. Yang, P. J. Kilner, N. B. Wood, S. R. Underwood, and D. N. Firmin. "Computation of flow pressure fields from magnetic resonance velocity mapping". In: *Magnetic resonance in medicine* 36.4 (1996), pp. 520–526.